Coal pollution to critical metals: Recycling rare earth elements from acid mine drainage

by

Benjamin Carl Hedin

B.S., Environmental Science, Allegheny College, 2012

Submitted to the Graduate Faculty of the

Dietrich School of Arts and Sciences in partial fulfillment

of the requirements for the degree of

Doctor of Philosophy

University of Pittsburgh

2021

UNIVERSITY OF PITTSBURGH

DIETRICH SCHOOL OF ARTS AND SCIENCES

This dissertation was presented

by

Benjamin Carl Hedin

It was defended on

March 17, 2021

and approved by

Dr. Charles A Cravotta III, Research Hydrologist, United States Geological Survey

Dr. Dorothy Vesper, Professor, West Virginia University

Dr. Daniel Bain, Associate Professor, University of Pittsburgh

Dr. Charles E. Jones, Senior Lecturer, University of Pittsburgh

Dr. Brian Stewart, Associate Professor, University of Pittsburgh

Dissertation Director: Dr. Rosemary Capo Associate Professor, University of Pittsburgh

Coal pollution to critical metals: Recycling rare earth elements from acid mine drainage

Benjamin Carl Hedin, PhD

University of Pittsburgh, 2021

Acid mine drainage (AMD) has been proposed as a novel source of rare earth elements (REE); a group of elements that include critical metals for clean energy technologies. REE are sequestered in the waste solids produced from precipitating metals during the treatment of AMD. Because these solids are typically landfilled or buried on site, they are a low cost, readily available REE source.

Here, I present my results from sampling AMD waters and solids, characterizing AMD solids using chemical and physical techniques, and constructing geochemical models to simulate dissolved REE attenuation from AMD. Sampling data show that AMD solids produced from low pH AMD treated by limestone or NaOH produce solids with the highest concentrations of REE and that these solids typically contain Fe, Al, and Mn phases. Characterization demonstrates that for all AMD solids evaluated, acidic and/or reducing extractions are required to mobilize REE. In solids dominated by Al phases, REE are widely dispersed throughout. However, in solids containing Fe and Mn phases, REE can co-associated with these phases. Finally, geochemical modeling indicates that pH dependent dissolved REE attenuation is dominated by surface complexation on Fe, Al, and Mn oxide/hydroxides. The models developed here can be applied to other AMD systems to predict REE removal and what solid phases will be enriched in REE and to engineer AMD systems to produce specific minerals enriched in REE.

Table of contents

List of tables

List of figures

Preface

Thank you committee members Rosemary Capo, Brian Stewart, Dan Bain, Charlie Jones, Chuck Cravotta, and Dorothy Vesper for guidance throughout my PhD journey. Thank you Christina Lopano and Mengling Stuckman for the mentorship and support that made much of this dissertation possible. Thank you to fellow graduate students for keeping me sane over the past 5 years. Finally, thank you friends and family for your unwavering support.

1.0 Introduction

Acid mine drainage (AMD) is a global environmental problem and common byproduct of mining. Mining practices typically expose subsurface minerals to surface conditions, altering or accelerating normal weathering reactions. One common reaction is the dissolution of sulfide minerals to produce high concentrations of Fe^{+2}, sulfate, and acidity (H^{+}) from the subsequent oxidation of sulfur (Younger, Banwart, & Hedin, 2002).

$$FeS_{2(s)} + 3.5\ O_{2(aq)} + H_2O = Fe^{+2} + 2\ SO_4^{-2} + 2H^{+}$$

This acidity can dissolve other subsurface minerals (e.g. alumino-silicates and manganese oxides/carbonates) resulting in high concentrations of cations including, but not limited to, Mn^{+2}, Al^{+3}, Na^{+}, and K^{+}.

In the Appalachian coalfield of the USA alone, over 5,400 km of streams are impaired by pH, sulfate, and/or metals from AMD (EPA, 2015). While AMD is a significant source of pollution, it could also be a resource. For example, iron oxide recovered from treatment systems is sold as pigment (Hedin, 2003) and could be used to decrease phosphorous concentrations in manure (Hedin, Hedin, Spargo, & Brimmer, 2020b; Sibrell, Montgomery, Ritenour, & Tucker, 2009), sequester trace metals in soils (Liu, Altschul, Hedin, Nakles, & Dzombak, 2014), decrease H_2S release from gypsum bedding for dairy cows (Chen, 2018), and adsorb Se from mine wastes (Donovan & Ziemkiewicz, 2013). Recently, AMD has also been proposed as a novel source of Rare Earth Elements (REE) (Ayora et al., 2016; Stewart, Capo, Hedin, & Hedin, 2017; Vass, Noble, & Ziemkiewicz, 2019b). REE include the lanthanide elements La through Lu (atomic numbers 57 to 71) and commonly include yttrium and scandium because of their similar geochemical behavior. Here, REE are defined as the lanthanide group and Y.

REE are an important group of metals that have received recent attention for three primary reasons:

1) REE have important functions in renewable energy technologies such as magnets, catalysts, and batteries (Van Gosen, Verplanck, Seal, Long, & Gambogi, 2017b; Wall, 2014). Five REE (Y, Nd, Dy, Eu, and Tb), are considered "critical resources" because of their importance to clean energy technologies (DOE, 2011). For example, the use of REE for the manufacture of electric cars, rechargeable batteries, and wind power infrastructure is expected to increase up to 90% by 2030 (Zhou, Li, & Chen, 2017) and the use of Nd and Dy could increase by over 700% (Alonso et al., 2012).

2) Most of the global REE supply comes from one country with approximately 60% and 80% of REE mined and refined in China, respectively (Law, 2019). In the U.S., approximately 80% of REE are imported from China (USGS, 2020).

3) The refining of traditional REE ores (e.g. carbonatites) commonly produces radioactive wastes because of the co-occurrence of REE and U and Th in these ores (Van Gosen, Verplanck, Seal, Long, & Gambogi, 2017a). These wastes are hazardous to human health and the environment and could complicate a global REE supply. For example, in 2018 the only major REE refiner outside of China, LynasCorp, located Malaysia, was threatened to be shut down by the Malaysian government over the production and storage of radioactive waste on the site (Law, 2019).

The increasing global demand for REE and geopolitical risks associated with geographically concentrated REE mining and refining have led to the investigation of many alternative sources of REE including recycling (Binnemans et al., 2013), deep ocean deposits (Hein, Mizell, Koschinsky, & Conrad, 2013; Takaya et al., 2018), coal fly ash (Lin et al., 2018; Stuckman, Lopano, & Granite, 2018), and AMD (Ayora et al., 2016; Lefticariu, Klitzing, &

Kolker, 2019; Stewart et al., 2017; Vass, Noble, & Ziemkiewicz, 2019a). Most methods for recovering REE from AMD have typically focused on two methods: development of specialized sorbents that can selectively remove dissolved REE from solutions (Callura et al., 2018) or the development of processing methods that precipitate REE and then process these solids to enrich REE concentrations (Zhang & Honaker, 2018).

The precipitation of dissolved REE from AMD already occurs during the treatment of AMD. AMD is commonly treated by adjusting pH and redox conditions to neutralize acidity and precipitate dissolved metals. The precipitated solids typically consist of Al/Fe/Mn oxide/hydroxides/sulfates and can contain calcite, gypsum, and lime depending on treatment technology and geochemical conditions (Cravotta & Trahan, 1999; Kairies, Capo, & Watzlaf, 2005; Lozano et al., 2019b; Pu, Vazquez, Monnell, & Neufeld, 2010; Tan, Zhang, Heaney, Webb, & Burgos, 2010). During the treatment of AMD, the concentrations of REE leaving treatment systems are commonly less than 10% of the concentrations entering systems (Cravotta & Brady, 2015; Orden et al., 2021) and AMD solids recovered from treatment systems can have high concentrations of REE, up to about 2,000 mg/kg (Stewart et al., 2017; Vass et al., 2019b). AMD solids are a waste by-product from treatment of AMD, which will continue for decades to centuries, and therefore are a low-cost material from which to recover REE.

AMD solids are produced on massive scales from mining and treatment operations. For example, in Pennsylvania alone, over 1.6×10^7 kg of AMD solids are produced per year (Stream Restoration, 2018). These solids are typically pumped back into underground mines or landfilled on site and managing AMD solids is a significant operational expense (Cravotta, Means, Arthur, McKenzie, & Parkhurst, 2014). Recovering REE from waste AMD solids is an opportunity to supply critical metals from an environmental liability. To maximize this opportunity, the most

promising AMD solids for REE recovery must be identified and REE hosting mineral phase(s) identified so REE extraction methods can be developed.

In chapter two of this dissertation (published as B.C. Hedin et al., 2019), I identify chemical conditions required to sequester REE in AMD solids in conventional AMD treatment systems and identify Mn oxides as an important phase for REE accumulation. I further characterize the most promising AMD solids for REE recovery, in chapter three of this dissertation (published as B. C. Hedin, Hedin, Capo & Stewart, 2020), using a database of 281 analyses of AMD treatment solids to demonstrate that REE and Co are promising critical metals to target for recovery from AMD solids and that these metals are positively correlated with Al and Mn concentrations.

To develop targeted REE extraction procedures, identification of the REE hosting phase(s) in AMD solids is an important step. In chapter four, I determine minerals/solid phases associated with REE using chemical extractions, micro scale imaging, and Ce oxidation state measurements. These data are synthesized with surface complexation geochemical models to reproduce empirical results. These geochemical models can be applied more widely to other systems to predict dissolved REE removal and REE accumulation in solids.

2.0 Second The evaluation of critical rare earth element (REE) enriched treatment solids from coal mine drainage passive treatment systems

2.1 Introduction

Rare earth elements (REE), generally defined as the 15 lanthanide elements (atomic numbers 57 to 71) and yttrium, are a group of metals with similar geochemical properties and critical technological functions (Du & Graedel, 2011; USGS, 2018; Wall, 2014). REE are important components in magnets, catalysts, batteries and other products which are essential for clean energy technologies such as hybrid cars and wind turbines (Binnemans et al., 2013; DOE, 2011). The use of REE in materials critical for the manufacturing of electric cars, rechargeable batteries, and wind power infrastructure is expected to increase from 65% of total REE consumption to 92% of global REE consumption by 2030 (Zhou et al., 2017). Currently, almost 80% of worldwide REE are mined in China and REE have not been mined in the U.S. since 2016 (USGS, 2018). The importance of REE to clean energy and REE supply risk has led to the designation of five REE (Y, Nd, Dy, Eu, and Tb) as "critical resources" (DOE, 2011). The demand for certain critical REE (e.g. Nd and Dy) could increase by over 700% by 2035 with rapid green energy adoption (Alonso et al., 2012).

Current REE mining and extraction processes are associated with negative impacts to human health and the environment (Haque, Hughes, Lim, & Vernon, 2014). A major concern of REE mining is the co-occurrence of REE deposits with radioactive elements like thorium and uranium, which can lead to radiological exposure during mining and processing and results in the production of radioactive waste (Ault, Krahn, & Croff, 2015; Binnemans et al., 2013; Dutta et al.,

2016). Additionally, mining techniques, including open pit mining and in situ leaching, are associated with environmental impacts such as groundwater contamination, deforestation, and soil erosion (Dutta et al., 2016; Yang et al., 2013). Overall, the water and energy consumption of REE processing is significantly higher compared to other metals (Haque et al., 2014) and the environmental impact of new sources of REE, such as ocean ferro-manganese nodules, is uncertain (Hein et al., 2013; Koschinsky et al., 2018). Increasing demand for REE and environmentally costly mining/extraction techniques have sparked research into alternative sources, such as REE recovery from coal and coal related materials (Dai & Finkelman, 2018; Lin et al., 2018; Stuckman et al., 2018; Zhang & Honaker, 2018).

Acidic mine drainage (AMD), resulting from the oxidation of iron-sulfide minerals, has been shown to be enriched in REE; thus, mine drainage has been proposed as a potential source of REE (Ayora et al., 2016; Stewart et al., 2017; Ziemkiewicz, He, Noble, & Lui, 2016). Contaminated mine drainage is a major global challenge facing the mining industry (Hudson-Edwards, Jamieson, & Lottermoser, 2011). In the Appalachian region of the eastern USA alone, over 5,400 kilometers of streams are polluted with mine drainage due to centuries of coal mining (EPA, 2015). Appalachian coal mine drainage (CMD) ranges from acidic (pH <3) to circumneutral (pH ~7), anoxic to oxic, and can contain up to hundreds of mg/L of dissolved iron (Fe), aluminum (Al), and manganese (Mn) (Cravotta, 2008a). Dissolved REE concentrations in Appalachian CMD range from <1 to almost 2,000 µg/L and are negatively correlated with pH (Cravotta, 2008a; Stewart et al., 2017). AMD (defined here as mine drainage with pH <5.5), in particular, is enriched in REE with total concentrations up to three orders of magnitude higher than unpolluted fresh water (Cravotta, 2008a; Cravotta & Brady, 2015; Noack, Dzombak, & Karamalidis, 2014). REE can be categorized by geochemical classifications such as light (La, Ce,

Pr, Nd, Sm), middle (Eu, Gd, Tb, Dy, Y), and heavy (Ho, Er, Tm, Yb, Lu) and application classification such as energy-critical (Y, Nd, Dy, Eu, Tb) (DOE, 2011; Seredin & Dai, 2012). Based on a survey of the literature, (Cravotta, 2008a; Cravotta & Brady, 2015; Stewart et al., 2017), Appalachian CMD is enriched in both energy critical (55% ±12 wt. % of total REE concentrations) and middle REE and depleted in light REE when normalized to the North American Shale Composite (NASC) (Gromet, Dymek, Haskin, & Korotev, 1984; Haskin & Haskin, 1966).

Mine drainage treatment involves acid neutralization and/or redox adjustment to precipitate dissolved metals, resulting in large quantities of waste solids (>1.6 x 10^7 kg/year in Pennsylvania, USA alone (Stream Restoration, 2018)), the disposal of which is a major cost to treatment operators (Cavazza & Beam, 2010; Cravotta & Brady, 2015). These precipitated solids, defined herein as treatment solids, are enriched in total REE up to ~1,000 ppm (Stewart et al., 2017) and have been proposed as a potential source of REE (Ayora et al., 2016; Erickson, 2018; Stewart et al., 2017; Zhang & Honaker, 2018; Ziemkiewicz et al., 2016). Estimates indicate that up to 5 x 10^5 kg of REE could be recovered every year from Appalachian CMD alone (Stewart et al., 2017). However, the impact of treatment methods on REE concentrations in treatment solids is not well documented.

Mine drainage treatment technologies generally fall into one of two categories: “active treatment” or “passive treatment” (Younger et al., 2002). Active treatment systems involve the constant addition of chemicals (e.g., lime, sodium hydroxide, and hydrogen peroxide) to neutralize acidity and oxidize and/or hydrolyze dissolved metals. Active systems require delivery, storage, and mixing procedures for chemical reagent(s), routine maintenance of mechanical equipment, and electricity for pumps and aerators (Younger et al., 2002). Treatment solids (Fe, Al, and Mn

oxides and hydroxides as well as other minerals such as calcite, dolomite, and gypsum) plus unreacted caustic agents accumulate as sludge in settling ponds or mechanical clarifiers which must be regularly cleaned.

Passive treatment systems typically do not use electricity or chemicals, and rely on gravity flow, natural geochemical processes, and microbial activity (Hedin, Watzlaf, & Nairn, 1994; Younger et al., 2002). There are many different passive treatment technologies and each technology is applied to specific water chemistry (Hedin, Weaver, Wolfe, & Watzlaf, 2013; Skousen et al., 2017). Limestone aggregate is commonly used in passive systems to raise the pH to 6-8, which results in a bicarbonate-buffered solution that facilitates the oxidation, hydrolysis, and precipitation of dissolved Fe, Al, and Mn, and largely limits the precipitation of nontarget solids (e.g., calcite, gypsum, $Mg(OH)_2$).

Unlike active systems, which typically produce a single sludge containing a mixture of metal precipitates and unreacted chemical additives, passive systems often treat CMD sequentially in separate treatment steps. Sequential treatment technologies can generate different metal-rich solids at each step and may provide different geochemical and physical environments for REE enrichment. Examining the processes and conditions that facilitate REE precipitation and selective enrichment in passive treatment systems offers the opportunity to maximize REE recovery in treatment solids.

The composition of treatment solids in passive treatment systems can be influenced by pH, redox, and precipitation mechanics. For example, the removal of dissolved oxygen (DO) via microbial respiration in an organic substrate layer preceding a limestone bed limits Fe(II) and Mn(II) oxidation in the limestone bed, but allows for Al(III) hydrolysis (Hedin, Weaver, Wolfe, & Weaver, 2010). In subsequent oxidizing conditions, the rapid oxidation of Fe(II) at near-neutral

pH can produce solids composed predominantly of Fe(III) hydroxide. Additionally, the heterogeneous precipitation of Mn(II) via sorption and autocatalytic/biologically-catalyzed oxidation of Mn(II) on existing Mn(III/IV) oxide results in a growing, armored Mn-oxide surface on limestone solids that is largely immobile (Hansel, Zeiner, Santelli, & Webb, 2012; Luan, Santelli, Hansel, & Burgos, 2012; Post, 1999; Santelli, Webb, Dohnalkova, & Hansel, 2011a; Tan et al., 2010). Homogenous Al(III) hydroxide precipitation via hydrolysis often creates colloidal solids that can be transported by turbid water (Hedin Environmental, 2008). Phases in passive mine drainage treatment solids include amorphous Al phases (e.g., $Al(OH)_3$ and $Al(OH)(SO_4)$) (Ayora et al., 2016; Cravotta & Trahan, 1999; Pu et al., 2010), iron oxides and hydroxides (e.g., goethite, FeO(OH); ferrihydrite, $Fe(OH)_3 \cdot 0.5H_2O$; and schwertmannite, $Fe_8O_8(OH)_6(SO_4)$) (Bigham, Schwertmann, Traina, Winland, & Wolf, 1996; Cravotta & Trahan, 1999; Hedin, 2003; Kairies et al., 2005), and manganese oxides (e.g., birnessite, $(Na,Ca)Mn_7O_{14}$; and todorokite $(Ca,Na,K)_xMn_6O_{12}$) (Cravotta & Trahan, 1999; Tan et al., 2010).

Although Cravotta & Brady (2015) documented REE removal in active and passive CMD treatment systems, REE behavior in different types of passive mine drainage treatment systems is largely unknown. Work in other geochemical environments suggests that dissolved REE can be removed by adsorption on hydrous Fe(III) oxides/hydroxides at neutral pH (e.g. goethite and ferrihydrite), but are not removed by Fe(III) oxides/hydroxides at low pH (e.g. schwertmannite) (Ayora et al., 2016; Bau, 1999; de Carlo, Wen, & Irving, 1998; Prudêncio, Valente, Marques, & Braga, 2015; Verplanck, Nordstrom, Taylor, & Kimball, 2004). Ayora et al. (2016) used sequential extractions and synchrotron micro-x-ray fluorescence (μ-XRF) on treatment solids from benchtop experiments simulating passive treatment systems to show the sorption and co-precipitation of REE on basaluminite (aluminum-sulfate mineral) treatment solids. Zhang and

Honaker (2018) titrated AMD with NaOH in a stepwise manner, collected precipitated solids after each NaOH addition step, and found that REE were most enriched in the Al solids. Mn oxides (e.g. birnessite and todorokite) can also be produced in passive treatment systems (Cravotta & Trahan, 1999; Tan et al., 2010). Mn oxides exhibit strong sorptive properties (Bau, Koschinsky, Dulski, & Hein, 1996a; Cao, Chen, Wang, & Deng, 2001); however, to-date, the role of Mn oxides in REE removal from mine drainage has not been investigated.

To investigate the REE characteristics in treatment solids, we designed this study to: (1) determine REE mobility in geochemically diverse passive treatment systems and identify treatment solids that are enriched in REE, and (2) evaluate how different mine drainage treatment technologies concentrate REE into treatment solids. To do this, we investigated REE attenuation in treatment solids from selected passive treatment systems and documented the physical and geochemical conditions that lead to accumulation of high concentrations of REE. Second, we mapped micro-scale REE distribution and their associations with different phases in Mn rich treatment solids recovered from a passive treatment system. Third, we calculated REE concentration factors for 17 passive and active treatment systems. The results of this study will help inform future REE recovery efforts and aid in the construction of treatment systems specifically designed to remove and concentrate REE from CMD. They also have the potential to support environmentally friendly CMD remediation efforts, often spearheaded by local community groups, with REE resource recovery.

2.2 Methods

2.2.1 Treatment system sampling

Influent (untreated) and effluent (treated) water samples and treatment solid samples were collected from four passive treatment technologies each with unique internal geochemical conditions (Table 1). The passive treatment technologies sampled in this study are oxidation/settling ponds (SPs), low pH Fe removal (LP) systems, vertical flow ponds (VFPs), and drainable limestone beds (DLBs). Different sites using the same treatment technology are identified numerically after the treatment technology (e.g., VFP-1, VFP-2…etc.).

Table 1 Summary of passive treatment systems sampled in this study and the major geochemistry of the untreated water and conditions found inside the treatment systems (internal pH).

Treatment system	Samples	Influent pH[a]	Internal pH[a]	Internal redox[b]	Major pollutants
Settling ponds					
SP-1	Solids	Circumneutral	Circumneutral	Oxic	Fe
Low pH Fe oxidation					
LP-1	In/Out, solids	Low	Low	Oxic	Fe, Al, Mn
Vertical flow ponds					
VFP-1	In/Out	Low	Circumneutral	Anoxic	Fe, Al, Mn
VFP-2	In/Out	Low	Circumneutral	Anoxic	Fe, Al, Mn
Drainable limestone beds					
DLB-1	In/Out, solids	Low	Circumneutral	Oxic	Al
DLB-2	In/Out, solids	Low	Circumneutral	Oxic	Al, Mn
DLB-3	In/Out	Low	Circumneutral	Oxic	Fe, Al, Mn
DLB-4	Solids	Low	Circumneutral	Oxic	Fe, Al, Mn

[a]Low pH is between 2.9 and 4.1 and circumneutral pH is between 6.3 and 7.2.
[b]Oxic is between 2.3 and 13 mg/L DO and Anoxic is between 0.1 and 0.6 mg/L DO.

The SP-1 treatment system consists of a series of six settling ponds and a wetland, treating circumneutral, anoxic CMD with elevated Fe(II) concentrations. Passive aeration generates oxic,

circumneutral geochemical conditions, promoting abiotic Fe(II) oxidation and the settling of Fe(III) solids (Figure 1A; Table 1) (Hedin, 2008). Treatment solids were collected from each setting pond and the wetland.

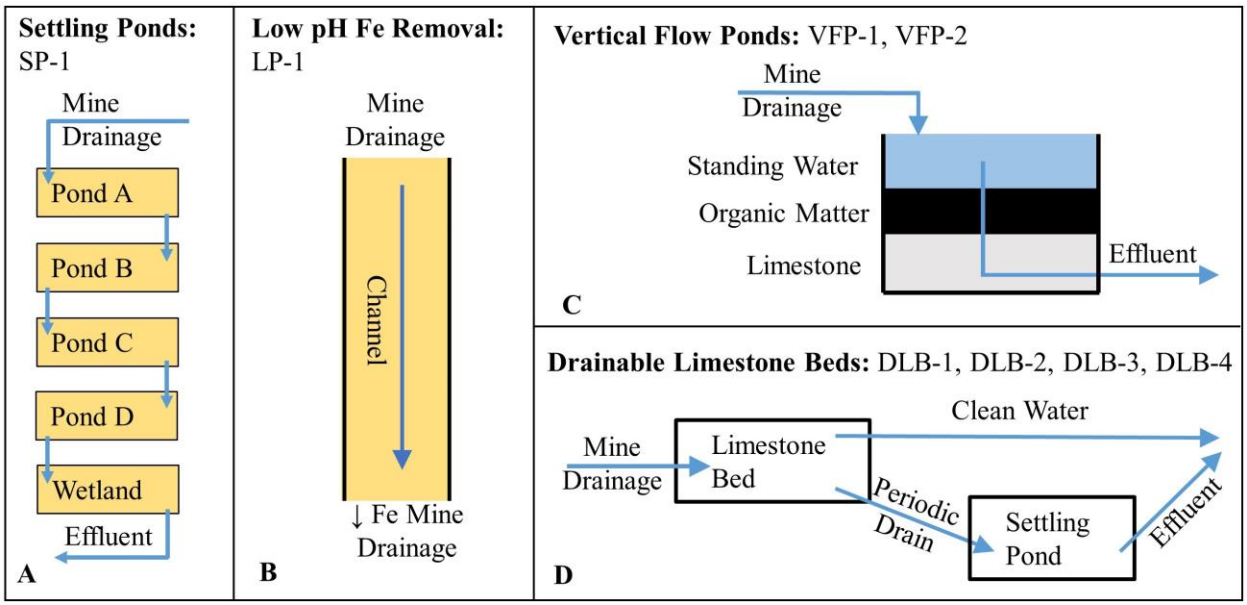

Figure 1 Schematics of passive treatment systems sampled in this study. A. sequential settling ponds (SP) and wetlands. B. low pH Fe removal system (LP). C. vertical flow pond (VFP). D. drainable limestone bed (DLB).

The LP-1 treatment system consists of an open channel treating low pH, oxic CMD with elevated Fe, Al, and Mn concentrations. The generation of oxic, low pH conditions through the system promotes biotic Fe(II) oxidation and the settling of Fe(III) solids (Figure 1B; Table 1) (Stream Restoration, 2018). Influent and effluent water samples and treatment solids were collected from LP-1 for analysis.

The VFP-1 and VFP-2 treatment systems are limestone beds covered with organic substrate and standing water treating low pH, oxic CMD with elevated Fe, Al, and Mn concentrations

(Figure 1C; Table 1). Microbial aerobic respiration in the organic substrate creates anoxic conditions and reduces Fe(III) to Fe(II) before reacting with the limestone. This limits the oxidation and precipitation of dissolved Fe and Mn; but allows for the hydrolysis and precipitation of dissolved Al (Hedin et al., 2010). Influent and effluent water samples were collected from VFP-1 and VFP-2, but treatment solids were not available for sampling.

The DLB-1, DLB-2, DLB-3, and DLB-4 treatment systems are limestone beds treating low pH, oxic CMD with elevated Fe, Al, and Mn concentrations (Figure 1D; Table 1). Limestone dissolution neutralizes acidity and generates alkalinity, promoting the precipitation of dissolved Fe, Al, and Mn via oxidation and hydrolysis reactions. DLBs are periodically drained of fluid (approximately weekly) to remove solids that have accumulated in the limestone. Draining removes Al, but not Mn solids, from the limestone bed into settling ponds. Mn precipitants tend to cement onto the limestone aggregate and are not removed with draining (Hedin Environmental, 2008). Influent and effluent water samples were collected from DLB-1, DLB-2, and DLB-3. Solid samples were collected from the flush pond of DLB-1, the flush pond and limestone bed of DLB-2, and the limestone bed of DLB-4.

2.2.2 Chemical analysis

Fourteen influent and effluent water samples from the passive treatment systems described above were collected and filtered to <0.45 μm. Acidified aliquots of the samples (2% ultrapure nitric acid) were analyzed for major elements, trace elements, and all REE at Activation Laboratories, Ontario, Canada (Actlabs, 2018) by inductively coupled plasma mass spectrometry (ICP-MS) (6 - Hydrogeochemistry-ICP/MS method). Unacidified aliquots were analyzed for anions by ion chromatography (IC) (6B - Ion Chromatography method). Sulfate concentrations

were measured at G&C Coal Analysis Labs, Summerville, PA, USA by IC. Cation-anion balances are ≤±6% except for LP-1 influent and effluent which are -24% and -21% imbalanced, respectively. Field data collected concurrently included flow rate, pH, conductivity, dissolved oxygen, oxidation-reduction potential, and alkalinity. Alkalinity was measured via gran titrations on unfiltered samples collected with minimal headspace no more than 10 hours after collection.

Approximately 3 liters of treatment solids collected from the five passive treatment systems described above were stored in resealable plastic bags until processing. Solid samples were dried at 105°C and when treatment solids were cemented onto limestone, the limestone aggregate was dried and lightly sieved to <2 mm to separate the limestone and cemented solids. For DLB-1, DLB-2, and DLB-4, dried treatment solids were analyzed for major oxides, trace elements, and all REE at Activation Laboratories by lithium metaborate/tetraborate fusion and inductively coupled plasma optical emission spectrometry (ICP-OES) and ICP-MS (4Litho method) and for C and S by infrared spectroscopy (IR) (4F - C, S method) (Actlabs, 2018). Average deviations from certified reference material (CRM) for individual lanthanide elements were less than 4% and for Y was 14%. For SP-1, dried treatment solids were analyzed for major oxides, trace elements, and select REE (Y, La, Ce, Nd, Sm, Eu, Tb, Yb, and Lu) at Activation Laboratories by ICP-OES and instrumental neutron activation analysis (INAA) (4E-expl. method) (Actlabs, 2018). Due to incomplete REE analysis and many REE concentrations below the method detection limit, Y concentrations are used as proxies for total REE concentrations at SP-1 using the linear regression calculated in this study (Total REE (µg/L) = Y (µg/L) × 3.6875; R^2 = 0.76; Appendix Figure 1).

Major element data for solids in this study are reported as oxides as measured by Activation Labs (e.g., Fe_2O_3) which does not reflect the mineralogy of the solids in treatment systems (e.g., FeO(OH)). Loss on ignition (LOI) is the mass of volatiles (e.g. hydrates, carbon dioxide from

carbonates, and organic matter) lost from a sample heated to 750°C (Actlabs, 2018). Total recovery (major oxides + LOI + C + S) ranges from 96% to 103% for the solid samples in this study.

2.2.3 Microanalysis

Powdered treatment solids collected from DLB-2, and -4 were analyzed for crystalline solids via X-ray diffraction (*XRD*). Ground material was backloaded into a 10 mm diameter cavity spin mount for analysis via XRD. The samples were run on a PANalytical X'Pert Pro utilizing copper X-rays at 45 kV, 40 mA, with an X'Celerator parallel plate detector. The samples were scanned between 4-70° 2θ at using a step size of 0.033°/step and a 1,000 sec count time. The resulting XRD patterns were compared against the PDF-4 ICDD database using the X'Pert HighScore program to identify the crystalline mineral phases present.

A cross-section of a single piece of Mn-coated limestone from DLB-2 was prepared into a 30-µm thick doubly-polished microprobe-prepped thin section (Spectrum Petrographics, Inc.) for Scanning Electron Microscopy (*SEM*) imaging and synchrotron micro-X-ray Fluorescence (*µ-XRF*) elemental maps. SEM with energy dispersive X-ray spectroscopy (SEM-EDS; Quanta 600 FEG, FEI, Hillsboro, OR) was performed for point-analysis and mapping selected regions in BSE mode (under high vacuum, 20 keV excitation energy, with 3.0 µm spot size). µ-XRF mapping was conducted using synchrotron radiation at beam line 2-3 at the Stanford Synchrotron Radiation Light Source (SSRL) which was equipped with a 4-µm beam size, Si(1,1,1) crystal, and a single element Si Vortex detector. Mapping was conducted at 9,500 eV with a 5 µm step size and 100 ms dwell time. Element maps were processed in the SIXpack software (Webb, 2005) including

using PyMCA fitting to deconvolute and potential spectral interferences between REE and transition metals, as per Stuckman et al. (2018).

2.2.4 REE concentration in different treatment systems (passive vs. active)

To evaluate how efficiently REE are concentrated into treatment solids by different treatment technologies, treatment solid and influent CMD chemistry from 17 individual treatment systems were paired and analyzed. Solids data are from this study, Hedin Environmental, and Stewart et al. (2017). Solids collected by Hedin Environmental were analyzed by Activation Laboratories. Data from multiple solid samples from a single treatment system were averaged. Influent CMD data are from this study, Cravotta (2008), and Cravotta and Brady (2015).

From these data, solids concentration factors for each treatment system were calculated. Yttrium concentrations were used as proxies for total REE concentrations in both solids and influent CMD samples because for some samples, either Y was the only REE measured or most REE are below detection limits. Total REE concentrations calculated from Y concentrations are noted in the text and figures.

Concentration factors can be calculated using REE concentrations in treatment solids and influent CMD (Ziemkiewicz et al., 2016). However, REE concentrations in a treatment solid sample are a composite value representing accumulation over time, while REE concentrations in an influent CMD waters are an instantaneous value and subject to diel and seasonal fluctuations and dilution. We propose to account for this difference by normalizing dissolved REE concentrations (using Y as a proxy) to total dissolved solids (TDS) in influent CMD. This normalization accounts for the effects of dilution and diel cycling because of the expected

covariance of dissolved REE and TDS at a given CMD discharge (Vesper & Smilley, 2010). We calculate the REE solids concentration factor (CF_s) for individual treatment systems as:

$$CF_s = \frac{Y_{ts}}{Y_{in}/TDS_{in}}$$

where Y_{ts} (ug/g) is the yttrium concentration in the treatment solids, Y_{in} (µg/L) is the concentration in the influent, and TDS_{in} (g/L) is the total dissolved solids of the influent.

2.3 Results

2.3.1 REE partitioning in passive treatment systems

Settling ponds (SPs) treat circumneutral mine drainage with elevated Fe concentrations by oxygen transfer and CO_2 degassing to promote the abiotic oxidation of Fe(II) (Younger et al., 2002). SP-1 influent has high Fe (58 mg/L) and low REE (6 µg/L) concentrations at the influent and the circumneutral and oxic conditions decrease Fe concentrations to <0.1 mg/L in the effluent (Table 2). Fe(III) hydroxide/oxides constitute approximately 70% of the settling pond solids (Figure 2), likely as goethite/ferrihydrite (Kairies et al., 2005).

Table 2 Influent and effluent chemistry of treatment systems in this study. For SP-1, major element data are from Hedin Environmental and REE data are from Cravotta, 2008. DLB 4 data are from Hedin Environmental. All other data were collected in this study. HCO_3^- is calculated from field alkalinity. TRT = theoretical retention time. N/A = data not available.

Site	Location	Flow L/sec	pH	DO	HCO_3	Fe	Al	Mn	Ca	Mg	Na	K	SO4	Cl	Si	Sr	ΣREE µg/l	TRT hours
										mg/L								
SP-1	Influent	115.9	6.31	0.7	416	58.3	<0.1	1.0	154	41	479.1	6.1	1,105	124.7	9.7	2.2	6	71
SP-1	Effluent		7.93	18.8	278	<0.1	<0.1	0.1	130	41	456.0	4.7	1,057	140.5	5.4	1.9	N/A	
LP-1	Influent	0.9	2.86	6.4	0	128.9	32.3	43.1	122	98	28.4	6.4	2,077	47.2	12.9	0.2	1,297	21
LP-1	Effluent		2.94	13.0	0	61.8	25.8	37.2	168	88	24.0	6.1	1,718	39.6	10.3	0.3	1,003	

VFP-1	Influent	0.3	4.13	3.1	0	64.4	40.1	67.8	158	234	3.5	7.5	1,759	2.5	18.9	0.2	779	103
VFP-1	Effluent		6.28	0.6	242	32.4	0.6	*79.8	403	295	4.1	8.6	2,329	2.8	6.0	1.3	73	
VFP-2	Influent	6.0	2.73	10.9	0	14.0	17.2	3.8	18	21	0.7	1.2	364	0.4	11.2	0.1	145	201
VFP-2	Effluent		6.84	0.0	171	4.1	<0.1	3.1	158	17	0.7	1.5	354	0.5	9.4	0.2	1	
DLB-1	Influent	0.2	3.27	4.7	0	0.7	19.7	0.8	106	45	11.7	0.8	608	4.9	16.9	1.2	181	119
DLB-1	Effluent		6.62	4.2	274	<0.1	0.1	0.1	252	47	11.7	1.0	560	5.6	12.2	1.5	5	
DLB-2	Influent	2.7	3.91	3.9	0	0.0	7.4	16.1	91	99	2.8	4.4	701	0.9	10.4	0.1	151	31
DLB-2	Effluent		6.98	3.2	209	<0.1	<0.1	0.3	193	100	2.8	4.4	713	1.3	9.1	0.2	3	
DLB-3	Influent	0.6	3.35	12.1	0	5.6	4.0	40.3	422	273	4.0	8.0	1,997	15.6	12.9	1.3	453	94
DLB-3	Effluent		7.24	2.3	111	0.2	0.1	0.1	496	264	0.1	7.9	1,868	21.2	11.4	3.1	11	
DLB-4	Influent	0.1	2.99	N/A	0	4.0	16.8	7.3	N/A	N/A	N/A	N/A	394	N/A	N/A	N/A	N/A	54
DLB-4	Effluent		7.36	N/A	124	<0.1	<0.1	0.3	N/A	N/A	N/A	N/A	392	N/A	N/A	N/A	N/A	

*Effluent Mn concentration is likely greater than influent because of changing influent water chemistry in one bed volume.

Total REE concentrations in SP-1 treatment solids were calculated from Y concentrations because the concentrations of some REE were below the method detection limit and because Y concentrations and total REE concentrations are well correlated (Appendix Figure 1). REE concentrations in the solids are 380 ppm in the first pond and decrease to 37 ppm by the seventh pond (Figure 2). REE concentrations in the treatment solids are relatively low in this system due to low influent REE concentrations (Table 2).

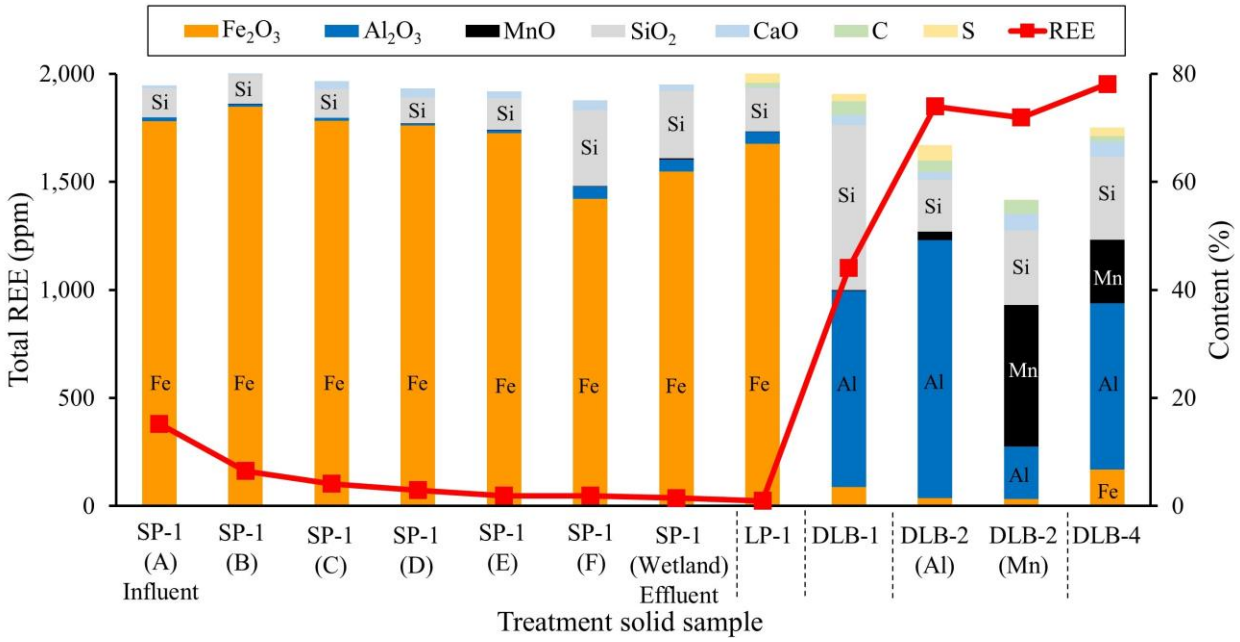

Figure 2 Total REE and oxide concentrations of the treatment solids collected from passive treatment systems in this study. The remaining solids composition (>2%) is loss on ignition (LOI). SP-1 total REE concentrations are calculated from Y concentrations and do not include C and S measurements.

Low-pH Fe removal systems (LPs) treat low pH mine drainage with elevated Fe concentrations by oxygen transfer to promote the biotic oxidation of Fe(II) (DeSa, Brown, & Burgos, 2010; Larson, Sánchez-España, & Burgos, 2014). The low pH and oxic conditions in LP-1 decrease dissolved Fe from 129 mg/L in the influent to 62 mg/L in the effluent (52% reduction). Concentrations of REE and other dissolved metals, as well as pH, are generally conserved through the treatment system, with total REE concentrations only decreasing from 1,297 µg/L to 1,003 µg/L, a 23% reduction (Table 2). Approximately 50% of the change in REE concentration is likely due to dilution from unpolluted fresh water, as indicated by the similar decreases in Mn, Na, Cl, and K concentrations (Table 2), which should act as conservative tracers under low pH conditions. Accounting for this dilution, only 11% of dissolved REE and 45% of dissolved Fe is removed in LP-1 (Figure 3).

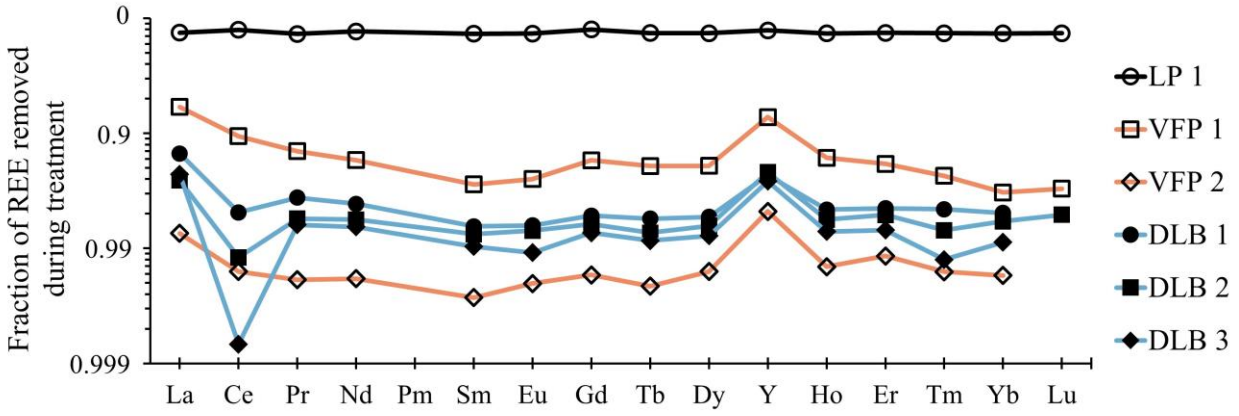

Figure 3 Fraction of total REE removal for DLBs (in blue), VFPs (in red), and LPs (in black). Removal is calculated as (1 – $REE_{effluent}$ / $REE_{influent}$). Redox conditions are reducing in VFPs and oxidizing in DLBs and LP. Missing data for Lu is due to effluent samples below detection limit (<0.004 µg/L).

Solids accumulating in the open channel of LP-1 are 67% Fe(III) oxides/hydroxides (Figure 2) with both amorphous Fe mineral and goethite phases (Appendix Figure 2). Based on

the low pH and high SO_4 concentration in LP-1, schwertmannite is likely precipitating (Bigham et al., 1996) and recrystallizing to goethite over months/years (Schwertmann & Carlson, 2005). These solids contain 24 ppm REE (Figure 2) and have a flat REE pattern when normalized to NASC (Figure 4). The treatment solids produced at LP-1 contain low concentrations of REE (Figure 2) despite high dissolved REE concentrations in the influent (Table 2).

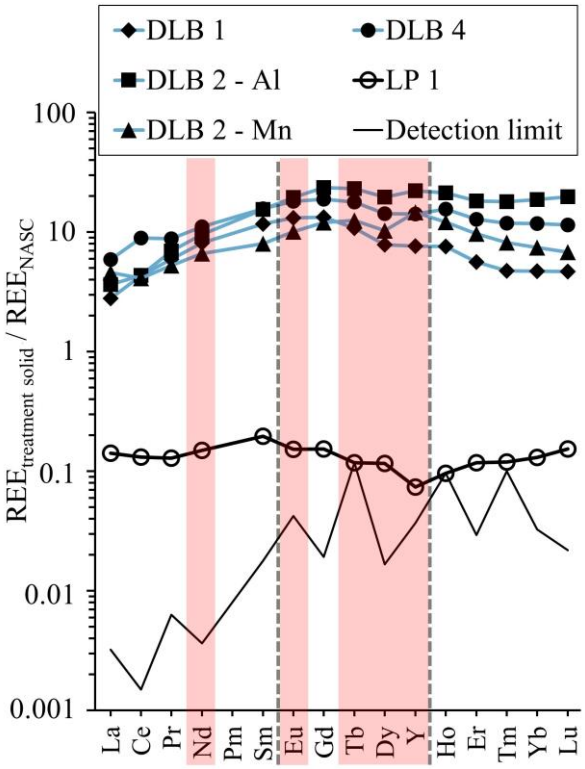

Figure 4 REE concentrations in treatment solids normalized to NASC REE concentrations. Vertical dashed lines divide light REE (left), middle REE (center), and heavy REE (right). Energy critical REE are highlighted in pink. The solid line is detection limits normalized to NASC.

Vertical flow ponds (VFPs) treat low pH CMD with elevated Fe, Al, and/or Mn concentrations by microbial respiration and limestone dissolution. Microbial aerobic respiration in an organic substrate removes DO to limit dissolved Fe(II) and Mn(II) oxidation and precipitation

in limestone, maintaining the reactivity and porosity of the limestone (Hedin et al., 2013). DO concentrations and pH values in VFP-1 and VFP-2 effluent were 0.6 mg/L and 0.1 mg/L, and 6.3 and 6.8, respectively (Table 2). Therefore, the aqueous geochemical conditions in the limestone layer of these sites are anoxic/suboxic and circumneutral.

When effluent concentrations are normalized to influent concentrations, VFP-1 and -2 remove an average of 60% Fe, 99% Al, 9% Mn, and 95% total REE (Table 2) with lower Y removal relative to other REE (Figure 3). Treatment solids were not available for sampling from VFP-1 and -2 so total REE concentrations in the VFP treatment solids were estimated using a mass balance approach. This calculation assumed Fe, Al, Mn, and Si was removed (influent minus effluent) as goethite (FeO(OH) (Kairies et al., 2005), Al hydroxide sulfate ($Al(OH)(SO_4)$) (Pu et al., 2010), birnessite (MnO_2) (Cravotta & Trahan, 1999; Tan et al., 2010), and silica (SiO_2), respectively, and 30% LOI (average from all treatment solids measured in this study). To evaluate the accuracy of this calculation, identical calculations using influent and effluent data from two other treatment systems sampled in this study were compared to total REE concentrations measured by lab analysis. Calculated and measured values from these two treatment systems agreed to within 15%. Calculated REE concentrations in treatment solids are noted in the text and figures. Calculated REE concentrations in the precipitated solids of VFP-1 and VFP-2 are ~1,500 and ~800 ppm, respectively.

Drainable limestone beds (DLBs) treat low pH CMD with dissolved Fe, Al, and/or Mn by calcite dissolution (Hedin et al., 2013). The limestone beds are open to the atmosphere, and dissolved Fe, Al, and Mn are precipitated via oxidation and hydrolysis reactions within the limestone. DO concentrations and pH values in the effluents of DLB-1, DLB-2, and DLB-3 indicate that the geochemical conditions within the limestone bed are circumneutral and oxic

(Table 2). When effluent concentrations are normalized to influent concentrations, DLB-1, -2, and -3 remove an average of 95% Fe, 99% Al, 97% Mn, and 98% REE (Table 2) and preferentially remove Ce relative to other REE (Figure 3). Like VFPs, the DLBs also show less removal of Y relative to other REE (Figure 3).

DLBs are periodically drained empty to remove solids to maintain limestone porosity and reactivity (Hedin et al., 2013). The turbid conditions created by rapidly draining DLBs removes Al solids from the limestone bed to a settling pond but does not remove Mn solids which are armored onto the limestone aggregate. Treatment solids collected from the flush basins at DLB-1 and DLB-2 are 36% and 38% Al_2O_3 and contain 1,103 and 1,849 ppm REE, respectively (Figure 2). Mn-rich coating material physically removed from the limestone at DLB-2 contains 26% MnO and 1,798 ppm REE, after subtracting out the contribution of co-extracted limestone (based on elevated C and CaO content and calcite in XRD patterns) (Figure 2; Appendix Figure 2). Treatment solids coating the limestone at DLB-4 contain 7% Fe_2O_3, 31% Al_2O_3, 12% MnO, and 1,952 ppm REE with negligible limestone content (Figure 2). When normalized to NASC, all DLB treatment solids are light REE depleted and do not contain REE anomalies (Figure 4). On a mass basis, DLB treatment solids average 44% middle and heavy REE and 48% critical REE.

2.3.2 Mineralogy and advanced imaging

XRD analysis of treatment solids suggest that the solid phases are largely amorphous (Appendix Figure 2), with minor trace crystalline components (e.g. quartz and calcite), that do not match the overall bulk chemistry of the solids (e.g. Fe-, Al-, or Mn-rich) described in Figure 2. The amorphous or poorly-crystalline nature of the treatment solids in this study are consistent with

previous XRD analyses of treatment solids from passive CMD treatment systems (Cravotta & Trahan, 1999; Kairies et al., 2005; Pu et al., 2010; Tan et al., 2010).

SEM and synchrotron µ-XRF analyses of a CMD passive treatment system solid from this study show a strong correlation between REE and Mn phases. A photo-scan of the cross section of a piece of limestone aggregate from DLB-2 reveals a black coating on the surface of the limestone (Figure 5A). SEM-BSE imaging further demonstrates that the limestone coating is Mn-rich with botryoidal morphology; an identifying characteristic of Mn oxides and ocean ferro-manganese nodules (Hein et al., 2013; Margolis & Burns, 1976; Post, 1999) (Figure 5B). EDS analysis of the Mn-rich coating via SEM does not detect the presence of REE in this surface coating; however, synchrotron µ-XRF mapping captures the 200-300 µm thick Mn-rich coating on the limestone surface (Figure 5C) and the co-localization of REE in those coatings (Figure 5D).

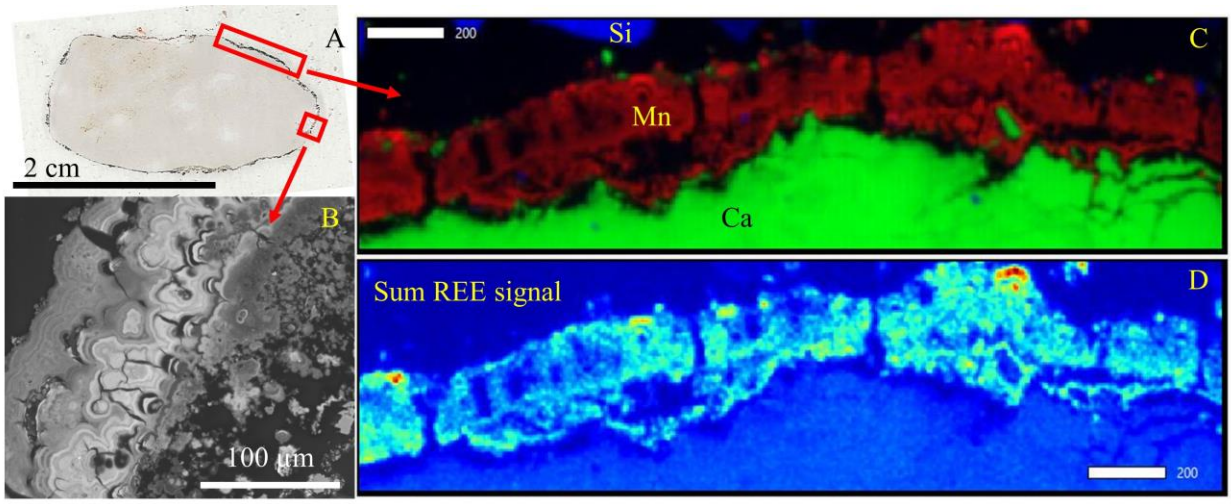

Figure 5 A. Photo-scan of a thin section from cross section of limestone from DLB-2. B. SEM-EDS image of the Mn coating showing botryoidal morphology. C. Tri-colored µ-XRF map collected at an excitation energy of 9500eV, 5 micron step size and 100 msec dwell time with Ca in green, Mn in red, and Si in blue showing Mn accumulating on the edge of the limestone. D. µ-XRF REE map (sum of La, Ce, Nd, Sm, Eu, Gd, Dy, Yb, and Lu counts from PyMCA fitting) with same mapping region as C. The color scale from blue to red represents low to high photon counts. Scale bars in C and D are 200µm.

2.4 Discussion

2.4.1 REE behavior in passive treatment systems

The results presented in this study confirm that the removal of dissolved REE from CMD is pH dependent. Low pH Fe removal technology that maintains pH <3.0 (e.g. LP-1) removes 12% of dissolved REE from AMD (Figure 3). Vertical flow pond (VFP) and drainable limestone bed (DLB), passive treatment technologies that raise pH to >6.0 using limestone dissolution, removed >90% of dissolved REE from AMD (Figure 3), which is corroborated by data from other systems as well (Cravotta & Brady, 2015).

The near complete removal of dissolved REE both in anoxic and oxic conditions in VFPs and DLBs, respectively, suggests that dissolved REE removal occurs under a range of redox conditions (Table 2; Figure 3). In addition to field DO measurements (Table 2), the presence or absence of preferential Ce removal can be used as a proxy for the redox conditions in treatment systems (Figure 3). Ce is redox sensitive and may oxidize and hydrolyze from $Ce(III)_{(aq)}$ to $Ce(IV)O_{2(s)}$ in circumneutral, oxic environments (Bau & Koschinsky, 2009). Preferential Ce removal in DLBs (Figure 3) suggest that Ce is oxidized and hydrolyzed and that the geochemical conditions in DLBs are circumneutral and oxic. Iron and/or manganese oxides, present in DLB-2 and DLB-3, can scavenge Ce and oxidize Ce(III) to Ce(IV) (Bau & Koschinsky, 2009; Ohta & Kawabe, 2001). The absence of preferential Ce removal in VFPs (Figure 3) is consistent with anoxic geochemical conditions that prevent the oxidation of Ce(III).

The presence of organic matter in VFPs could also indicate that organic complexes are important in these systems. Humic acid-REE complexes can suppress Ce anomalies even in the presence of Mn and Fe oxides (Davranche, Pourret, Gruau, & Dia, 2004; Davranche et al., 2008). Additionally, REE can bind to humic acid at pH <4 (Pourret & Martinez, 2009) suggesting REE could be removed in the organic matter portion of VFPs. Additional work on the distribution of REE in VFPs, such as detailed sampling of VFP substrate and/or sequential extractions, will be important to determine where REE accumulate in these systems.

The anomalously low Y removal observed in both DLBs and VFPs has been seen in REE sorption studies in seawater (Bau, 1999; Bau, Koschinsky, Dulski, & Hein, 1996b) and mine drainage (Vesper & Smilley, 2010). This phenomenon is poorly understood but may be due to the weak surface complexation of Y (Bau & Koschinsky, 2009).

The pH dependent removal of REE from AMD in a range of redox conditions could be used to improve the design of treatment systems optimized to remove REE from solution. For example, circumneutral, anoxic conditions could be used to promote the removal of redox-insensitive metals (e.g. REE and Al), and limit the removal of redox-sensitive metals (e.g. Fe and Mn).

2.4.2 REE in treatment solids

Setting pond (SP) systems do not create treatment solids with high REE concentrations (Figure 2) because this technology is primarily used to treat circumneutral mine drainage with low dissolved REE (Table 2) (Hedin et al., 2013). Previous studies have shown that REE are rapidly adsorbed or co-precipitated by Fe(III) hydroxides (e.g. goethite and ferrihydrite) in circumneutral conditions (Bau, 1999; de Carlo et al., 1998; Verplanck et al., 2004); similar to the geochemical conditions in SP-1. In this study, REE concentrations in treatment solids from SP-1 are highest near the influent of the systems and decrease through the system. This suggests REE are rapidly removed with Fe(III) hydroxides at circumneutral pH (Figure 2) and is consistent with their adsorption by goethite (Liu, Pourretc, Guoa, & Bonhourec, 2017; Verplanck et al., 2004). Therefore, any potential REE recovery from SP treatment solids should be targeted near the influent of these systems where pH increases rapidly owing to CO_2 outgassing and, correspondingly, Fe(II) oxidation and Fe(III) accumulation take place (Cravotta & Brady, 2015).

Low pH Fe removal (LP) systems do not produce treatment solids with high REE concentrations (Figure 2) because dissolved REE are not removed from AMD in these systems (Figure 3). This is consistent with previous studies showing both synthetic (Bau, 1999; de Carlo et al., 1998) and natural (Verplanck et al., 2004) Fe(III) hydroxides precipitated at low pH (e.g.

schwertmannite) do not remove dissolved REE from solution. Thus, treatment solids from LP systems should not be targeted for REE recovery. However, these systems could be used as a pre-treatment to remove dissolved Fe for subsequent downstream REE recovery using co-precipitation of REE with other dissolved metals (Al and Mn). For example, LP-1, increases the REE/Fe ratio by 61% by removing 45% Fe but only 11% REE (Table 2). Increasing retention time in the systems could remove more Fe and further increase the REE/Fe ratio.

Vertical flow pond (VFP) and drainable limestone bed (DLB) systems create treatment solids with high REE concentrations that could be targeted for REE recovery (Figure 2). In the circumneutral, anoxic geochemical conditions characteristic of VFPs, there is limited removal of redox-sensitive metals, such as Fe and Mn, and near complete removal of dissolved REE and Al from solution (Table 2; Figure 3), producing treatment solids with high REE concentrations. In the circumneutral, oxic geochemical conditions characteristic of DLBs, there is near complete removal of Fe, Al, Mn, and REE (Table 2; Figure 3), and both Al- and Mn-rich treatment solids are enriched in REE.

Aluminum hydroxides formed in mine drainage environments have been reported to sequester REE in previous studies (Ayora et al., 2016). Synchrotron μ-XRF from this study reveal that REE can also be associated with Mn solid phases in CMD treatment solids produced from DLB passive treatment systems (Figure 5). The REE enrichment is not associated with specific mineral grains (e.g., monazite) that have been identified in other novel REE sources such as coal fly ash (Montross, Verba, Chan, & Lopano, 2018; Stuckman et al., 2018; Zhang & Honaker, 2018). Along with the non-crystalline nature of the Mn oxides, this suggests that REE are diffusely distributed in the Mn-rich treatment solids cemented onto aggregate in DLB-2. However, the exact removal processes of REE by Mn and Al compounds by surface sorption or solid-solution

substitution into the mineral structure remains unclear. In marine systems, REE are associated with Fe and Mn oxide phases in ocean ferro-manganese nodules (Bau & Koschinsky, 2009) and likely accumulate on these solids via surface complexation (Bau et al., 1996b). Additional microanalysis work on the associations between REE and geochemically diverse treatment solids will be important to reveal co-associations and inform targeted extraction methods such as the reductive and/or acid dissolution of Fe/Mn phases (Senanayake, 2011; Zhang & Cheng, 2007). The REE enrichment of both Al and Mn solid phases in DLB treatment solids suggest that these are important phases for REE removal in passive CMD treatment systems.

2.4.3 REE partitioning in treatment solids

Total REE enrichment in treatment solids is dependent on treatment technology (e.g. LP vs DLB). However, individual REE can be uniquely partitioned into solids in mining environments (Prudêncio et al., 2015; Romero, Prol-Ledesma, Canet, Alvares, & Pérez-Vázquez, 2010; Verplanck et al., 2004). In this study, REE concentrations in treatment solids (REE_S) are normalized to REE concentrations in influent CMD (REE_{IN}) to show individual REE partitioning into treatment solids (Figure 6) (Bau, 1999). Although there is anomalously high Ce removal and anomalously low Y removal in DLBs when comparing effluent and influent water samples (Figure 3), corresponding positive Ce and negative Y anomalies are not observed in REE_S/REE_{IN} patterns (Figure 6). Mass balance calculations (($REE_{IN} - REE_{OUT}$) / REE_{IN}) for DLB-1, DLB-2, and DLB-3, show that the anomalous removal of Ce and Y in DLBs (Figure 3) would result in negligible Ce and Y anomalies in corresponding treatment solids. In addition, REE concentrations in influent and effluent CMD samples are instantaneous measurements while REE concentrations

in treatment solids integrate REE removal over longer, multi-season time periods complicating Ce and Y relationships between water samples and treatment solids.

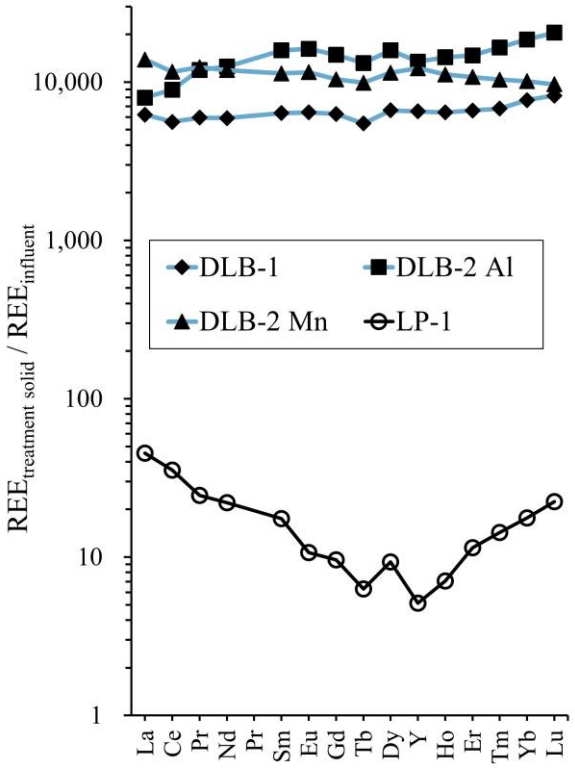

Figure 6 REE concentrations in treatment solids (ppm) normalized to influent CMD REE concentrations (mg/L).

The overall REE patterns in Figure 6 show that LP-1 does not effectively concentrate REE into treatment solids, especially for middle REE, whereas DLB technologies effectively concentrate REE into treatment solids. Although both Al- and Mn-rich treatment solids from DLB-2 accumulate REE, Figure 6 demonstrates that the Al-rich treatment solids accumulate heavy REE more effectively than the Mn-rich treatment solids. De Carlo, Wen, and Cowen (2000) reported enhanced removal of dissolved heavy REE compared to light REE at pH <7.5 by synthetic ferric hydroxide in marine conditions. Field observations during the excavations of operating

DLBs show that treatment solids near the influent of DLBs can be white (Al-rich treatment solids) and transition to black (Mn-rich treatment solids) further from the influent. If heavy REE are also preferentially removed from CMD by Al solids at lower pH, dissolved Al and heavy REE could be preferentially co-precipitating near the influent of DLBs enriching Al solids in heavy REE.

2.4.4 REE concentration in different treatment systems (passive vs. active)

To complement the passive systems sampled in this study, we aggregated existing REE data from additional passive and active CMD treatment systems to determine how treatment technology may impact REE concentrations in treatment solids. We compared the performance of both passive (SP, LP, VFP, DLB) and active (lime) treatment systems by calculating REE solids concentration factors (CF_s) for each system (see methods for a complete description). For the 17 treatment systems included in this study CF_s range from 0.01 to 33 and total REE concentrations (calculated from Y concentrations) in the solids range from 88 to 2,194 ppm.

Plotting CF_s and total REE calculations suggest four groups of treatment technologies (Figure 7): (1) LP systems with low CF_s and total REE concentrations, (2) lime (CaO, $Ca(OH)_2$) systems with low to moderate CF_s and total REE concentrations, (3) SPs with high CF_s and low total REE concentrations, and (4) DLBs and VFPs with moderate CF_s and high total REE concentrations. As discussed above, LP systems do not concentrate REE into treatment solids resulting in low CF_s and total REE concentrations. SPs have high CF_s but produce treatment solids with low total REE concentrations because this technology is primarily used to treated circumneutral CMD with low REE concentrations. DLBs, VFPs, and lime systems all utilize alkaline reagents to treat acidic influent but produce solids with markedly different REE CF_s and total REE concentrations.

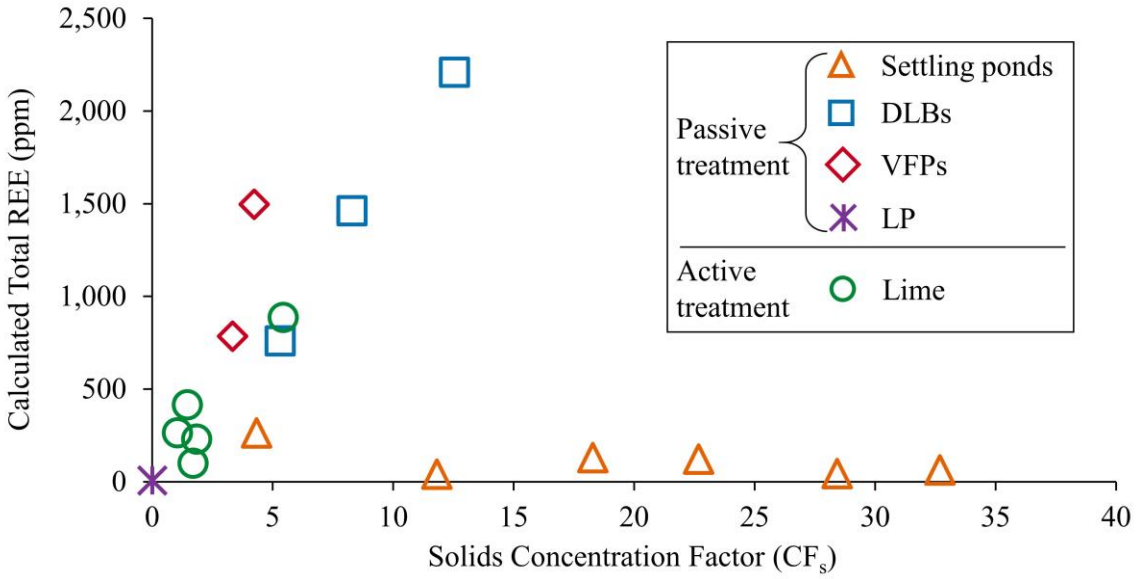

Figure 7 Solids concentration factors (CF_s) and total REE concentrations in treatment solids produced from various CMD treatment technologies. See methods section 2.4 for a description of CF_s. Total REE concentrations are calculated from Y concentrations using the relationship in Appendix Figure 1. VFP data is calculated using a mass balance approach described in the methods section.

The passive treatment of low-pH CMD with limestone dissolution (VFPs and DLBs) have the potential to concentrate REE into treatment solids about three times more effectively than active systems that use lime and can produce treatment solids with about three times higher REE concentrations (Figure 7). In active treatment systems, lime addition creates a high pH, high Ca^{2+}, high SO_4^{2-}, weakly carbonate-buffered system resulting in nontargeted precipitation (e.g., calcite, gypsum, $Mg(OH)_2$). The additional precipitation, together with unreacted lime, will dilute the final REE concentrations in treatment solids from lime systems. However, limestone dissolution from passive treatment systems creates a bicarbonate-buffered system where nontargeted precipitation is minimal. Therefore, DLB and VFP systems treating low-pH, metal contaminated CMD via limestone dissolution concentrate REE most effectively in treatment solids.

2.4.5 CMD treatment solids as potential REE resources

High concentrations of total REE and high % critical REE in CMD treatment solids suggest they are a promising REE recovery source compared to many conventional and newly proposed REE sources. Figure 8 shows that total and critical REE concentrations in CMD treatment solids are generally higher than US and China coals (Dai et al., 2008; Finkelman, 1993), ocean ferromanganese nodules (Bau et al., 2014), and coal fly ash (Stuckman et al., 2018) and are comparable to deep sea muds (Takaya et al., 2018). Although total REE concentrations are less than those for conventional carbonatite sources, the CMD treatment solids evaluated in this study contain an average 48% critical REE (Nd, Eu, Tb, Dy, Y) whereas carbonatites typically contain <20% (Ault et al., 2015; Bao & Zhao, 2008; Castor, 2008; Lynas Corporation Ltd., 2012). Critical REE in CMD solids approach that of ion adsorbed clay deposits (~75%) which currently provide a substantial portion of the world's REE resources (Bao & Zhao, 2008; Dutta et al., 2016; Long, Gosen, Foley, & Cordier, 2010). Additionally, treatment solids are low in radioactive elements U and Th with concentrations averaging 6.1 ppm (±6.9 ppm) and 10.2 ppm (±8.8 ppm), respectively, compared to >300 ppm Th for some carbonatite deposits (Ault et al., 2015). High proportions of easily leachable critical REE and low radioactivity are what make small ($<10^7$ kg of ore) ion-absorbed REE clay deposits economical to mine (Papangelakis & Moldoveanu, 2014; Wall, 2014; Yang et al., 2013). High proportions of critical REE and low radioactivity could also make CMD treatment solids attractive REE sources.

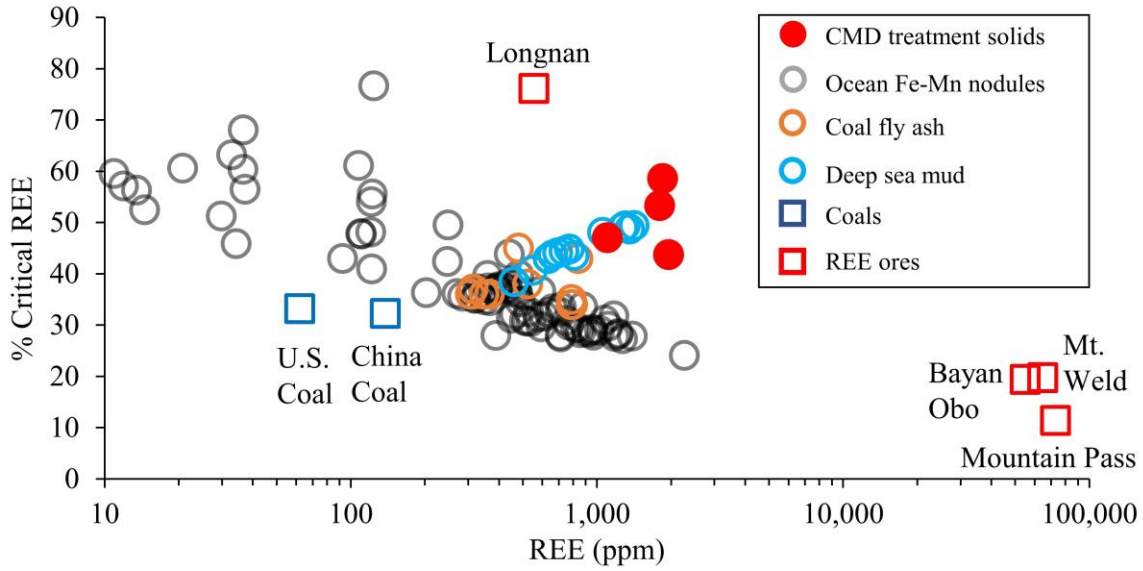

Figure 8 Total REE concentrations vs. % critical REE (Y, Nd, Dy, Eu, Tb) for CMD treatment solids, coal fly ash (Stuckman et al., 2018), ocean Fe-Mn nodules (Bau et al., 2014), deep sea mud (Takaya et al., 2018), average U.S. and China coals (Dai et al., 2008; Finkelman, 1993), and mined ores (Ault et al., 2015; Bao & Zhao, 2008; Castor, 2008; Dutta et al., 2016; Long et al., 2010; Lynas Corporation Ltd., 2012). Longnan is an ion absorbed ore. Mountain Pass and Bayan Obo are carbonatite ores and Mt. Weld is a carbonatite laterite ore. LP-1 data not included as treatment solids from LP systems should not be targeted for REE recovery.

2.5 Conclusions

We report rare earth element data from eight passive coal mine drainage (CMD) treatment systems to determine the geochemical conditions required for REE sequestration and microanalysis work on selected CMD solids produced from these systems to identify REE-enriched phases for potential REE recovery. REE removal in passive treatment systems is pH dependent and redox independent. If pH is raised >6.0 during the treatment process, >90% REE are sequestered in treatment solids. Passive treatment systems using limestone to neutralize acidity can concentrate REE in treatment solids about three times more effectively than active

treatment systems using lime to neutralize acidity. These limestone-based passive systems, such as drainable limestone beds and vertical flow ponds, can produce treatment solids with REE concentrations up to 1,950 ppm and with up to 55% energy critical REE and 56% middle and heavy REE. Both Al- and Mn-rich treatment solids produced from passive systems can be enriched in REE and in Mn-rich treatment solids, REE are diffusely distributed in the Mn-rich layer cemented onto limestone aggregate. CMD treatment solids can contain higher REE concentrations and higher % critical REE compared to many other novel REE sources (e.g., ocean Fe-Mn nodules, coal fly ash, deep sea muds, and coal) and this study indicates that REE in CMD treatment solids represent a substantial REE recovery opportunity. The recovery of REE from treatment solids is an opportunity to transform mine drainage, an environmental challenge and economic liability, into an asset, further spurring the treatment of polluted water.

2.6 Acknowledgements

This research was supported by a University of Pittsburgh Mellon Predoctoral Fellowship, the Dr. J. Frederick and Ann Sarg Research Award from The University of Pittsburgh's Geology and Environmental Science Department, a CRDF grant from the University of Pittsburgh (RCC), logistical support and data from Hedin Environmental, and an appointment by the U.S. Department of Energy (DOE) Postgraduate Research Program at the National Energy Technology Laboratory administered by the Oak Ridge Institute for Science and Education (ORISE). The synchrotron work was conducted on beamline 2-3 at the Stanford Synchrotron Radiation Lightsource, SLAC national Accelerator laboratory, which is supported by the U.S. Department of Energy, Office of Sciences, Office of Basic Energy Sciences under Contract No. DE-AC02-76SF00515. We thank

Dr. Charles Cravotta III for sharing data and for a detailed review of an earlier version of this manuscript. The manuscript was improved by comments and suggestions from Dennis Kraemer and an anonymous reviewer. We also thank Dr. Wei Xiong (NETL) for her aid in SEM analyses. Use of trade, firm, or product names is for descriptive purposes only and does not imply endorsement by the U.S. Government.

This chapter was published in the International Journal of Coal Geology, 208, Benjamin C. Hedin, Rosemary C. Capo, Brian W. Stewart, Robert S. Hedin, Christina L. Lopano, and Mengling Y. Stuckman, The evaluation of critical rare earth element (REE) enriched treatment solids from coal mine drainage passive treatment systems, Copyright Elsevier, 2019.

3.0 Critical metal recovery potential of Appalachian acid mine drainage treatment solids

3.1 Introduction

The demand for metals such as Mn, Co, Ni, Ga, Cd, Ag, Cu, Se, In and rare earth elements (REE; defined here as the 15 lanthanide elements plus yttrium)(DOE, 2011; Dominish, Florin, & Teske, 2019) is expected to increase sharply in the coming decades due to their use in renewable energy technologies (e.g., wind turbines, electric motors, and batteries) and their limited sources (Fishman & Graedel, 2019). However, mining and refining these metals can have serious impacts on human health and the environment. For example, REE extraction from carbonatite and monazite ores produces large quantities of radioactive waste, uses significant amounts of energy, and is poorly regulated in some regions(Haque et al., 2014; Van Gosen et al., 2017a). The need for both environmentally friendly and geographically diverse REE sources has spurred research into non-traditional feedstocks(Binnemans et al., 2013; Hein et al., 2013; Lin et al., 2018; Stuckman et al., 2018; Takaya et al., 2018), including polluted mine drainage(Ayora et al., 2016; Hedin et al., 2019a; Lefticariu et al., 2019; Stewart et al., 2017; Vass et al., 2019b).

Oxidation and dissolution of sulfide minerals (e.g., pyrite, FeS_2) related to coal and metal mining produces acidity and dissolved metals that pollute waterways around the world with acid mine drainage (AMD)(Younger et al., 2002). In the Appalachian basin in the eastern USA, over two centuries of coal mining has produced thousands of pollution sources that impair over 5,000 km of streams with acidity, metals, and sulfate(EPA, 2015). However, Appalachian AMD also generates between 500 and 3,400 metric tons of REE annually, depending on estimates of total AMD discharge and REE concentrations(Stewart et al., 2017; Vass et al., 2019a). This represents

7% - 41% of annual US consumption of REE in 2018(Gambogi, 2019a, 2019b). Total REE loads for single AMD discharges can be up to 7,000 kg/year with many discharges producing >100 kg/year(Cravotta, 2008a; Cravotta & Brady, 2015; Stewart et al., 2017).

AMD treatment involves pH and redox adjustments to neutralize acidity and accelerate the precipitation and settling of dissolved metals(Younger et al., 2002). This generates significant amounts of solid waste; more than 18,000 metric tons are produced annually in Pennsylvania alone(Stream Restoration, 2018). The management and disposal of these treatment solids incur significant costs to operators(Cravotta et al., 2014). With REE concentrations reported as high as 2,000 mg/kg, these solids could be targeted for REE recovery, and could offset the cost of treating AMD(Hedin et al., 2019a; Vass et al., 2019b).

Although there has been substantial work on identifying and characterizing REE enriched AMD treatment solids, most estimates are based on relatively small sample sizes (<25), or discuss regional trends and do not focus on geochemical trends(Acero, Ayora, Torrentó, & Nieto, 2006; Hedin et al., 2019a; Lozano, Ayora, & Fernández-Martínez, 2019a, 2020; Lozano et al., 2019b; Moraes, Murciego, Álvarez-ayuso, & Ladeira, 2020; Stewart et al., 2017; Vass et al., 2019a, 2019b). Additionally, there is limited work on potential to recover clean energy critical elements (Mn, Co, Ni, Ga, Cd, Ag, Cu, Se) from treatment solids. In this study, we report major and trace element concentrations for 281 AMD precipitates from 94 sites across the Appalachian Basin, with corresponding untreated AMD pH and treatment technology information to determine (1) the relationship between AMD chemistry and clean energy critical concentrations in treatment solids, (2) the impact of treatment technology on REE concentrations and geochemical trends, and (3) potential REE market value in AMD treatment solids. While we focus on REE in AMD treatment solids, we also report on the concentrations and geochemical trends for other clean energy critical

metals. These results can be used to identify promising feedstocks from existing treatment systems and inform the design of new systems optimized to both remediate polluted water and concentrate economic amounts of critical metals in treatment solids.

3.2 Materials and methods

3.2.1 Data sources

Treatment solids chemistry and AMD water chemistry used in this study are compiled from published and unpublished sources (Table 3). Solids chemistry for 281 samples is compiled from Hedin et al., 2019(Hedin et al., 2019a) (n = 11), Stewart et al., 2017(Stewart et al., 2017) (n = 21) and unpublished data from Hedin Environmental (n = 249). For 170 samples, total REE concentrations are calculated from Y concentrations based on a robust linear regression (see details in section 2.2). Paired AMD water chemistry is compiled for 225 samples from Beam, 2019(Beam, 2019) (n = 2), Cravotta and Brady, 2015(Cravotta & Brady, 2015) (n= 2), Cravotta, 2008a(Cravotta, 2008a) (n = 33), Hedin et al., 2019(Hedin et al., 2019a) (n = 13), Stewart et al., 2017(Stewart et al., 2017) (n = 12), www.datashed.org(Stream Restoration, 2018) (an online AMD chemistry data repository; n = 23), and unpublished data from Hedin Environmental (n = 140). Treatment technology for 251 samples is compiled from Hedin Environmental.

Table 3 Data sources for this study and number of samples from each source. Datashed is an online AMD chemistry data repository (Stream Restoration, 2018).

Treatment solids	n	AMD liquid	n	Treatment technology	n
Hedin et al., 2019	11	Beam, 2019	2	This study	251
Stewart et al., 2017	21	Cravotta and Brady, 2015	2		
This study	249	Cravotta, 2008a	33		
		Hedin et al., 2019	13		
		Stewart et al., 2017	12		
		www.datashed.org	23		
		This study	140		
Total	281		225		251

3.2.2 Treatment solids chemistry

Treatment solids were grab samples from AMD treatment systems or naturally attenuated (untreated) locations collected by shovel or bucket and dried at 100°C until weight was constant. If limestone aggregate was collected, it was sieved to 2 mm after drying to separate treatment solids (<2 mm) from the aggregate (>2 mm). AMD pH was measured by calibrated pH meters in the field.

The treatment solid samples collected in this study were analyzed by Activation Laboratories (accredited by the Canadian Association for Laboratory Accreditation) by ICP-MS and/or ICP-OES. When these samples were combined with literature data from Hedin et al., 2019, and Stewart et al., 2017, thirteen of the samples have all REE concentrations (Y+lanthanides) measured by ICP-MS (Table 2). For 35 samples with concentrations for 9 out of 15 REE (Y, La, Ce, Na, Sm, Eu, Tb, Yb, Lu) measured by instrumental neutron activation analysis (INAA), missing REE concentrations were interpolated as the weighted average between the two nearest redox-insensitive REE_{NASC} ratios (see Appendix Table 4 and Appendix Table 5 for equations and

justification) for calculation of total REE concentrations. For 45 samples, concentrations of between 2 and 8 of the REE are above detection limits, and 170 samples have only Y concentrations measured by ICP-OES or ICP-MS (Appendix Table 4). Because the relationship between Y and total REE concentrations is robust (r^2 = 0.88; p<<0.001; Figure 9), total REE concentrations were estimated for these 215 samples as follows:

$$Total\ REE\ (ppm)\ =\ Y\ (ppm)\ \times\ 4.1063$$

The regression between Y and total REE concentrations is nearly identical for samples with REE only measured by ICP-MS versus using the methods described above (Figure 9).

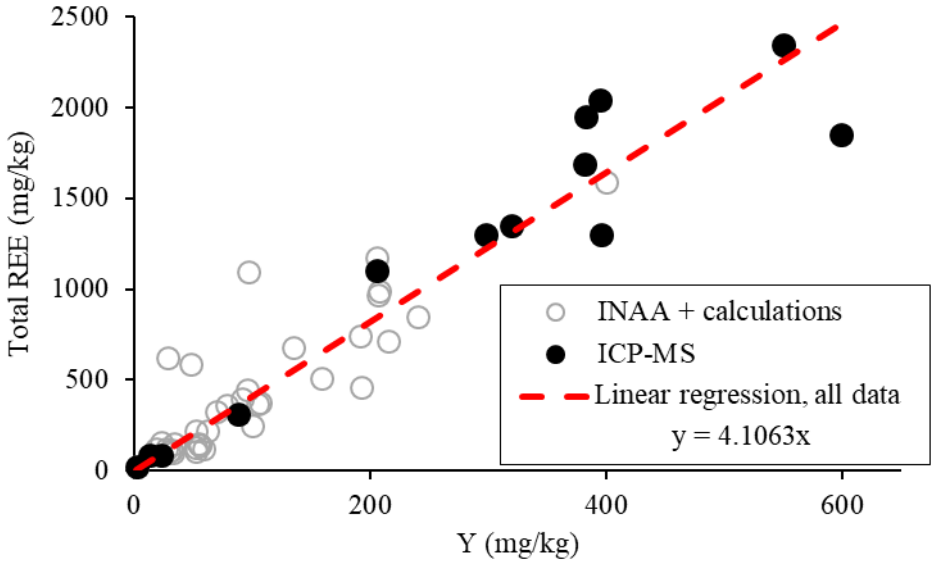

Figure 9 Linear regression between Y and total REE concentrations (both ICP-MS and INNA + calculations; r^2 = 0.88, p<<0.001). The regression with only ICP-MS measured data is y = 4.1022x; r^2 = 0.88. Sample analyzed using ICP-MS have all 15 REE measured. Samples analyzed using INAA points have 9 REE measured (Y, La, Ce, Nd, Sm, Eu, Tb, Yb, Lu) and remaining REE concentrations are calculated as detailed in methods.

Table 4 Appalachian AMD treatment solid samples and analyses included in this database.

REE concentrations above detection limits	Number of samples	Analysis
Total REE (Y + all lanthanides)	13	Correlate total REE with Y
Full INAA analysis (Y, La, Ce, Nd, Sm, Eu, Tb, Yb, Lu)	35	Calculate missing REE via Appendix Table 4 and correlate with Y
Partial REE (>1 REE, <9 REE)	45	Calculate total REE using Y
Y only	170	Calculate total REE using Y
All REE below detect	18	Unused

Samples were further classified into Al- and Mn- rich (>10% Al+Mn) and Fe-rich (>10% Fe and <10% Al+Mn) to determine if major element composition impacts the Y and REE relationship. While the slopes of the regressions are slightly different (4.19 for Al- and Mn-rich and 3.36 for Fe-rich; Appendix Figure 3), the linear regression using all data (Figure 1) is appropriate to calculate total REE concentrations from Y for the entire dataset.

3.2.3 Stepwise regression

Multivariate linear regressions constructed using stepwise linear regression to assess co-associations between REE, critical metals, and associated mineralogy can inform the search for valuable AMD treatment solids. Independent variables chosen for this analysis were concentrations of Si, Al, Fe, Mn, Mg, Ca, and LOI (loss on ignition; volatile components (e.g. H_2O, CO_2) from hydrated minerals, carbonate, and/or organic matter). Clean energy-critical elements considered as dependent variables were REE, Co, Ni, Cu, Ga, Cd, and Ag.

Only samples for which the sum of Si, Al, Fe, Mn, Mg, and Ca oxides and LOI was greater than 90% were used in the regression; this requirement excluded three samples out of 281. The

stepwise regression function in Matlab 2019a was used to generate multivariate linear regressions that maximizes explanatory power. The inclusion/exclusion of independent variables is determined by calculating p values for the models with and without an independent variable. If the weight of the variable is significantly statistically different from zero ($p < 0.05$), it is added to the model.

3.2.4 Economic evaluation

In-situ and basket REE prices were calculated based on average prices from the 2008 to 2015 USGS Mineral Yearbooks following the methodology of Vass et al. (2019) for 48 treatment solid samples with complete REE concentrations, and for 58 REE mineral resources that are currently under development(Lifton & Hatch, 2015).

3.3 Results and discussion

3.3.1 Characteristics of AMD treatment solids

Complete data from the 281 treatment solid samples from 94 AMD treatment systems in northern Appalachia are presented in Supplementary Table 4. A similar database with 629 treatment solid samples from 119 sites across Appalachia was compiled by West Virginia University and is freely available through the US Department of Energy's National Energy Technology Laboratory Energy Data eXchange ("National Energy Technology Laboratory, US Department of Energy, Rare Earth Element Database,")("National Energy Technology Laboratory,

US Department of Energy, Rare Earth Element Database,")("National Energy Technology Laboratory, US Department of Energy, Rare Earth Element Database,")("National Energy Technology Laboratory, US Department of Energy, Rare Earth Element Database,")("National Energy Technology Laboratory, US Department of Energy, Rare Earth Element Database,")("National Energy Technology Laboratory, US Department of Energy, Rare Earth Element Database,")("National Energy Technology Laboratory, US Department of Energy, Rare Earth Element Database,"). Although this database is extensive, it does not report Mn or volatiles, which can be substantial components of treatment solids, and the only trace metals reported are REE and Co. Thus, only the 281 samples compiled in this study are used in this analysis.

Major constituents in Appalachian AMD treatment solids include Al, Fe, Mn, Ca, Mg and Si. This is reflected in the mineralogy of the solids, which generally includes amorphous Al-, Fe-, Mn-, Ca-, and Mg-hydrated oxides and hydroxides, Ca and Mg carbonates and/or hydroxides, gypsum, and silica(Kairies et al., 2005; Pu et al., 2010; Tan et al., 2010). Percentile concentrations of critical metals are provided in Table 3. Manganese (Mn), a major metal pollutant in Appalachian AMD, was as high as 43% in the solids with two samples above the average global sedimentary Mn ore deposit value of 24%(Cannon, Kimball, & Corathers, 2018). The two highest Co concentrations (5,050 mg/kg and 2,940 mg/kg) were comparable to low grade Co ores (2,000-10,000 mg/kg)(Slack, Kimball, & Shedd, 2017). Additionally, Co concentrations in six samples were above laboratory reporting limits (1,000 mg/kg). Among other critical metal resources, Ni (≤ 6,800 mg/kg) and Cu (≤ 740 mg/kg) are below traditional laterite (8,300-18,000 mg/kg)(Berger, Singer, Bliss, & Moring, 2011) and porphyry (1,000-16,000 mg/kg) sources(Singer, Berger, & Moring, 2008), respectively. Gallium concentrations (≤ 17 mg/kg) are equivalent to or lower than continental crust concentrations (17-18 mg/kg)(Foley, Jaskula, Kimball, & Schulte, 2017). Both

Cd (≤ 13 mg/kg) and Ag (≤ 4.4 mg/kg) are already recovered as byproducts from refining Zn and Zn/Pb ores, respectively(Goonan, 2014; Shiel, Weis, & Orians, 2010). All In and Se measurements were at or below detection limits (0.2 mg/kg and 3 mg/kg, respectively).

Table 5 The range in critical metal concentrations for AMD treatment solids. Percentile data were calculated from samples with concentrations above detection limits. *Six samples have greater than 1,000 mg/kg Co.

Percentile	REE	Mn	Co*	Ni	Cu	Ga	Cd	Ag
	----------mg/kg----------							
100 (maximum)	2,344	427,497	5,050	6,720	731	17	13.1	4.4
75	255	2,168	94	355	57	15	2.0	0.7
50	115	620	14	32	17	13	1.7	0.5
25	61	232	5	14	9	6	1.3	0.5
0 (minimum)	4	100	1	4	1	4	0.5	0.3
# analyses	261	278	98	82	82	11	74	82
Minimum detection limit (mg/kg)	1	100	1	1	1	1	0.5	0.5
# below detection	0	1	5	0	15	0	7	60

Although untreated AMD has a higher REE content than natural waters, treatment solids are enriched by several orders of magnitude relative to either (Figure 2). Total REE concentrations in treatment solids range from 4 to ~2,300 mg/kg (Table 3). The highest concentrations of REE are associated with solids with substantial Al, and Mn content (Figure 3). While the REE concentrations in these enriched samples are well below the concentrations in carbonatite and monazite REE ores (30,000 mg/kg to 80,000 mg/kg), they are similar to concentrations in ion-absorbed clay deposits in Southern China (500 mg/kg to 4,000 mg/kg)(Van Gosen et al., 2017a). Ion absorbed clay REE deposits in South China are economical to exploit, in part, because of their high proportion of high-value heavy REE (Tb, Dy, Y, Ho, Er, Tm, Yb, Lu); they contain about

80% compared to under 2% for carbonatite/monazite ores(Bao & Zhao, 2008; Castor, 2008; Lynas Corporation Ltd., 2012). Treatment solids are similarly enriched in heavy REE (average 49%)(Hedin et al., 2019a; Stewart et al., 2017).

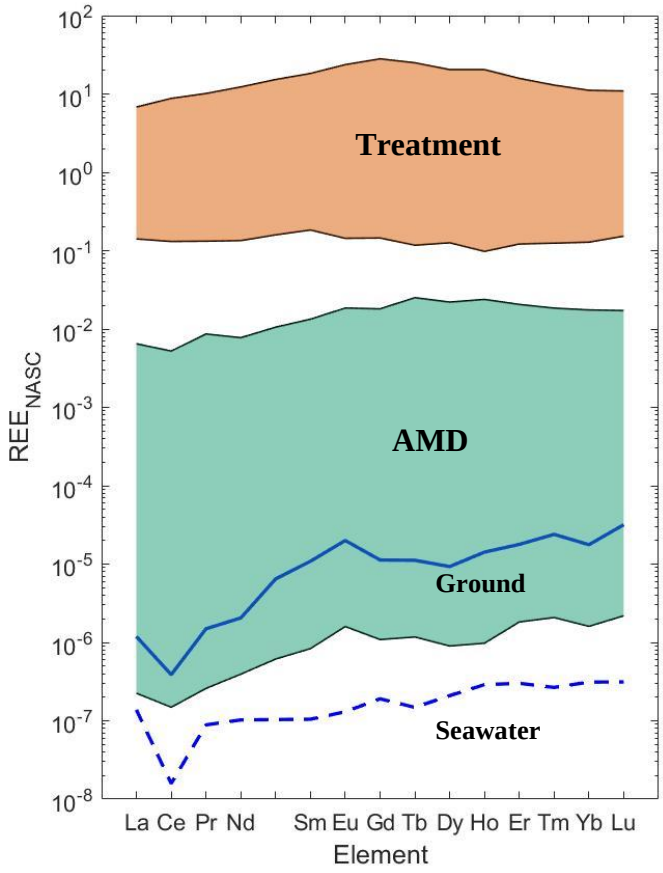

Figure 10 North American Shale Composite normalized REE patterns for the seawater and groundwater samples with median total REE concentrations(Noack et al., 2014), AMD liquid samples with the highest and lowest total REE concentrations(Cravotta, 2008b; Cravotta & Brady, 2015; Hedin et al., 2019a; Stewart et al., 2017), and treatment solids with the highest and lowest total REE concentrations from this study. Y is not included in this plot.

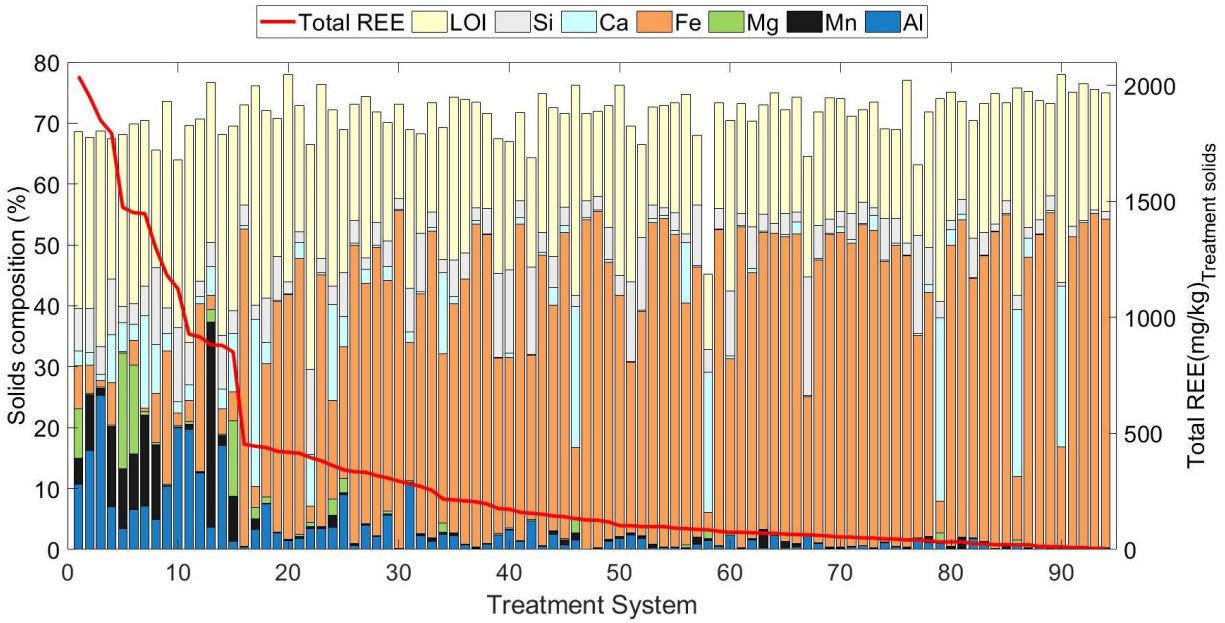

Figure 11 Average AMD treatment solids content and total REE concentrations from 94 treatment systems or naturally attenuated sites across northern Appalachia.

Treatment solids also contain a high proportion of green energy technology-critical REE (Y, Nd, Dy, Eu, and Tb)(DOE, 2011). Total concentrations of critical REE range from 7 mg/kg to ~1,000 mg/kg and make up 27% to 67% of total REE concentrations in the solids (Appendix Figure 4); Yttrium and Nd alone make up 26 ±10% and 16±4% of total REE concentrations, respectively. The proportion of green energy-critical REE in treatment solids are comparable to other unconventional REE feedstocks currently under consideration, such as coal fly ash, deep sea muds, and ocean Fe-Mn nodules,(Bau et al., 2014; Stuckman et al., 2018; Takaya et al., 2018) and approaches that of ion-absorbed REE clays (76%) in China(Bao & Zhao, 2008). Additionally, concentrations of uranium and thorium in carbonatite and monazite REE ores can be up to 400 mg/kg (Castor, 2008) and present an environmental challenge when processing these ores. AMD

precipitates are significantly lower in U (5.8 ±5.9 mg/kg; max. 26 mg/kg) and Th (4.3±7.2 mg/kg; max. 51 mg/kg; Appendix Figure 5).

These data suggest that while treatment solids can be enriched in Mn and Co, there are very few samples in this database with concentrations comparable to ores. However, REE concentrations are comparable to currently exploited ores and could be prioritized for recovery from AMD treatment solids.

3.3.2 Geochemical relationships

The multivariate linear regressions are shown in Table 4 and have strong prediction power (r^2 >0.60) for REE, Co, Ni, Ga, and Ag. For REE, the multivariate linear regression indicates that treatment solids with high concentrations of Al, Mn, and Mg (positive weights) are likely to have high concentrations of REE, while those with high Si and LOI concentrations are likely to have low concentrations of REE (negative weights). Likewise, higher Mn and Al concentrations are also associated with higher concentrations of Co. However, for Co, Mn is an order of magnitude more important than Al and dominates the multivariate regression.

Table 6 Results of the stepwise linear regression where major element concentrations (%) are used as independent variables to calculate critical metal concentrations (mg/kg). *=p <0.05 †=p<0.01 ‡=p<0.001

	REE	Co	Ni	Cu	Ga	Cd	Ag
Variables	-----Weights-----						
y intercept	234	0.9	1.6	8.9	17.2	1.84	0.51
Si (%)	-12‡	-9.3	-21.4	-2.3	0.2	-0.05	0.00
Al (%)	65‡	18.6†	25.4*	12.0‡	-0.4†	0.01	0.02
Fe (%)	-3	-3.8	-3.4	-0.9	-0.2	-0.01	0.00
Mn (%)	40‡	180.4‡	179.2‡	2.4	0.1	0.28‡	0.16‡
Mg (%)	43‡	-50.4*	-33.3	-6.7	-1.4†	-0.37†	-0.01
Ca (%)	2	7.8	11.2	1.7	0.0	0.04	-0.01*
LOI (%)	-7†	4.6	2.5	3.0	-0.1	0.01	-0.01
Regression r^2	0.70	0.76	0.63	0.33	0.77	0.32	0.99

Previous work on REE in AMD treatment solids shows that REE are associated with Al rich solids(Ayora et al., 2016; Lozano et al., 2019a; Lozano et al., 2019b; Moraes et al., 2020). However, Table 4 shows that solids with high concentrations of Mn and Mg can also have high concentrations of REE. Furthermore, Figure 3 shows that REE enriched solids are typically geochemically complex, containing Al, Mn, Fe, and Mg minerals. This is significant because the presence of a diverse mineralogical assemblage suggests complex REE attenuation mechanisms (e.g. sorption on Fe, Al, and Mn (hydr)oxides) are possible and that both Al- and Mn-rich solids are important to consider when targeting treatment solids for REE recovery.

Cobalt is strongly co-associated with Mn in AMD treatment solids in this study, as is common in ocean and freshwater systems(Lienemann, Taillefert, Perret, & Gaillard, 1997). Although Co and Al are positively correlated, some samples with high Al concentrations have low Co concentrations (Appendix Figure 6). Additionally, the six samples with greater than 1,000 mg/kg Co all contain at least 91,000 mg/kg Mn.

Although organic matter has strong REE chelating abilities(Tanizaki, Shimokawa, & Yamazaki, 1992), LOI is negatively weighted in the REE linear regression and is not well

correlated with total REE concentrations (r = 0.34). Similarly, while dissolved Si concentrations are highest in low pH AMD,(Cravotta, 2008a) Si and total REE concentrations are poorly correlated (r = 0.07). This suggests that Si and LOI dilute, rather than concentrate, REE in treatment solids.

3.3.3 Optimizing REE recovery in treatment solids

Trace metal content and statistical analyses indicate that AMD treatment solids with high Al and Mn concentrations should be targeted for recovery of REE and Co. Additionally, multiple samples collected from single treatment sites indicate that there is low intrasite variability in REE concentrations compared to variability between sites, which suggests that potential REE resource recovery for individual sites could be adequately determined by analyzing a few samples (Appendix Figure 7). Although REE may be uniquely partitioned between solid phases (e.g. preferentially adsorbed onto specific metal oxides), bulk geochemical relationships can inform the identification of treatment solids amenable for REE recovery.

3.3.4 Iron-rich precipitates

While iron oxide can be a strong sorbent of REE and Co (Dzombak & Morel, 1990; Verplanck et al., 2004), Fe in AMD treatment solids is negatively correlated with REE (r = -0.56, $p < 0.01$) and Co (r = -0.41, $p < 0.01$), and iron-rich treatment solids typically contain low total REE and Co concentrations (Figure 3). The reasons for this relate to pH-based treatment of coal mine discharges. Minewaters that are both anoxic (dissolved oxygen <1 mg/L) and circumneutral (pH ~7) are a common occurrence in Appalachia(Cravotta, 2008a). Under these conditions, Fe(II) is

soluble while Al, REE, and Co are minimally soluble and/or are not leached from associated strata. Treatment of this type of mine drainage oxidizes and precipitates Fe, resulting in Fe-rich solids with low REE and Co concentrations. Treatment of low pH, high Fe minewaters solely by microbial Fe(II) oxidation also results in solids with high Fe and low REE and Co concentrations(Hedin et al., 2019a).

3.3.5 Al- and Mn-rich precipitates

REE, Co, Al, and Mn concentrations are highest in low pH discharges because these elements are leached from rock units by acidic minewater(Cravotta, 2008a; Wallrich, Stewart, Capo, Hedin, & Phan, 2020). By neutralizing acidity and raising pH, dissolved metals can be precipitated. At pH 6-9, Al is minimally soluble and precipitates(Cravotta, 2008b); dissolved REE are also removed from solution by adsorption on Fe, Al and/or Mn oxide/hydroxides surfaces and/or co-precipitation with these metals(Ayora et al., 2016; Hedin et al., 2019a; Lozano et al., 2019b; Verplanck et al., 2004). Likewise, dissolved Co is removed from solution by adsorption on Fe/Mn oxide/hydroxide surfaces followed by substitution into Mn oxide structures (Burns, 1976; Lienemann et al., 1997). Mn can be removed at pH >9 by stoichiometric solubility controls(Cravotta, 2008b) or at pH 6-7 by heterogeneous precipitation on biogenic Mn coatings on limestone(Santelli, Webb, Dohnalkova, & Hansel, 2011b; Tan et al., 2010).

3.3.6 Treatment technology

To determine which AMD treatment systems should be prioritized for REE recovery, current treatment technology must also be considered. Because of the pH dependency of REE

concentrations in AMD, solids from systems treating AMD with pH >5 typically contain total REE less than 500 mg/kg, and solids from AMD with pH <5 can have REE concentrations from <500 mg/kg to >2,000 mg/kg (Figure 4). The impact of chemistry and treatment technology described below for REE likely also explain the variability and geochemical relationships for other clean energy critical metals and can inform their recovery from treatment solids.

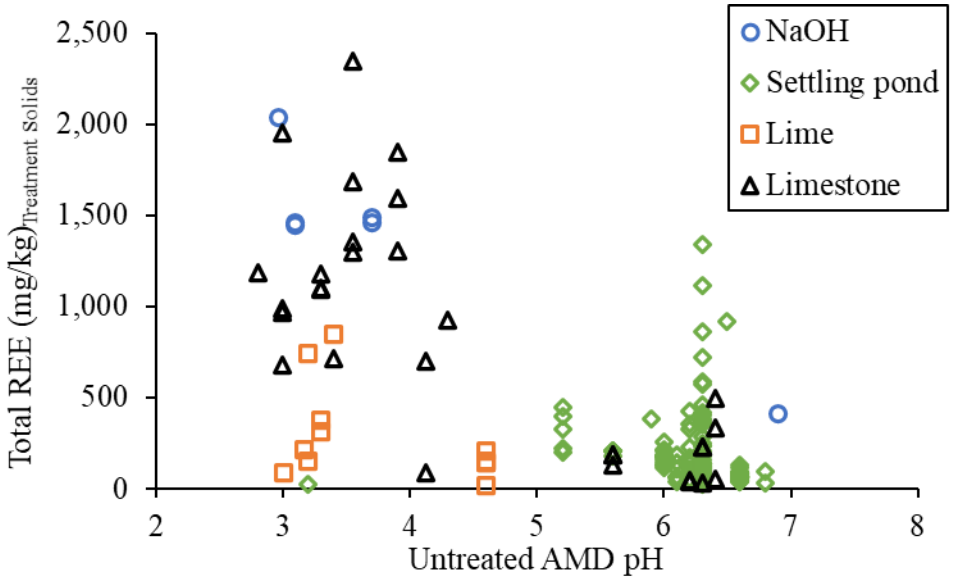

Figure 12 Paired untreated AMD pH and total REE concentrations in the treatment solids for 185 samples from 44 treatment systems using NaOH, lime, limestone, and settling ponds.

The wide range in total REE concentrations in treatment solids produced from pH <5 AMD is explained by the variety of acid neutralization technologies used in treatment. Typical active treatment technologies (in which chemicals are mixed with AMD in reaction tanks) utilized to neutralize acidity are sodium hydroxide (NaOH) or lime (either $Ca(OH)_2$ or CaO). In passive treatment systems limestone (consisting of calcite, $CaCO_3$) is typically used to neutralize acidity.

Systems using lime to neutralize acidity typically produce treatment solids with lower total REE concentrations (283 ± 258 mg/kg) than systems using limestone or sodium hydroxide (1,211 ± 522 mg/kg and 1,578 ± 258 mg/kg, respectively; Appendix Figure 8). Higher average Ca concentrations in lime solids (19% ±9%) compared to those from limestone and sodium hydroxide systems (3-6%) suggest that the lower REE concentrations are due to dilution by calcite and unreacted lime. Calcite commonly precipitates after the addition of lime because of high pCO_2 in minewaters(Cravotta, 2008a). However, modern hydrated lime treatment systems with CO_2 degassing technology and pH-controlled lime dosing can produce solids with low Ca content (5% Ca)(Beam, 2019) which could then potentially increase relative REE content.

Treatment solids produced from pH <5 AMD using sodium hydroxide to neutralize acidity produce solids with high REE. However, Mg concentrations are also high (15% ±4%) compared to the Mg content of solids from limestone and lime systems (<1-3%). This is because systems using sodium hydroxide to raise pH above 9 in order to precipitate Mn as $Mn(OH)_2$. Magnesium, also minimally soluble in this pH range, will precipitate as $Mg(OH)_2$ together with Mn and REE, as observed in the REE multivariate regression (Table 4).

Treatment solids produced from pH <5 AMD using limestone to neutralize acidity typically produce solids with high REE concentrations and low Ca and Mg concentrations (<6%). The bicarbonate buffering range of limestone dissolution minimizes the solubility of Al and Fe, promotes heterogeneous Mn removal, and minimizes Ca and Mg precipitation. Using pumps and excavators to wash treatment solids from limestone beds is a common maintenance task for passive treatment systems and result in solids primarily composed of Al, Mn, Fe, and Si. For these reasons, limestone-based systems produce the treatment solids with both high REE concentrations and low non-target metal concentrations (e.g., Ca, Mg).

3.3.7 REE resources in Appalachian AMD

In situ and basket REE prices can be used to evaluate and compare potential REE sources(Silva, Petter, & Albuquerque, 2018) and can be applied to AMD treatment solids(Vass et al., 2019a). In situ price refers to the REE value in one metric ton of raw material (dry weight); basket price is the REE value in 1 kg of pure REE product, assuming 100% REE can be extracted from the raw material. Because each REE is valued differently, in situ prices depend on REE distribution and concentration and basket prices depend only on REE distribution.

In-situ prices (in $USD) of Appalachian AMD treatment solids range from $3/metric ton to $405/metric ton; basket prices range from $131/kg to $292/kg (Figure 5). In-situ and basket prices of REE ores range from $18/metric to $6,023/metric ton and from $39/kg to $213/kg, respectively(Lifton & Hatch, 2015).

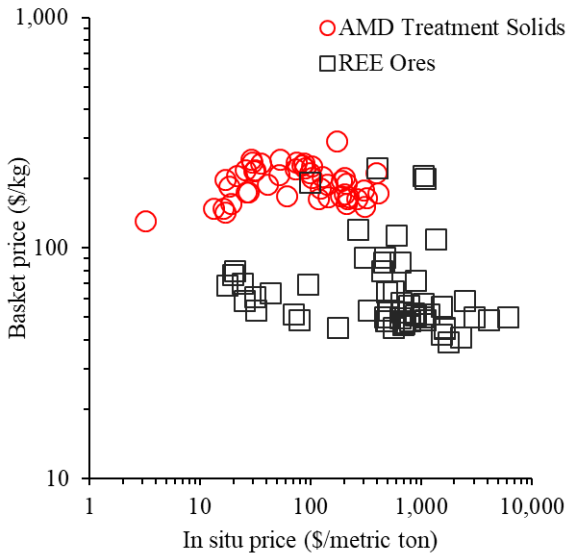

Figure 13 In-situ and basket REE prices of Appalachian AMD treatment solids and developed/developing REE ores from around the world(Lifton & Hatch, 2015).

Although in-situ and basket prices for treatment solids and REE ores are highly variable, there is significant overlap. REE concentrations in treatment solids range from 4 mg/kg to 2,460 mg/kg whereas REE concentrations in ores range from 256 mg/kg to 120,000 mg/kg (12%). However, REE in treatment solids are in a metal hydroxide/oxide matrix that is potentially easier to process than traditional sources which are mostly hosted in silicate or carbonatite igneous rocks(Van Gosen et al., 2017a). Additionally, AMD treatment solids contain low concentrations of U and Th, radioactive elements of concern in many REE ores.

In addition, basket REE prices for treatment solids are two to three times greater than those for REE ores. This is because AMD treatment solids contain a higher proportion of heavy REE (HREE; Tb, Dy, Y, Ho, Er, Tm, Yb, Lu) which are more valuable than light REE (LREE; La, Ce, Pr, Nd, Sm, Eu, Gd). The average HREE/LREE ratios for treatment solids and REE ores are 0.74 (±0.43) and 0.19 (±0.47), respectively. The small range in treatment solid basket prices for the treatment solids is due to their relatively homogeneous source (Pennsylvanian age sedimentary rocks in the Appalachian basin), compared to global REE ores.

In situ prices for Co were calculated using $42.98 USD/kg, the average yearly London Metal Exchange price of Co from 2015 to 2019(US Department of the Interior, 2020). In situ prices range from $4.31x10^{-5}/metric ton to $0.22/metric ton with 97% of samples below $0.05/metric ton. While in situ prices are only one variable in determining the viability of resource extraction and market prices are volatile, the value of clean energy critical metals in AMD solids is driven by REE.

3.3.8 Treatment costs and sustainability

While currently operating AMD systems offer a potentially inexpensive source of REE-enriched solids, the cost and sustainability of AMD treatment are critical factors for future AMD treatment systems engineered for REE recovery. In Appalachia, the cost of using limestone as a neutralization agent is less than 20% of the cost of hydrated lime and sodium hydroxide(Cravotta et al., 2014). Limestone is also inert, compared to caustic sodium hydroxide, and has a lower CO_2 footprint compared to lime which requires the energy-intensive process of limestone calcination(Bosoaga, Masek, & Oakey, 2009). In addition, in order to produce low-Ca solids, the construction of modern lime treatment systems typically cost $10 to $15 million USD with hundreds of thousands of dollars per year in operation and maintenance(Beam, 2019).

An additional sustainability concern is the amount and nature of chemicals used in the processing of treatment solids. In many REE processing chains, the use of mineral acids (e.g., HCl) to solubilize REE accounts for about 40% of the greenhouse gas emissions in the REE processing chain(Haque et al., 2014). Treatment solids from lime and sodium hydroxide systems can contain high concentrations of Ca and Mg hydroxides/carbonates which would need to be dissolved before REE are solubilized at low pH. Treatment solids physically removed from limestone aggregate would require less acid to solubilize REE than other methods.

Although cheaper, the use of limestone to treat large flows of severely contaminated AMD requires more land than lime or sodium hydroxide technologies and additional considerations to maintain porosity and reactivity compared to lime or sodium hydroxide(Skousen et al., 2017). Despite these challenges, the effective treatment of severe AMD with limestone-based technologies has been demonstrated in both large and small scale systems(Caraballo, Rötting, Macías, Nieto, & Ayora, 2009; Hedin et al., 2010) that can serve as models to leverage the high

REE concentrating efficiency, low cost, and sustainability of limestone to provide the best technology for recovering REE from AMD.

3.4 Conclusions

REE appear to be the most promising clean energy critical metal to recover from waste AMD treatment solids. Recovering REE from these solids offers a more sustainable source of REE compared to many traditional and non-traditional sources by (1) eliminating mining impacts, (2) generating lower U and Th content, and (3) reduced use of chemicals needed for processing. Total REE concentrations in solids currently produced from AMD treatment systems across Appalachia can contain over 2,000 mg/kg dry weight and the variability in REE in AMD treatment solids can be explained by AMD pH and the neutralization technology used in the remediation system. The highest total REE concentrations are associated with solids containing high Al and Mn concentrations. Geochemical relationships indicate that REE recovery will be maximized in systems that treat low pH (<5) and high Al and/or Mn- containing AMD, using methods such as limestone treatment that can minimize nontarget solids precipitation.

For future systems designed to treat AMD and concentrate REE into solids, the use of limestone as an acid neutralization agent should be considered because it is significantly less costly than lime or sodium hydroxide, has a lower environmental footprint, and produces solids with high REE concentrations. The value of REE in treatment solids, up to $405 USD/metric ton of dry material, could offset the treatment costs of AMD that pollutes many surface waters worldwide. The framework developed here can help in the identification of promising REE and critical metal sources, evaluation of the economics of REE capture, and in engineering treatment systems to

maximize REE recovery in solids, thus transforming an economic and environmental liability into a valuable resource.

3.5 Acknowledgements

This research was supported by a University of Pittsburgh Mellon Predoctoral Fellowship (BCH), and a University of Pittsburgh Central Research Development grant (RCC), with technical support and data from Hedin Environmental. We appreciate the help with statistical analysis from Dr. Eitan Shelef at the University of Pittsburgh.

This chapter was published in the International Journal of Coal Geology, 231, Benjamin C. Hedin, Robert S. Hedin, Rosemary C. Capo, and Brian W. Stewart, Critical metal recovery potential of Appalachian acid mine drainage treatment solids, Copyright Elsevier, 2020.

4.0 Determination and prediction of micro scale rare earth element geochemical relationships in mine drainage treatment wastes

4.1 Introduction

The demand for rare earth elements (REE), defined here as the 15 lanthanide elements plus yttrium (DOE, 2011) is expected to increase sharply in the coming decades due to their use in renewable energy technologies (e.g., wind turbines, electric motors, and batteries) and because of their limited natural sources (Fishman & Graedel, 2019). The mining and refining of REE from ore commonly results in the production of hazardous waste, and currently is largely limited to southeastern Asia (Law, 2019) The need for more geographically diverse and environmentally friendly REE sources has spurred research into non-traditional feedstocks (Binnemans et al., 2013; Hein et al., 2013; Lin et al., 2018; Stuckman et al., 2018; Takaya et al., 2018), including from acid mine drainage (AMD)(Ayora et al., 2016; Hedin et al., 2019a; Lefticariu et al., 2019; Moraes et al., 2020; Stewart et al., 2017; Vass et al., 2019b).

The oxidation and dissolution of sulfide minerals (e.g., pyrite, FeS_2) related to coal and metal mining produces acidity and dissolved metals that pollute waterways around the world with AMD (Younger et al., 2002). However, this acidity can also interact with surrounding rocks to leach REE from host minerals (Wallrich et al., 2020), resulting in dissolved concentrations many orders of magnitude higher than unpolluted groundwater (Cravotta, 2008a; Noack et al., 2014; Stewart et al., 2017). Single AMD discharges can produce up to 7,000 kg dissolved REE/year with many discharges in the Appalachian Basin, eastern USA, and the Iberian Pyrite Belt, Spain, potentially producing >100 kg REE/year (Ayora et al., 2016; Cravotta, 2008a; Hedin et al., 2019a;

Stewart et al., 2017). AMD from the Appalachian basin alone generates between 500 and 3,400 metric tons of REE annually, depending on estimates of the AMD flux and REE concentration (Stewart et al., 2017; Vass et al., 2019a). This represents 7% to 41% of the annual US consumption of REE in 2018 (Gambogi, 2019a, 2019b).

Regardless of where AMD discharges occur, remediation involves pH and/or redox adjustments to neutralize acidity and accelerate the precipitation and settling of dissolved metals (Younger et al., 2002). This generates significant amounts of solid waste which incur considerable costs to treatment system operators (Cravotta et al., 2014). Dissolved REE are preferentially partitioned into these precipitates, and with reported REE concentrations as high as 2,000 mg/kg, they are potential targets for REE recovery that could offset the cost of treating AMD (Hedin, Hedin, Capo, & Stewart, 2020a; Vass et al., 2019b).

AMD solids are primarily composed of amorphous and poorly crystalline Fe-, Al-, and Mn-rich sulfate/oxide/hydroxide phases (Bigham & Nordstrom, 2000; Kairies et al., 2005; Pu et al., 2010; Tan et al., 2010). Many of these phases co-precipitate or sorb REE and thus are potentially REE-enriched (Ayora et al., 2016; Hedin et al., 2019a; Hedin et al., 2020a; Lozano et al., 2019b; Moraes et al., 2020; Verplanck et al., 2004). Lozano et al., (2019b) found that in Al rich AMD solids, REE are removed by inner-sphere complexation with Al minerals. Although similar work has not been carried out for Fe- and Mn-rich AMD solids, in marine Fe-Mn nodules REE are also removed by surface sorption (Bau & Koschinsky, 2009). Additionally, experimentals on the pH dependent surface complexation of dissolved REE in sulfate-rich waters by basaluminite ($Al_4SO_4(OH)_{10}\cdot 5H_2O$) and schwertmannite ($Fe_8O_8(OH)_6SO_4$) have been carried out and developed into geochemical models (Lozano et al., 2019a, 2020). Similar models could be developed for Fe hydroxides and Mn oxides from existing data compilations (Dzombak & Morel, 1990; Karamalidis

& Dzombak, 2010; Pourret & Davranche, 2013; Tonkin, Balistrieri, & Murray, 2004). Developing a model that integrates REE sorption on Al, Fe, and Mn oxide/hydroxides is critical for AMD treatment systems where all three mineral phases can be present.

Despite the work to date, the REE-hosting mineral phases in geochemically complex AMD solids (e.g., those with Fe, Al, and Mn minerals) is poorly understood, and the mechanism of dissolved REE attenuation (e.g., mineral precipitation, solid solutions, and/or surface complexation on Fe, Al, and/or Mn minerals) in AMD systems has not been identified. There is a need to develop models that will predict both dissolved REE removal from treatment systems, and REE accumulation with specific minerals in AMD solids. This is significant because in the Appalachian basin, AMD solids with the highest REE concentrations typically also have high concentrations of Fe, Al, and Mn (Hedin et al., 2020a).

In this study, we use chemical sequential extractions, synchrotron x-ray absorption near edge spectroscopy (XANES), and synchrotron x-ray florescence (XRF) to identify minerals in AMD solids that are enriched in REE. We then use existing thermodynamic data to construct geochemical models to predict dissolved REE mobility in AMD treatment systems, identify the mechanisms of removal, and to assess which minerals are enriched in REE. These results can be used to predict REE mobility in AMD treatment systems and aid in the development of novel extractions that specifically target the REE-enriched phases or the development of treatment processes that concentrate REE with specific phases.

4.2 Materials and methods

4.2.1 Chemical data

Chemical data from AMD solids and influent and effluent water samples from the Scootac and Woodlands AMD remediation systems and solids from the Westbox system (described in Hedin et al., 2019) are presented in Tables 7 and 8. Solids were used for phase characterization and water data were used to calibrate the models. At the Scootac passive remediation site, Scootac-Al refers to Al-rich solids flushed from the limestone bed and Scootac-Mn refers to Mn-rich solids armored on the limestone aggregate. The Woodlands sample are Al-rich solids flushed from a limestone system. Solids from the Westbox site are Fe-, Al-, and Mn-rich solids that precipitate in a non-flushing limestone bed.

Influent and effluent water samples from the Westbox limestone treatment system were filtered to <0.45 μm and aliquots acidified to 2% nitric acid (HNO_3^-). Cations were determined on aliquots acidified to 2% ultrapure HNO_3^- by inductively coupled plasma (ICP) optical emission spectroscopy (OES) and ICP-mass spectroscopy (MS) and anions were determined by ion chromatography (IC) at Activation Laboratories, Ontario, Canada. Cation-anion imbalances are <±4% of total charge. AMD solid samples Woodlands, Scootac-Al, Scootac-Mn, and Westbox were also analyzed for bulk chemistry at NETL's Pittsburgh Analytical Laboratory (PAL) using $LiBO_2$ fusion followed by ICP-MS/OES analysis for major and trace elements. Cobalt concentrations are reported in Table 7.

Field data collected included flow rate, pH, temperature, conductivity, and alkalinity measured by titration. CO_2 concentrations were measured by Carbo-Q (Vesper & Edenborn, 2012).

4.2.2 Sequential extractions

Sequential extractions were performed on Scootac-Al, Scootac-Mn, and Westbox solids to identify solid phases containing REE. They were conducted on Scootac-Al and Scootac-Mn solids in duplicate and on Westbox in triplicate. Initial samples were dried at 95° C and ground to <100 mesh. Sequential extractions were conducted in acid washed plastic centrifuge tubes and all syringes and filters used in the sequential extractions were acid washed.

Seven step sequential extractions (Lin et al., 2018) targeted: (1) water soluble phases using MilliQ water (18.2 mΩ/cm) at 20:1 liquid to solid (L:S) ratio (mL to g), 25°C, and 24 hour reaction time; (2) the exchangeable fraction using 1.0 M ammonium chloride at 20:1 L:S ratio, 25°C, and 24 hour reaction time; (3) carbonates using 1.0 M ammonium acetate at 25:1 L:S ratio, 25°C, and 24 hour reaction time; (4) amorphous Mn oxides using 0.1 M hydroxylamine hydrochloric at 20:1 L:S ratio, 25°C, and 0.5 hour reaction time; (5) amorphous Fe oxides using 0.2 M ammonium oxalate and 0.2 M oxalic acid at 20:1 L:S ratio, 25°C, and 4 hour reaction time in the dark; (6) crystalline Fe oxides using 0.2 M ammonium oxalate, 0.2 M oxalic acid, and 0.1 M ascorbic acid at 20:1 L:S ratio, 80°C, and 0.5 hour reaction time; (7) organics and sulfides using two doses of 30% hydrogen peroxide acidified to pH 2 by nitric acid at 10:1 L:S ratio, 85°C, and 1 hour reaction time followed by 1.0 M ammonium acetate at 50:1 L:S ratio, 25°C, and 16 hour reaction time. Finally, solid residues were analyzed at NETL PAL using $LiBO_2$ fusion followed by ICP-MS/OES analysis for major and trace elements.

After each step, solids and liquids were separated by centrifuging at a force of 3,000 times gravity (× g) for 20 minutes. The leachate was filtered to <0.45 μm, pH recorded, and an aliquot sent to NETL PAL for ICP-MS/OES analysis. Solids were then washed with 20 mL MilliQ water, mixed for 20 minutes, and centrifuged for 20 minutes. The supernatant was discarded, and the

solids were dried overnight at 60° C and the dried weight recorded. Final reported elemental extractions were adjusted based on the percent weight lost in each step, and percentage of REE extracted was calculated from the bulk geochemistry of each initial sample measured at NETL PAL. Detection limits at PAL ranged from 0.004 μg/L to 0.031 μg/L for REE, from 0.57 μg/L to 1.12 μg/L for Sc, and was 1.29 μg/L for Co.

4.2.3 Bulk Ce and Mn x-ray absorption near edge spectroscopy (XANES)

Ce oxidation states were measured using bulk Ce XANES conducted at the Stanford Synchrotron Radiation Lightsource (SSRL) on four AMD samples (Woodlands, Scootac-Al, Scootac-Mn, and Westbox), three synthetic Mn, Al, and Fe oxides/hydroxides, and Ce standards. ACS grade boehmite AlO(OH) was used as a synthetic Al mineral.

Na-birnessite ($(Na)Mn_7O_{14}\cdot 2.8H_2O$), a major mineral in Mn-rich AMD solids (Tan et al., 2010), was synthesized following methods of Golden et al., 1987 (Golden, Chen, & Dixon, 1987). Briefly, air was bubbled through a 200 mL solution of 0.5 M $MnCl_2$ while a refrigerated 250 mL, 5.5 M NaOH solution (55 g NaOH total) was quickly added. The solution was aerated at the highest flow rate possible and mixed with a magnetic stir bar at the maximum velocity possible (Feng, Liu, Tan, & Liu, 2004) for 5 hours. The solution was centrifuged and the precipitates were rinsed with MilliQ water until the supernatant was less than pH 7.5. Precipitates were then dried at 60°C.

Ferrihydrite ($Fe(OH)_3$), a major Fe mineral in AMD solids (Kairies et al., 2005), was synthesized according to the methods of Cornell and Schwertmann (Cornell & Schwertmann, 2003). Briefly, 500 mL of $FeCl_3$ (0.1 M Fe) was rapidly titrated to pH 7.5 in less than 5 minutes using 1.0 M NaOH. The last 20 mL was added drop-wise while the pH was monitored. The

resulting mixture was centrifuged at 8,000 g for 20 minutes and dialyzed until free of electrolytes and unreacted ions.

A 1.0 M Ce solution was prepared by dissolving $CeCl_3$ (ACS grade, Sigma Aldrich, Inc.) into 10 mL of MilliQ water and reacted with 1 g of the synthetic Mn, Al, and Fe oxides/hydroxides described above for approximately 15 hours to allow for Ce sorption. The solutions were centrifuged, liquid and solid fractions separated, and solids dried at 95° C. Aliquots of the initial solution and the final liquid fractions were analyzed at NETL PAL by ICP-MS analysis for Ce concentrations. These four AMD solids, three synthetic minerals, and seven Ce standards ($Ce(IV)(SO_4)_2$, $Ce(IV)O_2$, $Ce(III)_2(CO_3)_3$, $Ce(III)_2(SO_4)_3$, $Ce(III)NO_3$, $Ce(III)Cl_3$, and $Ce(III)PO_4$; ACS grade Sigma Aldrich, Inc.) were then ground to <100 mesh and spread on clear tape for bulk Ce XANES analyses.

Bulk Ce-XANES data were collected on the Ce L_{III} edge (5,732 eV) at SSRL beamline 3-4 following the methods of Stuckman et al. (Stuckman et al., 2018). Twelve to 20 scans were collected for each AMD solids and two scans for each synthetic mineral and Ce standard. Scans were energy aligned and merged into one average scan and normalized using ATHENA software (Ravel & Newville, 2005). The contribution of Ce(III) and Ce(IV) in the synthetic minerals and the AMD solids were quantified using ATHENA's linear combination fitting (LCF) using different combinations of Ce(III) and Ce(IV) standards as endmembers.

Bulk Mn XANES were collected on the Mn K edge (6539 eV) for the AMD solids and Mn oxide standards ($Mn(II)O$, $Mn(III)_2O_3$, and $Mn(IV)O_2$; ACS grade Sigma Aldrich, Inc.). AMD sample spectra show evidence of beam damage (oxidation/reduction of Mn during measurements) and were not usable. Manganese standard spectra were not damaged and were used for LCF fitting of Mn μ-XANES described below.

4.2.4 Micro x-ray fluorescence (μ-XRF) and μ-XANES

μ-XRF mapping was conducted on Woodlands, Scootac-Al, Scootac-Mn, and Westbox samples to determine the spatial co-associations of REE and major elements. 30 μm thick, doubly polished microprobe-prepped thin sections (Spectrum Petrographics, Inc.) were prepared. μ-XRF mapping was conducted at SSRL beamline 2-3 which was equipped with a 4 μm beam size, Si(1,1,1) crystal, and a single element Si Vortex detector. Energy ranged from 1,000 eV to 10,000 eV with a 5 μm step size and 100 ms dwell time. Maps were processed in SIXpack software (Webb, 2005) using PYMCA fitting to deconvolute spectral interferences (Stuckman et al., 2018).

During μ-XRF mapping, μ-XANES were periodically collected on beamline 2-3 at SSRL to determine the oxidation state of Ce and Mn at micro scale resolution. Cerium and Mn μ-XANES were collected on the Ce L_{III} and the Mn K edges, respectively, with 4 μm beam size. Multiple μ-XANES scans were collected and they were processed following the same methods as bulk XANES. CeO_2 and MnO_2 standards were measured on beamline 2-3 to calibrate the Ce and Mn standards measured on beamline 4-3 for beamline 2-3 μ-XANES LCF of both Ce and Mn. Manganese oxidation states were computed from μ-XANES spectra using ATHENA's LCF with Mn(II)O, $Mn(III)_2O_3$, and $Mn(IV)O_2$ as endmembers per Manceau et al., 2012 (Manceau, Marcus, & Grangeon, 2012).

4.2.5 Geochemical models

Geochemical models were constructed in PHREEQC (Parkhurst & Appelo, 2013) for the three treatment systems to test predictions of REE removal and mineral associations from published thermodynamic data. PHREEQ n AMDTreat models (Cravotta, 2020) were expanded

to include REE. The default PHREEQC database was supplemented with HFO (hydrous ferric oxide), HMO (hydrous manganese oxide), and HAO (hydrous aluminum oxide) cation and anion surface complexation thermodynamic data from Cravotta, 2020 (see Table S4 in Cravotta, 2020), REE aqueous speciation thermodynamic data (Table S4), REE mineral thermodynamic data (Table S5), REE surface complexation thermodynamic data (Table S6), and HFO, HMO, and HAO surface properties (Table S7).

REE aqueous speciation log k data from Liu et al., 2017 were supplemented with Y and Sc data from Thermo Minteq (https://www.gwb.com/thermo.php). $REE(SO_4)_2^-$ data were added from an updated Lawrence Livermore National Laboratory (LLNL) database (Ram, Vaughan, Etschmann, & Brugger, 2019). REE mineral thermodynamic data were obtained from an updated LLNL database (Ram et al., 2019) supplemented with thermodynamic data from Wagman et al. (Wagman, Evans, Parker, Schumm, & Halow, 1982) and Spahiu and Bruno (Spahiu & Bruno, 1995).

For the surface complexation model, sorption of REE, Ca, Mg, Al, Fe(II), and Mn(II) on HFO, HMO, and HAO was considered. For HFO and HAO lacking empirically derived REE surface complexation thermodynamic data, the linear free energy relationship (LFER; the relationship between the first hydrolysis constant and surface complexation constant), was used to calculate REE surface complexation constants per the methods of Liu et al. (Liu et al., 2017). HFO was modeled using the monoprotic, diffuse double layer (MDDL) model of Dzombak and Morel (Dzombak & Morel, 1990) with $Fe(OH)_3$ stoichiometry, two exchange sites (HFO_w and HFO_s) with REE^{+3} cations, and REE surface complexation constants calculated from REE and Y LFER. HMO was modeled using the MDDL model of Pourret and Davranche (Pourret & Davranche, 2013) with MnO_2 stoichiometry, two exchange sites (HMO_x and HMO_y) with REE^{+3} cations,

and surface complexation constants from Pourret and Davranche, 2013. HAO was modeled using data from two sources: 1) Karamalidis and Dzombak (Karamalidis & Dzombak, 2010) with $Al(OH)_3$ stoichiometry, a single exchange site with REE^{+3} cations, and surface complexation constants calculated from LFER, and 2) Lozano et al. (Lozano et al., 2019a) with a single exchange site with $REESO_4^+$ complexes and surface complexation constants calculated from their experiments. Surface areas and exchange site densities for HFO, HMO, and HAO were obtained from Dzombak and Morel (1990), Tonkin et al. (2004), and Karamalidis and Dzombak, (2010), respectively.

The PHREEQC model operated by reacting AMD with a base (e.g. $CaCO_3$, NaOH) to a set pH at which point the system was equilibrated with respect to aqueous speciation, sorption on HFO, HAO, and HMO, and precipitation of mineral phases or solid solutions. The process was then repeated using the same untreated AMD chemistry titrated to a different pH. In this manner, the pH dependency of the distribution of REE between the dissolved, sorbed, and mineral phases could be evaluated. The PHREEQC model was calibrated using a NaOH titration of the Nittanny Mine influent from Cravotta and Brady (Cravotta & Brady, 2015).

4.3 Results

4.3.1 Field samples

Chemistry for the water and solid samples used in this study are presented in tables 7 and 8. All three treatment systems removed over 97% of dissolved REE entering the systems and all produced solids with over 1,100 mg/kg REE.

Table 7 Major element and REE chemistry for the solids used in this study. Data are from Hedin et al., 2019 except for Co concentrations for Scootac-Mn and Westbox which were measured at NETL PAL.

	Al	Fe	Mn	Si	Ca	C	LOI	Sc	Y	La	Ce	Pr	Nd	Sm	Eu	Gd	Tb	Dy	Ho	Er	Tm	Yb	Lu	Sum REE	Co	Ni	Zn	Cu
				%															ppm									
Woodlands	19	2	0.1	14	1	3	24	31	206	87	288	47	222	66	16	70	9	47	8	19	2	14	2	1,103	18	54	339	112
Scootac-Al	25	1	1.2	4	1	2	35	25	599	113	291	55	262	86	23	123	20	118	22	62	9	57	9	1,849	351	681	4,450	112
Scootac-Mn	4	1	14.8	5	18	5	27	5	396	143	274	42	181	45	12	63	11	62	13	33	4	23	3	1,303	6,026	6,720	9,860	103
Westbox	16	5	9.1	7	2	1	28	49	383	183	597	69	305	88	21	98	15	86	16	44	6	36	5	1,952	2,059	3,850	6,880	590

Table 8 Chemistry for the water samples used in this study. Data for Scootac and Woodlands are from Hedin et al., 2019. Data from Westbox are from this study.

Location	pH	Conductivity	Dissolved oxygen[1]	Field Alkalinity[2]	CO_2[3]	Ca	Mg	Na	Fe	Al	Mn	K	Si	Cl	SO4
		uS/cm						mg/L							
Scootac In	3.91	1146	3.90	0	127.3	90.5	98.5	2.8	*0.0*	7.4	16.1	4.4	10.4	0.9	701.1
Scootac Out	6.98	1326	3.16	172	49.3	193.0	99.6	2.8	*<0.04*	0.0	0.3	4.4	9.1	1.3	712.9
Woodlands In	3.27	1111	4.65	0	143.7	105.5	44.6	11.7	0.7	19.7	0.8	0.8	16.9	4.9	608.0
Woodlands Out	6.62	1232	4.23	225	92.3	252.0	47.2	11.7	*<0.04*	0.1	0.1	1.0	12.2	5.6	559.5
Westbox In	2.95	920	10.07	0	16.7	44.3	27.7	1.2	2.8	12.2	6.6	2.3	15.3	0.6	388.0
Westbox Out	7.30	852	12.50	132	5.0	147.5	30.2	1.3	0.0	0.0	0.0	2.0	8.8	0.5	376.0

Location	Y	La	Ce	Pr	Nd	Sm	Eu	Gd	Tb	Dy	Ho	Er	Tm	Yb	Lu
						ug/L									
Scootac In	44.48	14.19	32.52	4.60	20.94	5.45	1.42	8.28	1.49	7.44	1.55	4.22	0.54	3.08	0.44
Scootac Out	1.71	0.63	0.05	0.07	0.32	0.06	0.01	0.11	0.02	0.10	0.02	0.06	0.00	0.03	<0.004
Woodlands In	31.58	13.96	51.39	7.84	37.53	10.28	2.41	11.09	1.68	7.10	1.23	2.90	0.35	1.87	0.26
Woodlands Out	1.37	0.93	1.05	0.22	0.91	0.16	0.04	0.21	0.03	0.13	0.03	0.06	0.01	0.04	<0.003
Westbox In	30.80	14.95	39.37	5.24	23.87	6.51	1.55	7.55	1.22	6.36	1.22	3.28	0.43	2.59	0.37
Westbox Out	0.73	0.39	0.10	0.07	0.33	0.06	0.01	0.09	0.01	0.07	0.01	0.03	0.00	0.02	0.00

[1]Dissolved oxygen is is mg/L O_2. [2]Field alkalinity is in mg/L as $CaCO_3$. [3]CO_2 is measured by Carbo-Q methods.

4.3.2 Sequential extraction leachates

The elemental sequential extraction data are shown in Figure 14. The total REE extracted (7 steps + residual) ranged from 74% to 105% of the REE concentrations measured in the solid material. The cumulative extraction of Sc and Co, which are additional valuable metals that could be recovered from AMD solids, ranged from 84% to 107% and from 74% to 90%, respectively. Co is also presented because can be incorporated into the crystal structure of Fe and Mn oxides and hydroxides (Burns, 1976; Manceau et al., 2000) and thus could be used as a comparison to indicate whether REE are similarly structurally substituted.

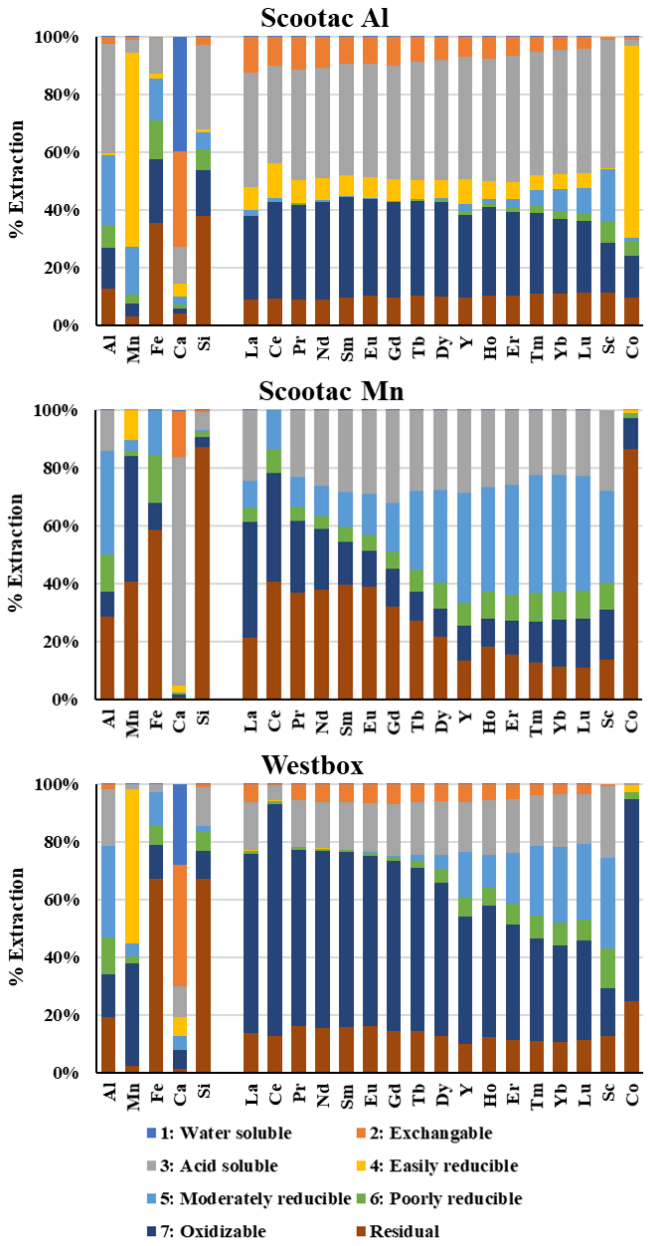

Figure 14 Percent major elements, REE, Sc, and Co extracted at each sequential extraction step normalized to 100%.

For the Scootac-Al solids, the acid soluble (extractions 3) and oxidizable (extraction 7) fractions contained the most REE, yielding 35% and 27% of TREE, respectively. For the Westbox solids, the oxidizable fraction (extraction 7) contained the most REE, but the yield varied from

between 29% for Lu to 53% for La. For the Scootac-Mn solids, the acid soluble (extraction 3) and oxidizable (extraction 7) fractions contained the most light REE (LREE; La to Gd) and the moderately reducible fraction (extraction 5) contained the most heavy REE (HREE; Tb to Lu, including Y).

There was little preferential partitioning of individual REE in different fractions in the Scootac-Al solids. For Scootac-Mn and Westbox, the moderately reducible (extraction 5) preferentially contained HREE. Additionally, Scootac-Mn and Westbox have anomalously low Ce extraction (< 2%) in steps 1 and 2. These anomalies are largely absent in the Scootac-Al extractions.

The fractions that contained the most Sc were the water soluble fraction (extraction 3) for the Scootac-Al solids, and the moderately reducible fraction (extraction 5) for the Scootac-Mn and Westbox solids. The fractions that contained the most Co was the easily reducible (extraction 4) for the Scootac-Al solids and the oxidizable fraction (extraction 7) for the Westbox solids. For the Scootac-Mn solids, 89% of Co remained in the residue. For Woodlands, approximately 60% of Co and Mn and less than 10% of REE were contained in the easily reducible fraction (extraction 4), consistent with the close association between Mn and Co and the different removal mechanisms of REE and Co from AMD.

4.3.3 Synchrotron bulk Ce XANES

While XANES patterns are influenced by structural symmetry and bonding, spectra for all Ce(III) standards were similar and spectra for all Ce(IV) standards were similar (Figure S9), in agreement with previous work (Stuckman et al., 2018; Takahashi, Sakami, & Nomura, 2002). All Ce(III) standards show a single peak at ~5,728 eV and all Ce(IV) standards two peaks at ~5,732

eV and ~5,740 eV. Bulk Ce XANES spectra for Ce(III) and Ce(IV) sulfate standards, synthetic minerals, and AMD solids are shown in Figure 15.

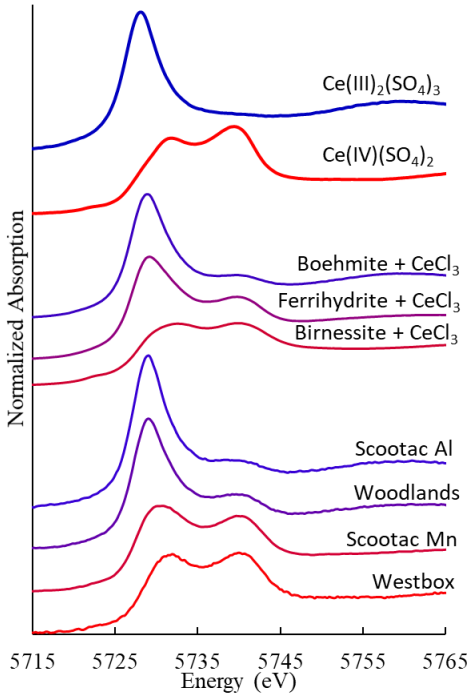

Figure 15 Bulk Ce XANES for pure Ce minerals, synthetic mineral + Ce(III) experiment, and AMD solids. Colors indicate oxidation state with blue and red as Ce(III) and Ce(IV), respectively, and purple as a mix of two oxidation states.

Linear combination fitting (LCF) resulted in similar Ce(III) and Ce(IV) fractions for each sample regardless of which combinations of standards were used (Table S8). The maximum ranges in Ce(III) and Ce(IV) fractions for one sample were 0.22 and 0.12, respectively. Average deviations for Ce(III) and Ce(IV) fractions were 0.16 and 0.09, respectively.

Bulk Ce XANES on boehmite, ferrihydrite, and birnessite show average Ce(III) and Ce(IV) percentages of 74% Ce(III) and 26% Ce(IV), 46% Ce(III) and 54% Ce(IV), and 0% Ce(III) and 100% Ce(IV), respectively (Table 9). Bulk Ce XANES on Scootac-Al, Woodlands, Scootac-Mn,

and Westbox show average Ce(III) and Ce(IV) percentages of 69% Ce(III) and 31% Ce(IV), 54% Ce(III) and 46% Ce(IV), 20% Ce(III) and 80% Ce(IV), and 2% Ce(III) and 98% Ce(IV), respectively (Table 9).

Table 9 Linear combination fitting of bulk Ce XANES using Ce(III) and Ce(IV) standards as endmembers. Parentheses indicate software generated uncertainties. The combination of standards with the best fit (lowest R value from table S8) is shown below.

Sample	Ce(III) weight	Ce(IV) weight	Sum
Birnessite + $CeCl_3$	0.000 (0.006)	0.883 (0.007)	0.88
Ferrihydrite + $CeCl_3$	0.512 (0.008)	0.598 (0.008)	1.11
Boehmite + $CeCl_3$	0.780 (0.011)	0.270 (0.011)	1.05
Scootac-Al	0.692 (0.014)	0.308 (0.017)	1.00
Woodlands	0.541 (0.011)	0.463 (0.013)	1.00
Scootac-Mn	0.209 (0.008)	0.830 (0.008)	1.04
Westbox	0.019 (0.007)	0.979 (0.007)	1.00

4.3.4 Synchrotron μ-XRF and μ-XANES

Select μ-XRF maps are shown in Figure 16 and Figure 17 and the remaining μ-XRF maps can be found in supplemental information. Cerium and Mn μ-XANES locations and spectra are shown in supplemental Figures S10 to S17 and summarized in Tables S9 and S10.

For Scootac-Mn, Hedin et al. (Hedin et al., 2019a) used μ-XRF to show that REE accumulate in the ~200μm wide Mn crust precipitated on the surface of limestone aggregate. Cobalt and Ni also accumulate in this Mn crust (Figure S10). Cerium and Mn μ-XANES in the

Mn crust show average Ce(III) and Ce(IV) percentages of 7% Ce(III) (± 4% (one standard deviation)) and 93% Ce(IV) (± 4%) and an average Mn oxidation state of 3.99 (± 0.01) (Figure S11; Table S9; Table S10).

Two Westbox μ-XRF maps (area 2 small and area 3 small), show distinct Mn-, Fe-, and Al-rich zones (Figure 16; Figure S12) with Co, Ni, Cu, Zn, and REE co-associating with Mn and Fe in both maps. Quantitative associations were assessed by computing correlation coefficients between major metal (Mn, Fe, Al) and trace metal (Co, Ni, Cu, Zn, individual REE) detection counts (higher counts = higher concentrations) for all pixels in single maps. In both Westbox maps, Co, Ni, and Cu are associated with Mn ($r = 0.75$ to 0.92) and in one map, Zn is associated with Mn ($r = 0.73$) (Table 3). Correlation coefficients are <0.56 between these trace metals and Fe and Al.

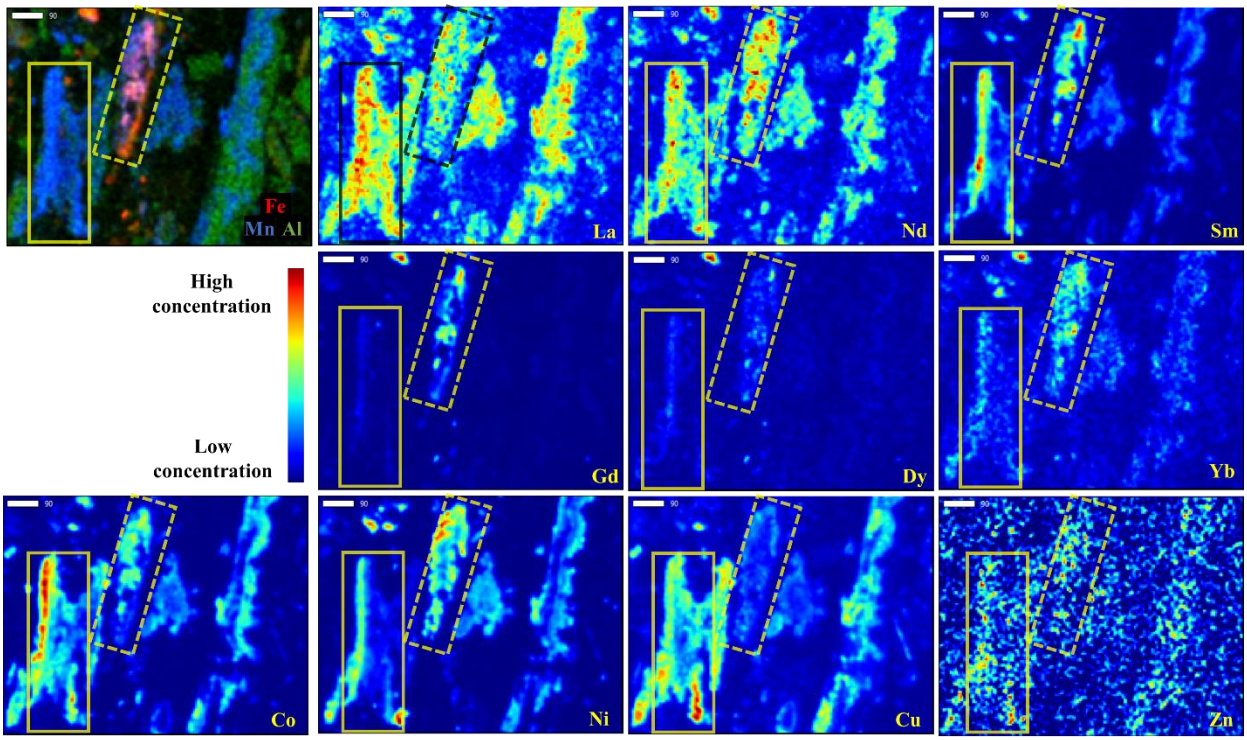

Figure 16 Westbox area 2 small µ-XRF maps. The same area is shows in all maps with a Mn rich area in the solid box and a Fe rich area in the dashed box. In the upper left box, Fe is in red, Mn in blue, and Al in green with brighter intensities relating to higher concentrations. For all other maps, red to blue shows high to low concentrations. Scalebars in the upper left of all maps are 90 µm.

Table 10 Correlation coefficients (r) between counts of major elements (Mn, Fe, Al) and trace metals for u-XRF maps. Correlations are calculated from the total detection counts of each element (after PyMCA fitting) for all pixels in the map. Blank cells mean no data because that element was not included in the PyMCA fitting. The darker the cell color, the better the correlation.

Map		La	Ce	Nd	Sm	Eu	Tb	Gd	Dy	Y	Yb	Lu	Sum REE	Co	Ni	Cu	Zn
Westbox Area 2 small	Mn	0.73	0.34	0.72	0.89			0.27	0.32		0.52		0.65	0.92	0.83	0.83	0.20
Westbox Area 2 small	Fe	0.14	0.11	0.35	0.35			0.89	0.63		0.40		0.74	0.23	0.22	0.01	0.02
Westbox Area 2 small	Al	0.40	0.22	0.38	0.37			0.24	0.22		0.29		0.37	0.41	0.35	0.43	0.09
Westbox Area 3 small	Mn	0.43	0.76	0.95	0.57			0.57	0.45		0.59		0.88	0.91	0.75	0.84	0.73
Westbox Area 3 small	Fe	0.10	0.21	0.22	0.19			0.64	0.41		0.29		0.36	0.23	0.30	0.02	0.16
Westbox Area 3 small	Al	0.32	0.45	0.48	0.30			0.34	0.24		0.31		0.47	0.47	0.36	0.56	0.44
Scootac Al A1sm	Mn	0.25	0.40	0.51	0.92	0.66	0.15	0.64			0.83		0.75	0.81	0.72	0.26	0.90
Scootac Al A1sm	Fe	0.11	0.15	0.12	0.05	0.41	0.89	0.62			0.07		0.54	0.05	0.16	0.21	0.19
Scootac Al A1sm	Al	0.26	0.30	0.22	0.13	0.14	0.09	0.14			0.14		0.16	0.16	0.23	0.35	0.33
Woodlands reg2	Mn	0.23	0.05	0.17	0.90	0.14		0.07	0.05	0.05	0.13	0.08	0.17	0.02	0.31	0.64	0.86
Woodlands reg2	Fe	0.28	0.26	0.28	0.22	0.80		0.91	0.81	0.26	0.47	0.69	0.87	0.90	0.68	0.21	0.29
Woodlands reg2	Al	0.14	0.13	0.16	0.12	0.23		0.24	0.21	0.13	0.20	0.21	0.25	0.24	0.22	0.19	0.15

For LREE, correlation coefficients with Mn range from 0.34 to 0.95 and are less than 0.48 with Fe or Al (Table 3). For MREE and HREE, there are correlation coefficients greater than 0.60 with both Mn and Fe. Westbox Ce and Mn μ-XANES show average Ce(III) and Ce(IV) percentages of 23% Ce(III) (±9%) and 77% Ce(IV) (±9%) and an average Mn oxidation state of 3.74 (no standard deviation, only 2 measurements; Figure S13; Table S9; Table S10).

Scootac Al μ-XRF maps show large Al-rich areas with small (<50 μm) hotspots of Fe and Mn co-associated with Co, Ni, Zn, and REE (Figure 17). Cobalt, Ni, and Zn are associated with Mn (r >0.72; Table 3). For REE, Tb is associated with Fe (r = 0.89), Gd is associated with both Fe and Mn (r = 0.64 and 0.62, respectively), and all other REE are co-associated with Mn (r >0.40). However, La, Ce, and Nd, all present in high concentrations (> 250 ppm), are also widely

distributed throughout the Al rich matrix. Cerium μ-XANES show average Ce(III) and Ce(IV) percentages of 89% Ce(III) (±4%) and 11% Ce(IV) (±4%) (Figure S14; Table S10). No Mn μ-XANES were collected.

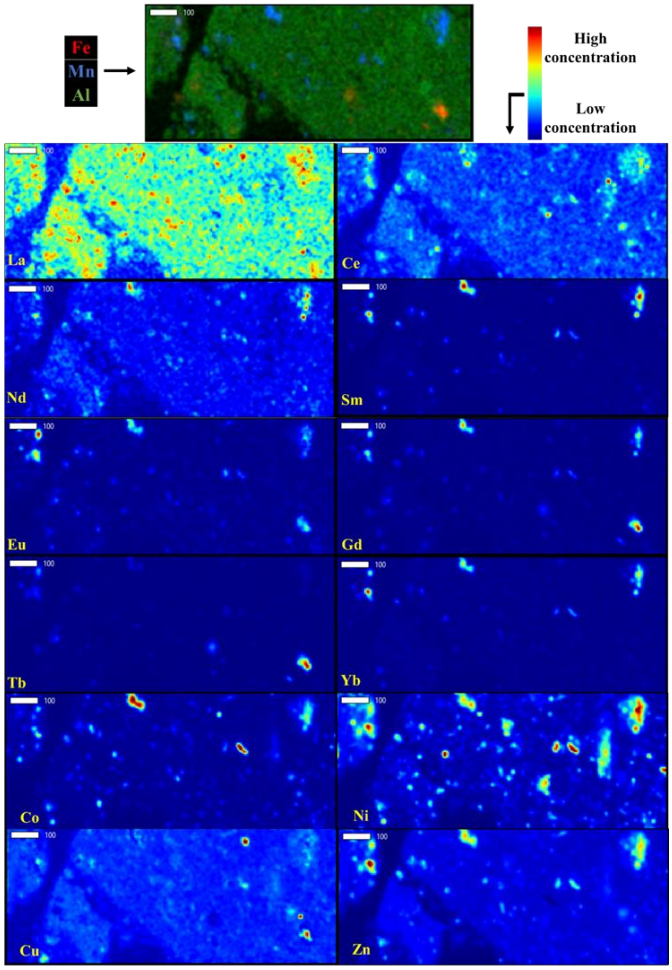

Figure 17 Scootac Al A1sm μ-XRF maps. In the upper box, Fe is in red, Mn in blue, and Al in green with brighter intensities relating to higher concentrations. For all other maps, red to blue shows high to low concentrations. Scalebars in the upper left of all maps are 100 μm.

Two Woodlands μ-XRF maps, (1fA and reg2), also show large Al rich areas with small (< 50 μm) hotspots of Fe and Mn co-associated with Co, Ni, Cu, Zn, and REE (Figure S15; Figure

S16). The REE hotspot in the center of image 1fA is an artifact, as shown by Ce μ-XANES spectra (Figure S17). This artifact prevents accurate correlation coefficients from being calculated. Woodlands 1fA Ce μ-XANES show average Ce(III) and Ce(IV) percentages of 80% Ce(III) (±8%) and 20% Ce(IV) (±8%) (Figure S17; Table S10). No Mn μ-XANES were collected.

For Woodlands reg2, LREE appear widely distributed throughout the Al rich matrix. Co and Ni are associated with Fe ($r > 0.68$) and Cu and Zn are associated with Mn ($r > 0.64$). Yttrium, La, Ce, and Nd are poorly correlated with Fe, Mn, or Al ($r < 0.28$). Sm is associated with Mn ($r = 0.90$) and Eu, Gd, Dy, Yb, and Lu are associated with Fe ($r > 0.47$). REE with high concentrations, La, Ce, and Nd, are also distributed throughout the Al matrix (Table 3). No μ-XANES were collected.

4.3.5 Geochemical models

4.3.5.1 Model validation and calibration

The accuracy of the REE geochemical model developed here needed to be assessed by comparing modeled data to empirical data. A field NaOH titration of the Nittanny mine influent carried out by Cravotta and Brady (Cravotta & Brady, 2015) was used for this assessment. This titration demonstrated that as pH increased from 3.0 to 10.0, dissolved Fe, Al, Mn, and REE concentrations decreased (Figure 18). The observed concentrations for Al and Fe (predominantly Fe^{+3}), reached minimum values during the first titration step to pH 6.0. Substantial removal of REE was observed at pH 6.0 with complete removal at higher pH. Additionally, REE with smaller atomic radii (HREE; e.g. Lu) are preferentially removed compared to REE with larger atomic radii (LREE; e.g. La); a phenomenon commonly observed in surface complexation studies (Bau, 1999;

Lozano et al., 2019a; Sun, Zhao, Zhang, & Li, 2011; Verplanck et al., 2004; Zhang & Honaker, 2018).

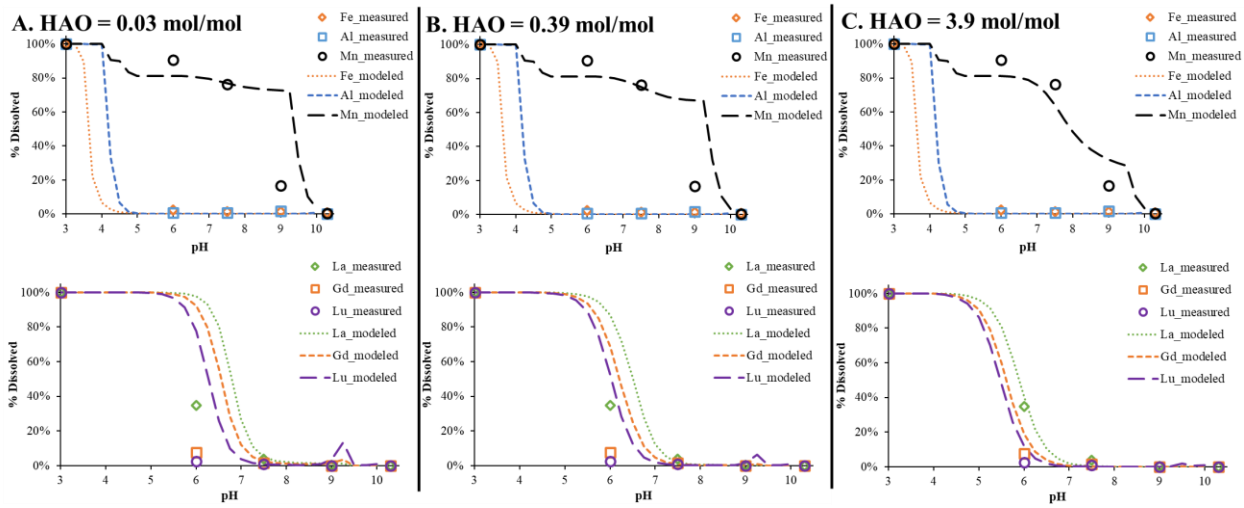

Figure 18 Modeled attenutation of Fe, Al, and Mn and select REE from the Nittanny AMD titration during NaOH showing measured data from Cravotta and Brady, 2015. REE removal is modeled as surface complexation on precipitated HFO ($Fe(OH)_3$), HAO (gibbsite), and HMO (MnOOH and $Mn(OH)_2$) surfaces. A, B, and C show identical chemistry and processes. The only difference is HAO surface properties. A is using default gibbsite surface area of 32 m^2/g for HAO for a site density of 0.03 moles of surface sites/mole $Al(OH)_3$. B is using freshly precipitated $Al(OH)_3$ surface area of 376 m^2/g for HAO for a site density of 0.39 moles of surface sites/mole $Al(OH)_3$. C is $Al(OH)_3$ with a surface site density of 3.9 moles of surface sites/mole $Al(OH)_3$.

To identify the possible processes responsible for dissolved REE attenuation, the following mechanisms were evaluated using the geochemical model: REE mineral precipitation, $(Al,REE)(OH)_3$ solid solution precipitation, and surface complexation. With the exception of CeO_2, REE mineral saturation indices were undersaturated below pH 7.75. Above that pH, some $REE(OH)_3$ minerals were oversaturated with $HREE(OH)_3$ minerals reaching saturation at a lower pH than $LREE(OH)_3$ minerals. Additionally, some $LREE_2(CO_3)_3$ minerals were oversaturated

above pH 9.25. Dissolved REE removal occurred well below the pH of REE mineral saturation suggesting REE mineral precipitation is not responsible for REE removal.

REE phosphate minerals are a major mode of REE occurrence in ore deposits and thermodynamic data for these minerals are available (Table S5). Although PO_4^{-3} concentrations are below detection in the Nittanny influent AMD, setting the dissolved P concentration at 0.02 mg/L (the detection limit) resulted in REE(PO_4) mineral precipitation from pH 4.75 to 5.75. While this is the pH range in which dissolved REE are removed, LREE(PO_4) minerals reach saturation before HREE(PO_4) minerals. This is opposite of what is observed in the titration data. Therefore, REE phosphate mineral precipitation is not considered as a viable mechanism of dissolved REE attenuation in these samples.

The co-precipitation of Al and REE is commonly observed in experimental studies (Ayora et al., 2016; Zhang & Honaker, 2018). To evaluate the potential of (Al,REE)$(OH)_3$ solid solution precipitation, the default solid solution block in PHREEQC was used with the minerals gibbsite and REE$(OH)_{3(s)}$ as two components. Results show the pH-dependent attenuation of dissolved REE from pH 6.0 to 8.5 with HREE removed at a lower pH. However, this is a higher pH than both Al and REE removal in the titration data, especially for LREE. Therefore, (Al,REE)$(OH)_3$ solid solutions are also not considered a viable REE attenuation mechanism for these samples.

To model dissolved REE removal as a surface complexation reaction, reactive surfaces first had to be generated by the model. Precipitated mineral phases to act as sites of surface complexation included Fe$(OH)_{3(a)}$, gibbsite ($Al(OH)_3$), manganite (MnOOH) and pyrochroite ($Mn(OH)_2$). Default log k values from the PHREEQC database were used for these minerals. Because observed patterns in Fe and SO_4 could be simulated by the precipitation of $Fe(OH)_3$ and

not by precipitation of schwertmannite, REE sorption on schwertmannite (Lozano et al., 2020) was not considered.

Modeled major metal removal is shown in Figure 18. $Fe(OH)_3$ precipitation was modeled as an Fe(III) precipitation reaction and a Fe(II) oxidation and precipitation reaction. MnOOH precipitation was modeled as a Mn(II) oxidation and precipitation reaction. Dissolved oxygen limited Fe(II) and Mn(II) oxidation. At pH 4.75, >99% Fe(II) was oxidized and precipitated as $Fe(OH)_3$ and 16% of Mn(II) was oxidized and precipitated as MnOOH by pH 5.0. The remaining dissolved Mn(II) was available for surface complexation reactions and precipitated as $Mn(OH)_2$ above pH 9.5. We assumed that surface properties of $Mn(OH)_2$ were identical to MnOOH. With these reactions, the modeled dissolved Na concentrations are similar to measured concentrations (Figure S14).

The model was configured so that HFO ($Fe(OH)_3$), HAO ($Al(OH)_3$), and HMO (MnOOH and $Mn(OH)_2$) surfaces were only available for reaction after precipitation. Once precipitated, surface properties (e.g. surface area (m^2/g) and surface site density ($sites/nm^2$)) determined how many surface complexation sites were available for reaction.

Initial modeling using default surface characteristics for HAO, HMO, and HFO (Table S7) underestimated dissolved REE attenuation as a function of pH (Figure 18a). Sampling results showed that at pH 6.0, 35%, 7%, and 2% of La, Gd, and Lu, respectively, is dissolved while the models showed that at pH 6.0, 72%, 46%, and 28% of La, Gd, and Lu, respectively, is dissolved. Nearly 80% of REE were removed via surface complexation with HMO and HFO (Figure S18a).

One reason for the poor model fit could be that the surface properties (surface area and site density) used for HAO are for gibbsite and may not reflect freshly precipitated amorphous $Al(OH)_3$. The methods used in gibbsite precipitation involve aging freshly precipitated $Al(OH)_3$

for 1 to 3 months, or precipitating $Al(OH)_3$ at 40°C followed by 1 month of aging (Karamalidis & Dzombak, 2010). Karamalidis and Dzombak (2010) report a wide range in surface areas for gibbsite (0.37 to 94 m^2/g) and use an average value of 32 m^2/g. However, freshly precipitated $Al(OH)_3$ has surface areas ranging from 5.9 to 774 m^2/g with an average value of 376 m^2/g (excluding the 2,000 m^2/g surface area calculated by Fukushi et al., 2006) (Fukuishi, Tsukimura, & Yamada, 2006; Gu & Karthikeyan, 2005; Manning & Goldberg, 1997; Okazaki, Sakaidani, Saigusa, & Sakaida, 1989; Rakotonarivo, Bottero, Thomas, Poirier, & Cases, 1988). Using a surface area of 376 m^2/g, HAO surface site density increases from 0.03 mole/mole $Al(OH)_3$ to 0.39 mole/mole $Al(OH)_3$. However, models using this larger surface site density value do not significantly improve REE removal (Figure 18b).

Like surface area, surface site density can also vary depending on the mineral. For example, Fukuishi et al., 2006 found a site density of 18 sites/nm^2 best fit their titration data of amorphous aluminum hydroxide; this is 2.25 times higher than the Karamalidis and Dzombak (2010) value of 8.0. Increasing surface site density to 80 sites/nm^2 dramatically increases dissolved REE attenuation as a function of pH making it consistent with the measured Nittanny titration data (Figure 18c). This model predicts that at pH 6.0, 22%, 8%, and 5% of La, Gd, and Lu, respectively, remain dissolved. Additionally, nearly 100% of dissolved REE removal occurring from pH 5 to 7 is from surface complexation on HAO (Figure S18c).

The necessity to increase HAO surface area and surface site density in the model could be due to underestimates of these values for HAO solids used in lab experiments. For example, McLaughlin et al., 1981 found that fresh $Al(OH)_3$ used in P sorption isotherms within 24 hours of precipitation sorbed approximately 70 times more P than gibbsite and approximately 2.2 times more P than $Al(OH)_3$ that was aged in distilled water for one month(McLaughlin, Ryden, & Syers,

1981). The 70 x reactivity is similar to the calibrated model here which uses HAO with 117 times the site density of gibbsite. Fresh $Al(OH)_3$ precipitated from AMD from acid neutralization reactions is likely substantially more reactive than aged and/or dried solids used in lab studies.

4.3.5.2 Application to AMD treatment systems

The calibrated model was applied to the field sites sampled in this study: Westbox, Scootac, and Woodlands. Two changes added to the model were that $CaCO_3$ was used to increase pH instead of NaOH and that the only HMO phase permitted to precipitate was manganite (MnOOH). In limestone systems, dissolved Mn(II) is removed at circumneutral pH via heterogenous autocatalytic precipitation/oxidation and/or biotically mediated precipitation/oxidation as birnessite and todorokite (Mn(III) and/or Mn(IV) containing minerals) (Luan et al., 2012; Post, 1999; Santelli et al., 2011b; Tan et al., 2010).

The model accurately simulated pH increases due to calcite dissolution. Modeled dissolved Ca concentrations at effluent pH values were similar to measured dissolved Ca concentrations and differed from measured values by 6 mg/L to 48 mg/L (Figure S20; Table S11). Major mineral (gibbsite, $Fe(OH)_{3(a)}$, manganite, calcite, and gypsum) SI values are shown in figure S21. In all models, all Fe, Al, and Mn minerals are precipitated by pH 5.5, below the pH of modeled dissolved REE removal. This means that surface complexation thermodynamics likely control REE removal, and not co-precipitation with Fe, Al, and Mn phases or the physical availability of sorbents.

REE aqueous speciation is similar regardless of AMD chemistry; Westbox is shown as an example in Figure 19 and all sites are shown in Figure S22. Models predict that the dominant REE aqueous species are $REESO_4^+$ at pH < 6, $REECO_3^+$ from pH 6 to 8 and $REE(CO_3)_2^-$ from pH 8 to 10. The transition from one major species to another (e.g. $REESO_4^-$ to $REECO_3^-$) occurs at lower pH for HREE compared to LREE.

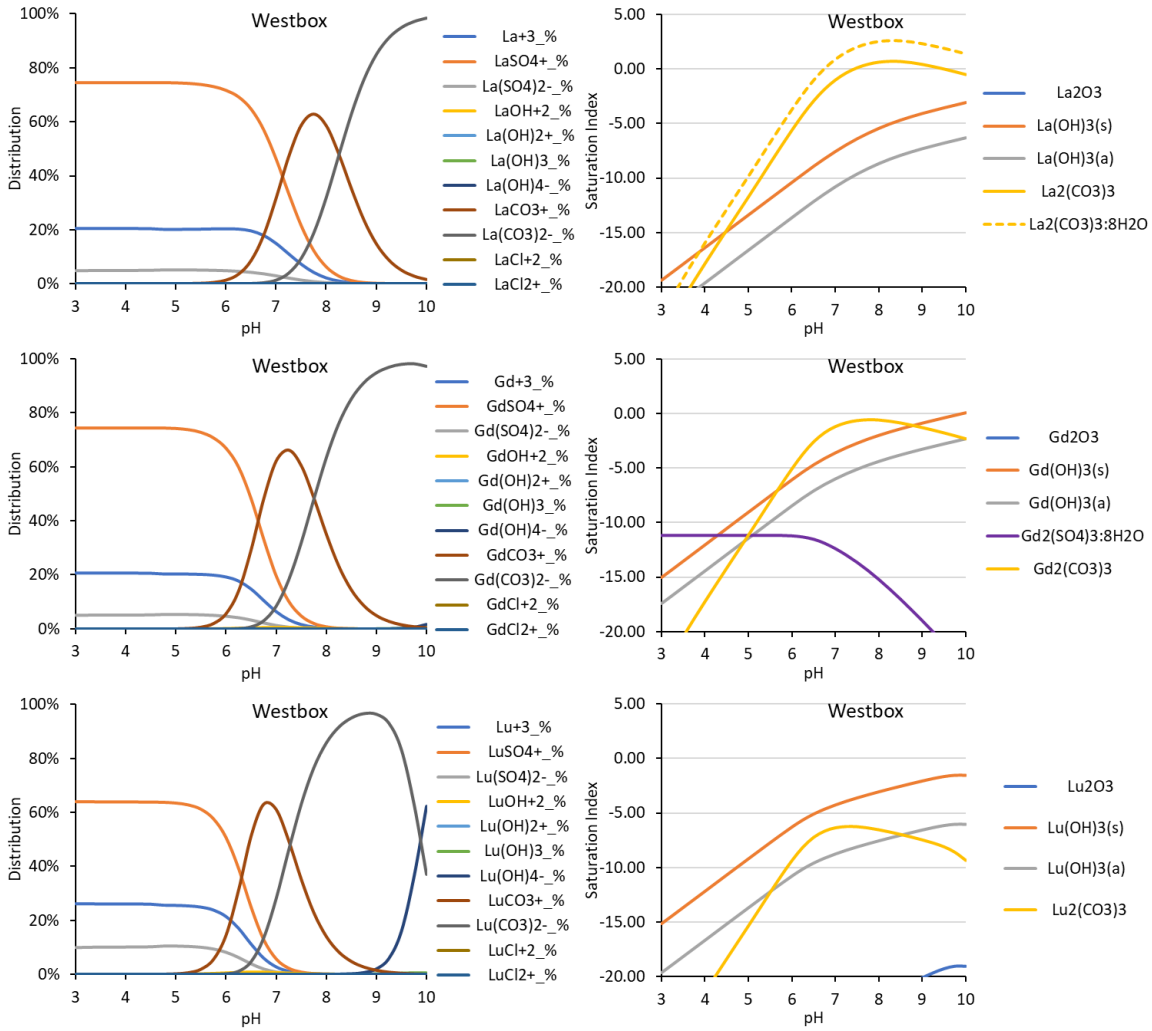

Figure 19 Simulated titration of Westbox AMD with $CaCO_3$ showing La, Gd, and Lu aqueous speciation (left) and mineral saturation indices (right) as function of pH.

REE mineral saturation indices (SI) are similarly undersaturated for all treatment systems tested here (Figure 19 and Figure S23). With the exception of CeO_2, all REE minerals are undersaturated (SI <1) below pH 6.75. From pH 7 to 9, some REE carbonate minerals (e.g. $La_2(CO_3)_3$ and $La_2(CO_3)_3{:}8H_2O$) and hydroxide carbonate minerals (e.g. $Nd(OH)CO_3$) are oversaturated. Additionally, at pH 10 some REE hydroxide minerals (e.g. $Gd(OH)_{3(s)}$) approach

saturation or are oversaturated. All REE oxide and sulfate minerals are undersaturated from pH 3 to 10.

Thermodynamic calculations suggest that REE phosphate minerals are oversaturated from pH 4 to 10. However, characterization data for the AMD solids suggests that these minerals do not precipitate, as Ce is largely oxidized to +4 and no $REEPO_4$ mineral hotspots were found in μ-XRF mapping. Therefore, $REEPO_4$ minerals were not specified to precipitate upon reaching equilibrium in the geochemical models.

Modeled REE attenuation for the Woodlands (influent pH = 3.27, Al = 19.7 mg/L, Fe = 0.7 mg/L, Mn = 0.8 mg/L, REE = 181 μg/L) treatment system match sampling data with the >90% of REE removal occurring between pH 5 and 7 (Figure 20a). Compared to the effluent at pH 6.62 where 7% and 2% of La and Gd remain dissolved, respectively (effluent Lu is below detection), the model predicts that at pH 6.75, 18%, 10%, and 8% of La, Gd, and Lu, respectively, remain dissolved. The model also predicts the removal of HREE at lower pH compared to LREE. For each liter of solution, masses of HFO, HAO, and HMO precipitated to maintain equilibrium with the solids at pH 6.50 (near that of the effluent) were computed to be 1.34 mg, 56.96 mg, and 1.27 mg, respectively.

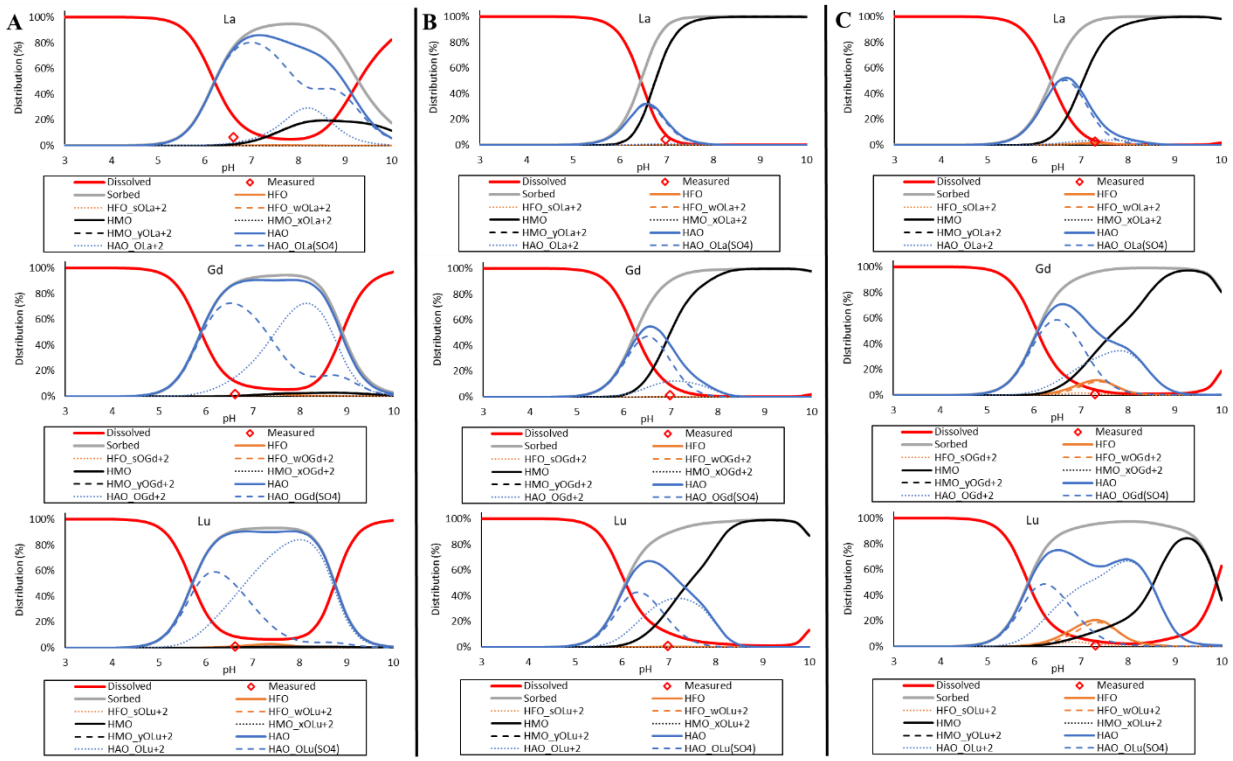

Figure 20 Distribution of REE between the dissolved (red) phase and the sorbed phase (grey) which is the summation of sorption on HAO (blue), HMO (black), and HFO (orange). Specific surface complexation sites of HAO, HMO, and HFO are shown in dotted and dashed lines of the same color. For all systems and REE, HMO_yOREE^{+2} is responsible for nearly 100% HMO surface complexation; HMO_xOREE^{+2} was a minor species. Diamond symbols are the measured data from the effluent of the treatment systems. A is Woodlands, B is Scootac, and C is Westbox.

Modeled REE removal mechanisms suggest that surface complexation on HAO is responsible for 93%, 96%, and 95% of La, Gd, and Lu removal at pH 7. HAO_OREE(SO_4) species are initially responsible for REE removal at lower pH, especially for LREE. At higher pH and for HREE, HAO_OREE^{+2} species are responsible for the majority of HAO removal of REE. LREE are preferentially adsorbed onto HMO and HMO_yOREE^{+2} sites are responsible for nearly 100% of REE removal. Less than 5% of REE were adsorbed onto HFO.

When the model is applied to Scootac (influent pH = 3.91, Al = 7.4 mg/L, Fe = <0.04 mg/L, Mn = 16.1 mg/L, REE = 151 μg/L), >90% of REE are removed between pH 5 and 7 (Figure 20b). Compared to the effluent at pH 6.98 where 4% and 1% of La and Gd remain dissolved, respectively, (effluent Lu is below detection), the model predicts that at pH 7.0, 8%, 9%, and 11% of La, Gd, and Lu, respectively, remain dissolved. The model predicts the removal of HREE begins at lower pH compared to LREE but LREE removal occurs more rapidly, and therefore within a smaller pH window, compared to HREE. For each liter of solution, masses of HFO, HAO, and HMO precipitated to maintain equilibrium with the solids at pH 7.00 (near that of the effluent) were computed to be 0.08 mg, 21.40 mg, and 25.48 mg, respectively.

Modeled REE removal mechanisms show that surface complexation on HAO and HMO are responsible for REE attenuation. HMO are responsible for a higher proportion of surface complexation of LREE (80% of La sorption at pH 7.0) whereas HAO are responsible for a higher proportion of surface complexation of HREE (66% of Lu sorption at pH 7.0). This is consistent with the findings of Hedin et al. (2019) where HAO recovered from Scootac are enriched in HREE compared to HMO recovered from the same system (Table 7).

Across all REE and pH ranges, HMO_yOREE^{+2} species predominate are responsible for nearly 100% of REE removal by HMO; although considered, HMO_xOREE^{+2} species are minor. At lower pH and for LREE, HAO_OREE(SO_4) species are responsible for REE removal. At higher pH and for HREE, HAO_OREE^{+2} species are largely responsible for the HAO removal of REE.

When the model is applied to Westbox (influent pH = 2.95, Al = 12.2 mg/L, Fe = 2.8 mg/L, Mn = 6.6 mg/L, REE = 145 μg/L), >90% of REE are removed between pH 5 and 7 (Figure 20c). Compared to the effluent at pH 7.30 where 3%, 1%, and 1% of La, Gd, and Lu remain dissolved, respectively, the model predicts that at pH 7.25, 4%, 5%, and 5% of La, Gd, and Lu, respectively,

remain dissolved. The model predicts the removal of HREE begins at lower pH compared to LREE. For each liter of solution, masses of HFO, HAO, and HMO precipitated to maintain equilibrium with the solids at pH 7.25 (near that of the effluent) were computed to be 5.36 mg, 35.27 mg, and 10.44 mg, respectively.

Modeled REE removal mechanisms show that surface complexation on HAO, HMO, and HFO are responsible for REE attenuation. HAO are initially responsible for responsible for REE removal from pH 5.5 to 6.5. However, above pH 6.5, HMO becomes the dominant sorbent for La. For Lu, HMO is not the dominant sorbent until pH 8.75. Additionally, 18% of Lu is predicted to be adsorbed to HFO at pH 7.25.

As with other treatment systems, HMO_yOREE^{+2} species are responsible for nearly 100% of REE removal by HMO; although considered, HMO_xOREE^{+2} species are minor. At lower pH and for LREE, HAO_OREE(SO_4) species are responsible for REE removal. At higher pH and for HREE, HAO_OREE^{+2} species are responsible for the majority of HAO removal of REE. HFO_wOREE^{+2} pecies are responsible for >65% of HFO sorption.

The models also largely replicate the Ce and Y removal anomalies observed in Hedin et al. (2019) and the sampling in this study. Cerium removal from Woodlands, Scootac, and Westbox is anomalously high and Y removal is anomalously low compared to neighboring REE with similar ionic radii (Figure S18). Scootac and Westbox have more pronounced Ce removal anomalies than Woodlands which the model successfully predicts. The model results also contain anomalously low Y removal which is also seen in the sampling data.

4.4 Discussion

4.4.1 REE characterization

4.4.1.1 REE distribution in Al-, Fe-, and Mn-rich solids

Due to the inverse relationship between AMD pH and REE concentrations, high concentrations of REE are typically found in AMD with high concentrations of Fe, Al, and Mn (Cravotta, 2008a). While previous work has shown a co-association between REE and Al in AMD solids (Ayora et al., 2016), the treatment of AMD can produce solids with Al, Fe, and Mn oxide/hydroxide minerals, for example the Westbox system (Table 7). Therefore, REE interaction with Fe, Al, and Mn minerals must be considered for REE removal from AMD.

Using Ce as a proxy for REE, data reported herein suggest that in AMD solids with substantial Al, Fe, and Mn content, REE could be associated with Fe and Mn minerals via surface sorption. Thermodynamic calculations show that Ce entering the AMD treatment systems sampled in this study is predominantly trivalent (Brookins, 1983). Fe and Mn oxides in lab and natural settings are well known to accumulate trace metals via surface sorption and oxidize sorbed Ce(III) to Ce(IV) (Bau & Koschinsky, 2009; Ohta & Kawabe, 2001; Takahashi, Shimizu, Usui, Kagi, & Nomura, 2000). Our XANES experiments with synthetic Mn, Fe, and Al minerals shows that Mn oxides largely oxidize sorbed Ce(III), Fe hydroxides partially oxidize sorbed Ce(III), and Al oxide hydroxides largely do not oxidize sorbed Ce(III) (Figure 21).

In AMD solids, bulk and μ-XANES show that Ce is primarily trivalent in Al-rich solids (Scootac Al and Woodlands) but is largely oxidized to +4 valence in solids with greater than 12% Fe+Mn concentrations (Scootac Mn and Westbox) (Figure 21). This is likely due to post sorption oxidation on Fe and Mn oxides/hydroxides because there is little evidence of CeO_2 precipitation

in Woodlands and Scootac Al, despise the oversaturation of CeO_2. If Ce is adsorbed to the surface of Fe and Mn minerals, other REE may also be.

Furthermore, Ce and Mn μ-XANES show little variability and generally match bulk XANES measurements suggesting Ce and Mn oxidations states are similar throughout the entire sample. Manganese μ-XANES show mean Mn valences between 3.70 to 4.00; consistent with previous work suggesting Mn minerals in AMD solids are birnessite, a Mn(IV) valence mineral, and todorokite, a mixed Mn(III) and Mn(IV) valence mineral (Table S9)(Tan et al., 2010). The presence of largely oxidized Mn oxide is significant because although REE can complex with organic matter which prohibits Ce(III) oxidation, Mn oxide can dissociate these complexes and re-adsorb REE and oxidize Ce (Davranche et al., 2008).

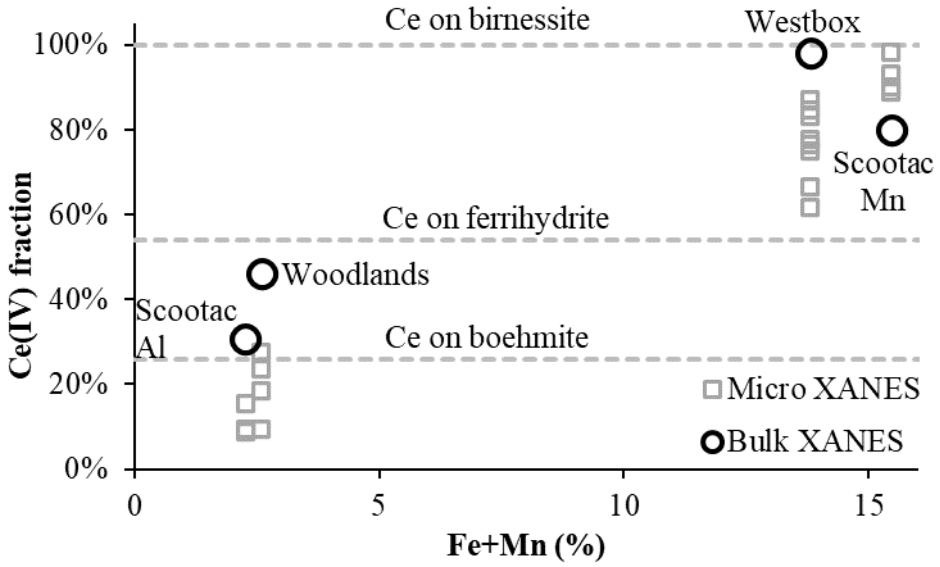

Figure 21 Ce(IV) fraction calculated from LCF of Ce bulk and μ XANES and Fe+Mn concentration in AMD solids. Horizontal dashed lines are Ce oxidation states of synthetic minerals reacted with sorbed Ce(III). Ce(IV) fraction = Ce(IV) weight / (Ce(IV) weight + Ce(III) weight).

μ-XRF maps largely support these conclusions. For Scootac-Mn, μ-XRF show that REE, Co, and Ni accumulate in the Mn crust on the exterior of limestone aggregate, like marine Fe/Mn nodules (Figure S10). For more compositionally diverse AMD solids, like Westbox, μ-XRF suggest that although Co, Ni, Cu, and Zn are mainly associated with Mn, REE can be associated with both Mn and Fe (Figure 16; Table 9).

Sequential extractions show that despite the REE removal mechanism likely being surface complexation, a very small fraction of REE are mobilized in the exchangeable phase (Figure 14). This could be due to the sequestering of REE in less available sites, such as in the octahedral sheets of birnessite, similar to how trace metals can be sequestered in clays (Post, 1999; Ryan, Hillier, & Wall, 2008).

The sequential extractions indicate that REE in Fe- and Mn- rich solids (Scootac-Mn and Westbox), are mobilized by acidic and reducing reagents, which also mobilize Al, Fe, and Mn (Figure 14). However, only fractions of the major metals are dissolved in each of the sequential extraction steps which were not selective for specific phases, a common result for sequential extractions (Ryan et al., 2008). For example, the easily reducible, moderately reducible, poorly reducible, and oxidizable fractions (extractions 4 through 7) dissolved substantial Al, Fe, and Mn in most steps (i.e., were not very selective). Furthermore, Mn oxides were dissolved in extraction 7 targeting organics because Mn oxides can dissolve with acidified H_2O_2 (Do, Batchelor, Lee, & Kong, 2009). Additionally, the high concentrations of reactive metals in AMD solids may buffer out the acids added. For example, after extractions 4 and 5 (easily reducible and moderately reducible), the final pH of the reacted solutions were one to two pH units higher than that of the extractant (Figure S25). Future sequential extractions could use larger liquid:solid ratios to ensure chemical conditions are maintained throughout each step.

Nevertheless, these sequential extractions reveal general trends that are useful to determine REE co-associations. Cobalt and REE show substantially different extraction patterns in the Scootac-Mn solids with about 75% Co and only 20% of REE in the final residual solids. This suggests that while Co and REE may be both associated with Fe and Mn, the mechanisms of associations likely differ. For example, it is well known that Co can structurally substitute for Mn in Mn oxides (Burns, 1976) so anomalous REE extraction behavior suggests they are not structurally substituted in AMD solids. Substantial Co and REE in the oxidizable phase (extraction 7) in the Westbox solids is likely a result of dissolving Mn oxides, which are soluble under acidic H_2O_2 conditions, not because of the dissolution/oxidation of organics.

Both the Scootac-Mn and Westbox solids display significant REE fractionation with certain phases. Individual REE (e.g., redox sensitive Ce, Eu) or groups of REE (e.g., LREE vs HREE) can fractionate when compared to other REE as a result of redox processes or the lanthanide contraction (the decrease in ionic radius of +3 REE with increasing atomic number). For example, anomalously low Ce in the water soluble, exchangeable, and acid soluble phases (extractions 1 – 3) for both Scootac Mn and Westbox solids suggest Ce is present as a different phase/oxidation state than other REE, possibly oxidized to Ce^{+4} by Fe/Mn oxides. The lack of Ce anomalies in Scootac-Al extractions suggest Ce^{+3} speciation, like other REE. This is consistent with Ce XANES for these solids.

The sequential extractions show substantial LREE and HREE fractionation in the moderately reducible and poorly reducible phases (extractions 5 and 6) of the Westbox and Scootac-Mn solids. Substantial fractions of HREE, Al, and Fe are associated with these phases which is consistent with the modeling results that show HREE are preferentially sorbed to $Al(OH)_3$ and $Fe(OH)_3$. Although it is not possible to separate the contribution of REE from Fe and Al

minerals, it is further evidence that Fe and Al minerals in AMD solids preferentially accumulate HREE.

While others have described Al-rich AMD solids as enriched in REE (Ayora et al., 2016; Lozano et al., 2019b; Moraes et al., 2020), these conclusions are likely not applicable to all AMD solids, especially those with substantial Fe and/or Mn fractions. A variety of potential sorbents are available in many AMD systems, such as limestone treatment systems, where Fe, Al, and Mn are removed at circumneutral pH conditions. In these systems, Mn(II) is removed at circumneutral pH via heterogeneous oxidation and precipitation as Mn(III-IV) solids. Additionally, in NaOH or $Ca(OH)_2$ treatment systems, pH is rapidly raised to precipitate all dissolved metals in a complex hydroxide slurry. In these systems, Mn(II) is removed as Mn(II) solids. Our results demonstrate that in AMD solids with Al, Fe, and Mn minerals, such as Westbox, REE can be associated with Fe and/or Mn minerals in addition to Al minerals.

4.4.1.2 REE distribution in Al rich solids

Consistent with previous findings (Ayora et al., 2016; Lozano et al., 2019b; Moraes et al., 2020), we find that REE are associated with Al minerals in the two Al-rich AMD solids examined here (Scootac Al and Woodlands). These Al-rich AMD solids arise from two different situations: 1) Woodlands AMD is primarily polluted with dissolved Al with only trace concentrations of Fe and Mn and therefore produces an Al-rich solid, and 2) while Scootac is polluted with both Al and Mn, only Al solids are mobilized by water rapidly draining out the limestone bed while Mn remains armored to the limestone aggregate (Hedin, Stuckman, Lopano, & Capo, 2019b).

Previous work has identified REE removal via monodentate inner sphere complexes with basaluminite in Al-rich AMD solids (Lozano et al., 2019b), and our work largely supports these findings. Bulk and μ Ce XANES show that Ce(III) is only partially oxidized in samples with less

than 3% Fe+Mn concentrations (Woodlands and Scootac Al). Partial oxidation suggests that a majority of Ce, and presumably other REE, are associated with solids that do not oxidize Ce(III), such as sorption on Al (sulfate)hydroxides, aluminosilicates, or organic matter. Modeling suggests that Ce(III) is not precipitated as a pure mineral or solid solution. Additionally, μ-XRF maps show that while Co, Ni, Cu, Zn, and REE are associated with Fe and Mn hotspots in the Al dominated matrix, REE present in high concentrations (e.g., La and Ce) can be widely dispersed throughout the Al matrix (Figure 17; Figure S15; Figure S16).

Sequential extractions show almost 40% of REE and Al are in the acid soluble phase (extraction 3; 1.0 M ammonium acetate) in Scootac Al solids; at least two times more than in the Scootac Mn and Westbox solids (Figure 14). Extraction 3 should dissolve Al hydroxide minerals. Ayora et al. (2016) subjected Al-rich AMD solids with sorbed REE to a similar sequential extraction regime and found about 80% TREE extraction with ammonium acetate buffered to pH 4.5 (here, we use 1.0 M ammonium acetate at pH 4.78). Additionally, Co and Mn are largely in the easily reducible phase (extraction 4), consistent with the association of Mn and Co, while less than 10% of REE are associated with this easily reducible phase. Taken together, these data suggest that while a fraction of TREE may be associated with trace Fe and Mn minerals, a substantial fraction of TREE are associated with Al minerals in Al-rich AMD solids; likely by surface complexation.

4.4.2 Geochemical models

4.4.2.1 Dissolved REE attenuation

The equilibrium geochemical models developed here accurately reproduce dissolved REE removal during the treatment of AMD. The models also show that surface complexation can

explain dissolved REE attenuation between pH 5 and 7. This is consistent with the decrease in aqueous REE concentrations above pH 5 described in multiple experiments (Ayora et al., 2016; Verplanck et al., 2004; Zhang & Honaker, 2018).

The only change to the literature values used in these models was to increase the surface area and/or site density of $Al(OH)_3$ by approximately one order of magnitude (increasing either increases the total number of surface sites). We believe this change in surface property is justified given the uncertainty and wide range of these values for other minerals. For example, HMO surface areas measured by BET-N_2 range from 74 to 296 m^2/g and site densities range from 8.8 to 367 $\mu mol/m^2$ (Tonkin et al., 2004). An alternative explanation is that the extra surface sites are from existing AMD solids in limestone systems. As AMD solids precipitate and accumulate in limestone beds, they are available for surface complexation reactions.

The removal of REE via $(Al,REE)(OH)_3$ solid solutions, while not mutually exclusive with surface complexation, is unlikely given the evidence from this study. Models predict that $(Al,REE)(OH)_3$ solid solutions to precipitate above pH 6.0, well above the pH of Al precipitation and dissolved REE attenuation. Additionally, Ce is largely oxidized to +4 in Fe- and Mn-rich solids suggesting that Ce, and presumably other REE, are not present as $(Al,REE)(OH)_3$ solid solutions, which requires a +3 valence. Finally, Lozano et al. (2019b) showed using EXAFS that dissolved Y is removed from solution via surface complexation with Al hydroxide surfaces of basaluminite. While similar mineral structural analyses of the samples in this study could definitively determine whether Al and REE are co-precipitated as solid solutions, we suggest that this mechanism is unlikely.

4.4.2.2 REE partitioning in AMD solids

The equilibrium surface complexation models presented here as titration simulations largely reproduce REE accumulation with specific minerals in AMD solids. In systems with Al^{+3} as the primary pollutant, such as Woodlands, the model with $CaCO_3$ as the titrant predicts that REE are associated with the Al minerals in formed solids; which is consistent with physical characterization and sequential extraction data. In systems with mixed sorbents (Fe, Al, and Mn minerals), like Scootac and Westbox, REE sorption on HAO occurs at lower pH than sorption on HFO or HMO. HAO_OREE(SO_4) sites are responsible for dissolved REE attenuation at the lowest pH (about 5 to 6). As pH increases above 6, HAO_$OREE^{+2}$ species are responsible for higher fraction of dissolved REE attenuation. This result is similar to the that considering HAO_$OREECO_3^+$ surface species included in modeling by Lozano et al. (2019a) which also result in REE adsorption at higher pH than HAO_OREE$(SO_4)^+$ species.

REE sorption on HMO becomes important above pH 6.0 and, if sufficient HMO sites are available, becomes the dominant sorbent above pH 7.5. The partitioning of REE between HAO and HMO minerals at circumneutral pH is critical to explaining systems like Scootac which produces both Al-rich and Mn-rich solids with high concentrations of REE. Additionally, the model predicts the preferential accumulation of HREE with HAO and LREE with HMO which is representative of the AMD solids collected from Scootac (Table 7).

Finally, in geochemically complex solids, such as those recovered from Westbox, the model predicts that REE surface complexation on HAO, HMO, and HFO are important, depending on the relative quantities of the sorbents and the pH of the solution. As with other models, REE sorb onto HAO from pH 5 to 6. Above pH 6, HMO and HFO become important sorbents. At these higher pH values, HREE are preferentially removed with HAO and HFO and LREE with HMO.

This is reflected in the μ-XRF data where REE can be associated with Mn and Fe minerals (Figure 16) and the bulk and μ XANES where Ce is largely oxidized to +4 (Figure 15).

The Westbox scenario is widely applicable to active AMD treatment systems which rapidly raise pH to 9 to 10 with NaOH or lime ($Ca(OH)_2$ or CaO) to precipitate dissolved Fe, Al, and Mn in a single slurry. The Westbox simulations (Figure 20) suggest that at these high pH conditions, sorption on HMO could be the dominant reaction controlling dissolved REE attenuation. However, the systems must have sufficient retention time to reach equilibrium, about 5 hours, for the models generated here to be representative (Lozano et al., 2020). Finally, the role of organics (e.g. humic acids), which are well known to complex REE(Marsac, Davranche, Gruau, Bouhnik-Le Coz, & Dia, 2011) could be included in future modeling.

4.5 Conclusions

Over 90% of dissolved REE are typically removed to solids during the treatment of AMD. Here, we suggest that dissolved REE are attenuated via surface complexation with Al, Fe, and Mn minerals that accumulate as sludge and surface coatings AMD treatment systems. In Al-rich AMD solids with less than 3% Fe+Mn content, REE are mostly associated with Al hydr(oxides). However, in AMD solids with over 10% Fe+Mn content, REE can be associated with Fe and Mn hydr(oxides) as well. Both empirical data and modeling data show that HREE preferentially associate with Fe and Al minerals and LREE with Mn minerals. The REE hosting minerals, identified here, can be targeted for dissolution to selectively extract REE from AMD solids (e.g., Mn oxides targeted for reductive dissolution). Additionally, and with basic information such as

untreated water chemistry and treatment technology, the geochemical models constructed here could be applied to other AMD treatment systems to predict REE-hosting minerals.

5.0 Conclusions and future work

To recover REE from AMD solids, it is critical to understand which treatment systems and AMD solids to target for recovery and what extraction methods are appropriate. This decision is complicated by the wide range of AMD chemistry, with pH values ranging from 3 to 7, and treatment technologies (e.g. limestone, NaOH, lime, low pH Fe oxidation). Previous work has shown that the highest concentrations of REE are found in low pH AMD. This study (Chapter 2) finds that REE are sequestered in AMD treatment solids when pH is raised above 5.0. Furthermore, field sampling of AMD solids showed that passive treatment systems treating low pH AMD with limestone produced AMD solids with the highest REE concentrations. Micro scale imaging analysis showed that REE can co-associate with Mn oxides in AMD solids in these systems. Finally, when comparing the total REE concentrations and % of critical REE of AMD solids to other novel REE sources and existing AMD ores, AMD solids are a promising source of REE.

An analysis of 281 AMD solids (Chapter 3) showed that Al, Mn, and Mg content of AMD solids is positively correlated with REE concentrations and the Mn content is positively correlated with Co concentrations. These data also suggests that treating low pH AMD with limestone produced solids with higher concentrations of REE compared to NaOH or lime ($Ca(OH)_2$ or CaO) treatment. Finally, the REE value in one metric ton of AMD solids ranged from $3 to $405 per metric ton which overlaps with REE ore values of $18 to $6,023 per metric ton.

These conclusions will help identify what AMD systems and AMD solids should be targeted for REE recovery. Significantly, AMD solids with high concentrations of REE, produced from limestone treatment systems with high concentration of Al and Mn, are comparable to other novel REE sources and REE ores.

In addition to identifying promising REE sources, it is critical to understand the mechanism of dissolved REE attenuation in AMD systems and any microscale element co-associations so that targeted REE extraction methods can be designed. Sequential extractions showed that REE are solubilized from AMD solids using acids and reducing agents. In addition to the widely reported association of REE with Al minerals, synchrotron micro x-ray fluorescence showed that REE can also be associated with Fe and Mn minerals. Synchrotron x-ray near edge spectroscopy analysis support these associations using Ce redox state as a proxy for REE associations. Finally, geochemical models using surface complexation on Fe, Al, and Mn minerals as the mechanism of dissolved REE attenuation accurately reproduced the pH-dependent REE removal observed in AMD treatment systems. These models also accurately predicted the preferential association of REE with specific minerals. Like the characterization data, these models suggest that REE can be associated with Al, Fe, and/or Mn minerals. These models can be applied to other systems to describe dissolved REE removal and REE accumulation on Fe, Al, and Mn oxide/hydroxide minerals. They can also be used to optimize treatment processes to produce specific minerals/solids that are enriched in REE.

These characterization data show that it is important to consider sorption reactions on Al, Fe, and Mn solids to accurately describe the fate of REE in AMD systems and that the mechanism of removal is surface complexation. The practical implications of this work include that these micro-scale REE associations can be used to design targeted extraction procedures. For example, in AMD solids where REE are associated with Fe and Mn minerals, reducing agents could be used to dissolve Fe and Mn oxides/hydroxides and liberate REE. A complexing agent could be used to inhibit the re-adsorption of REE on remaining solids (e.g. Al oxides/hydroxides).

While this study highlighted the micro scale geochemical relationships, it could be expanded to included solids produced from other treatment technologies. This study used geochemically complex solids produced from limestone treatment systems. Solids of similar compositions are produced from lime and NaOH treatment. However, the geochemical conditions in these systems are substantially different. Lime systems produce neutral to high pH (7 to 10), OH^- buffered aqueous systems with high concentrations of Ca^{+2}. Because the models developed here suggest that the microscale REE associations are pH dependent, a higher pH range could shift REE removal to being dominated by Mn sorption. Additionally, dissolved Ca^{+2} could compete with REE for surface complexation sites on Fe, Al, and/or Mn phases. Likewise, NaOH systems produce a high pH (about 10), OH^- buffered aqueous systems with high concentrations of Na^+. Like lime systems, the high pH of these systems could lead to different REE co-associations from the limestone systems investigated here.

While the geochemical models developed in this study accurately reflect the characterization data, more detailed data could improve the accuracy of these models. REE surface complexation thermodynamic data for Fe and Al solids are calculated from linear free energy relationships (LFER) of the first hydrolysis constant of REE. While the hydrous ferric oxide (HFO) LFER for REE has been used to model to existing data, with good success, the hydrous aluminum oxide (HAO) LFER has not undergone similar verification. Sorption studies could be conducted to evaluate the accuracy for the LFER HAO thermodynamic data. Additionally, more detailed AMD titrations should be carried out to better calibrate the models. Titrations should focus on a pH range from 3 to 6 and include existing AMD solids and a wide range of chemistry (i.e. varying Fe, Al, and Mn concentrations) to simulate treatment systems.

Finally, an understanding of the kinetics of REE removal in AMD systems would greatly enhance the geochemical models. Kinetics in lab experiments with REE and Fe sulfate hydroxide minerals suggest steady state conditions are reached within 5 hours (Lozano et al., 2020). However, retention time in some systems could be less than 5 hours, either by happenstance or design, and therefore the equilibrium models developed in this study may not be accurate. Incorporating REE sorption kinetics into the geochemical models developed here would make them an even more powerful predictive tool.

Appendix A: Supplemental material for chapter 2: The evaluation of critical rare earth element (REE) enriched treatment solids from coal mine drainage passive treatment systems

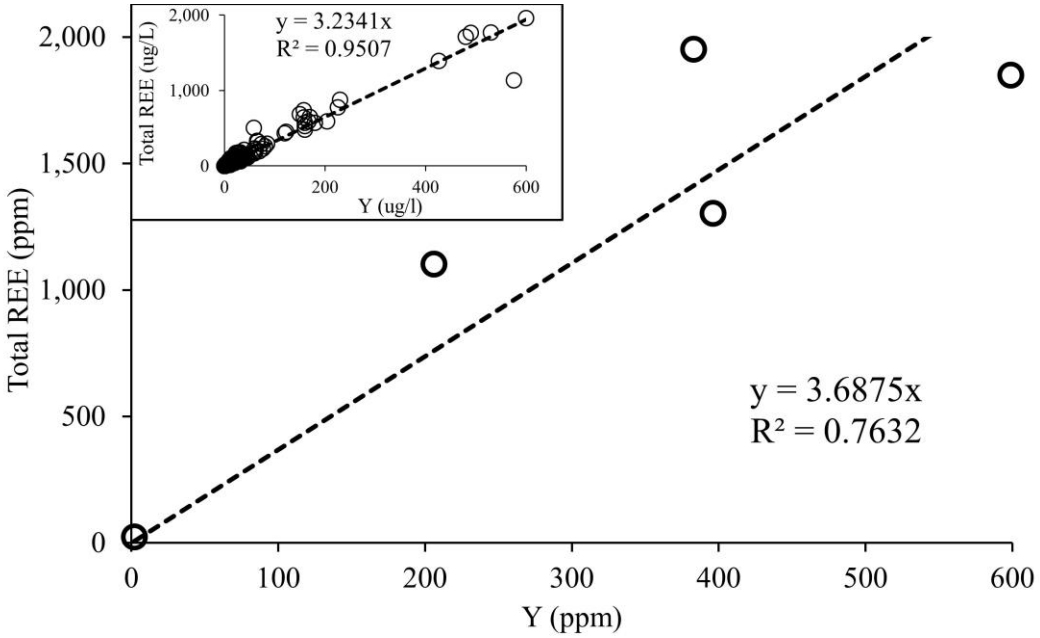

Appendix figure 1 The relationship between Y and total REE concentrations in treatment solids analyzed in this study. Inset figure is the relationship between dissolved Y and dissolved total REE concentrations in CMD across Appalachia (Cravotta, 2008; Cravotta & Brady, 2015; Stewart et al., 2017).

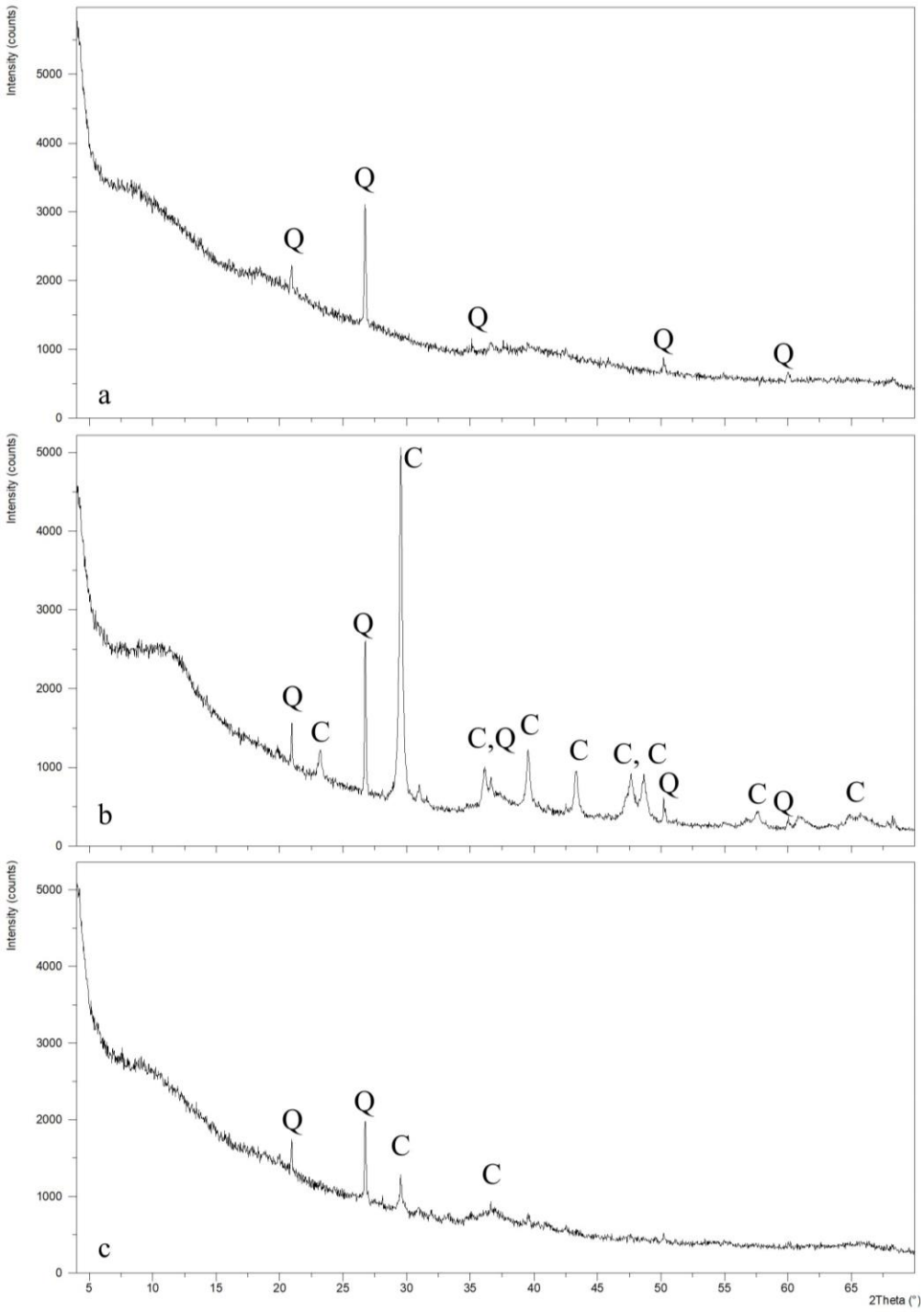
Intensity (counts)
a
Q
Q
Q
Q
Q
b
C
Q
Q
C
C,Q
C
C
C,
C
Q
C
Q
C
c
Q
Q
C
C
2Theta (°)

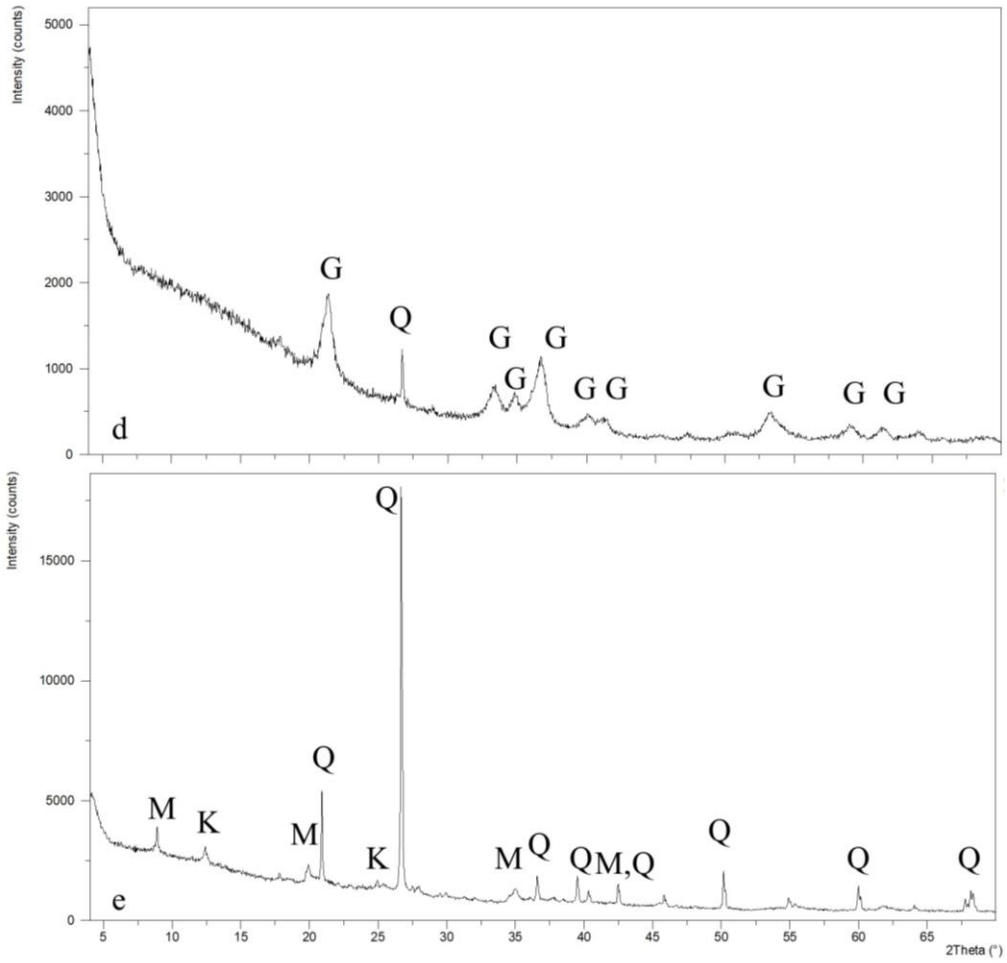

Appendix figure 2 XRD patterns plotted as Intensity (in counts) versus degrees (°) 2-theta (Cu) for select treatment solids: a) DLB-2 Al, b) DLB-2 Mn, c) DLB-4, d) LP-1, and e) DLB-1. Mineral phases of primary peaks are marked as follows: Q (quartz), C (calcite), G (goethite), K (kaolinite), and M (muscovite/illite). Samples exhibit low signal:noise and amorphous background signature between ~ 6-15 ° 2-theta; features indicative of poorly crystalline materials.

Appendix B: Supplemental material for chapter 3: Critical metal recovery potential of Appalachian acid mine drainage treatment solids

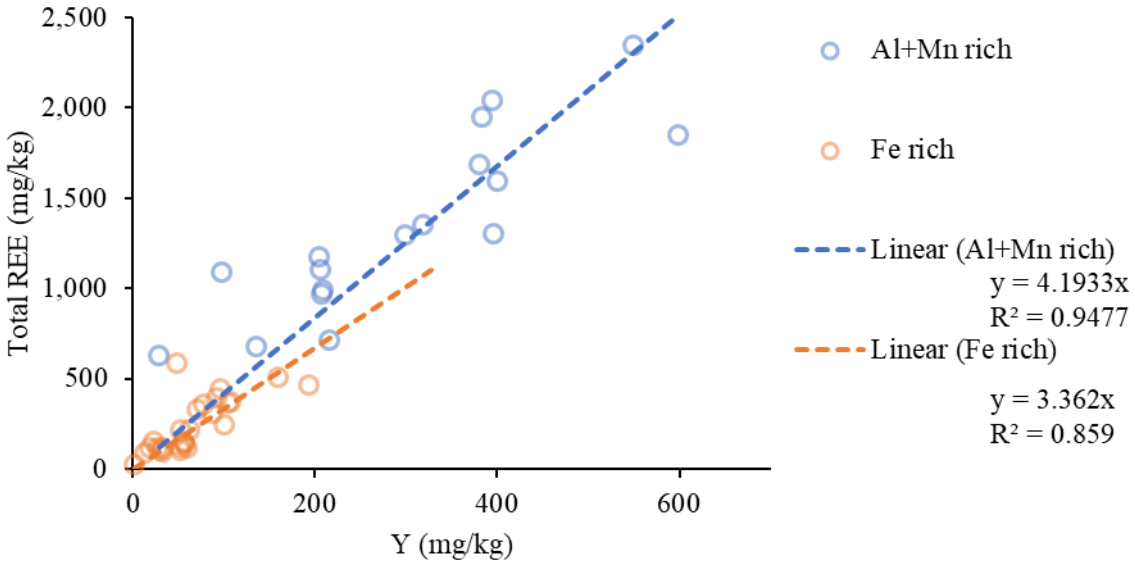

Appendix figure 3 Linear regression between Y and total REE concentrations for Al- and Mn-rich samples (>10% Al+Mn) and Fe-rich samples (>10% Fe and <10% Al+Mn).

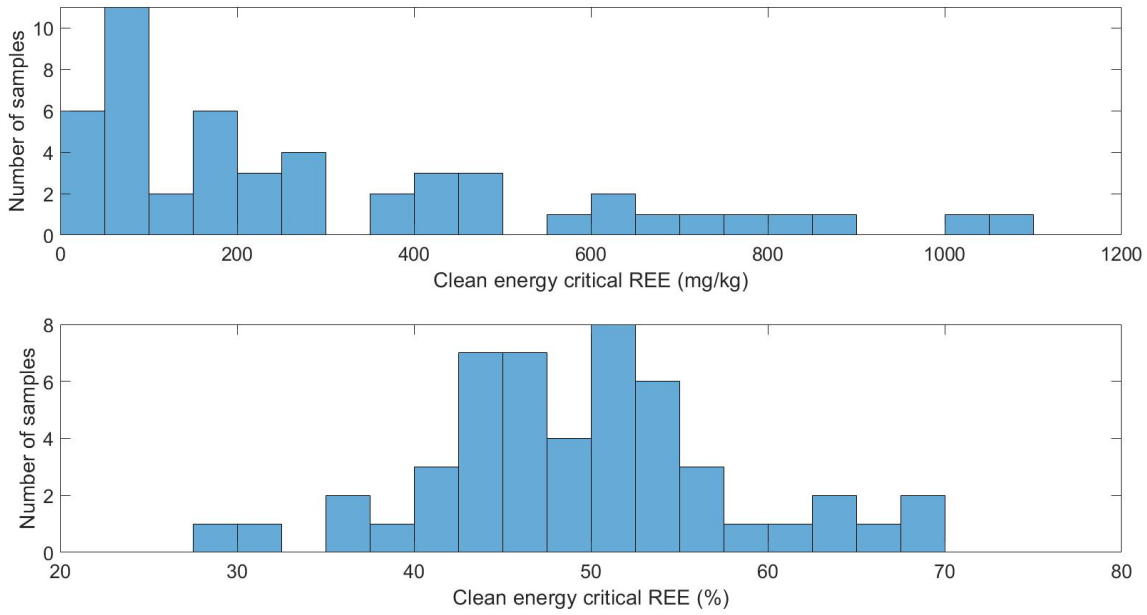

Appendix figure 4 (Top) Histogram of clean energy critical REE (Y, Nd, Dy, Eu, and Tb) concentrations. Bin width is 50 mg/kg. (Bottom) Histogram of the percentage of total REE as clean energy critical REE. Bin width is 2.5%

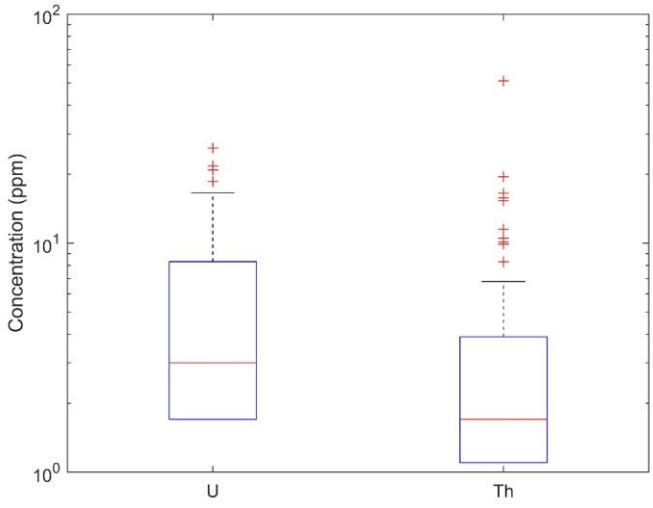

Appendix figure 5 U and Th concentrations in Appalachian AMD treatment solids. Red line is median, box limits are 25th and 75th percentiles, whiskers are the most extreme data points not considered outliers, and red crosses are outliers.

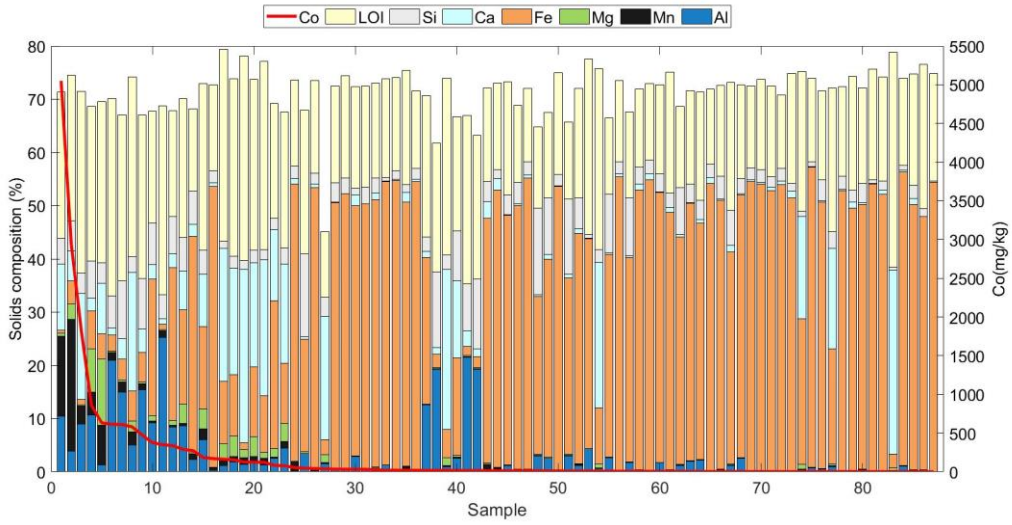

Appendix figure 6 AMD treatment solids content and Co concentrations for 87 samples from across northern Appalachia.

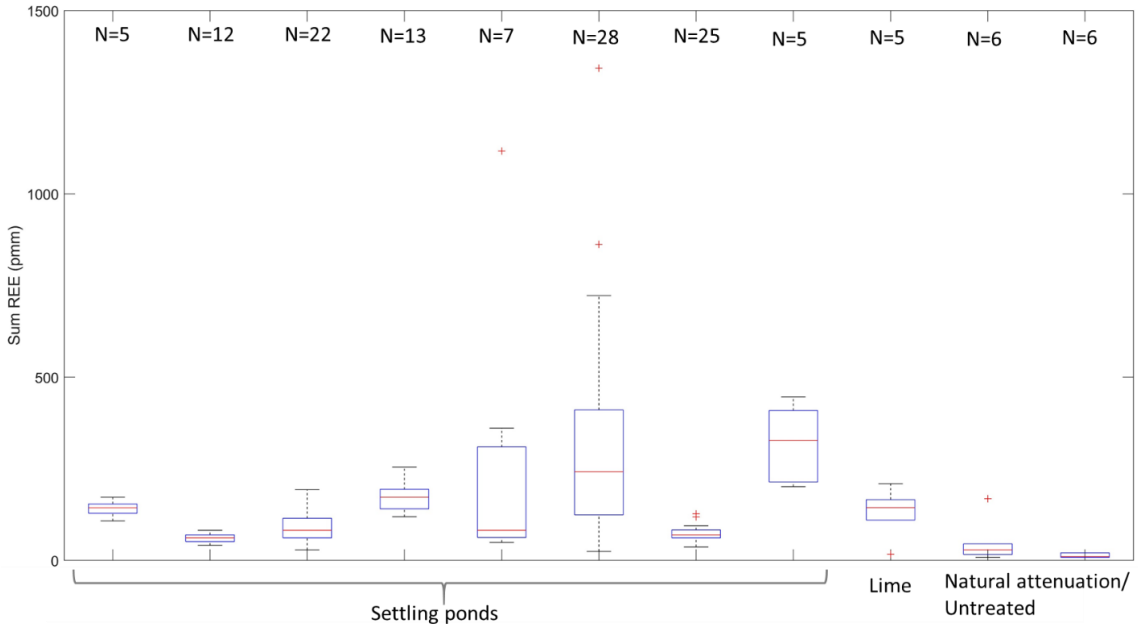

Appendix figure 7 Variance in total REE concentrations at sites from which at least 4 treatment solid samples were collected. Red line is median, box limits are 25th and 75th percentiles, whiskers are most extreme data points not considered outliers, and red crosses are outliers.

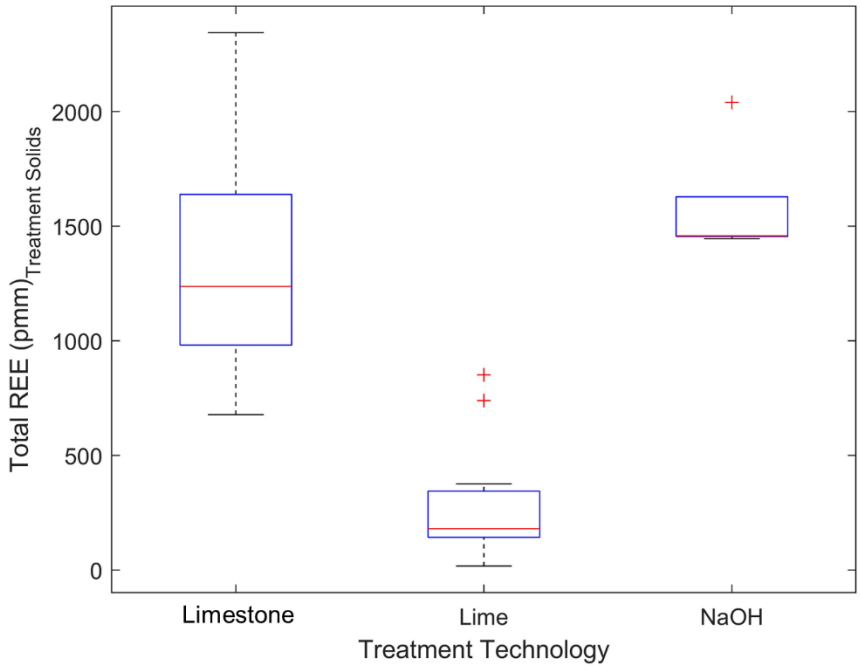

Appendix figure 8 Total REE concentrations of technologies used to treat low pH (<5) AMD. Red line is median, box limits are 25th and 75th percentiles, whiskers are the most extreme data points not considered outliers, and red crosses are outliers.

Appendix table 1 Equations used to calculate missing REE concentrations. REE values used in the calculations are NASC normalized (Gromet et al., 1984).

Table S1.
Pr = La * 0.33 + Nd * 0.66
Gd = Sm * 0.33 + Tb * 0.66
Dy = Tb * 0.80 + Yb * 0.20
Ho = Tb * 0.60 + Yb * 0.40
Er = Tb * 0.40 + Yb * 0.60
Tm = Tb * 0.20 + Yb * 0.80

Appendix table 2 REE concentrations for 13 Appalachian AMD treatment solids with all REE measured. * indicates REE calculated using the equations in Table S1. Calculated REE concentrations are maximum 2.2% of total REE concentrations. Total REE* concentrations are between 99.16% and 99.94% of total REE concentrations. The maximum variation between measured and calculated REE is 24% and 30 ppm. Average (±one standard deviation) differences are 7% (±6%) and 3.15 ppm (±5.07 ppm).

Sample	Y	La	Ce	Pr	Pr*	Nd	Sm	Eu	Gd	Gd*	Tb	Dy	Dy*	Ho	Ho*	Er	Er*	Tm	Tm*	Yb	Lu	Total REE	Total REE*
	ppm	ppm	ppm	ppm	ppm	ppm	ppm	ppm	ppm	ppm	ppm	ppm	ppm	ppm	ppm	ppm	ppm	ppm	ppm	ppm	ppm	ppm	ppm
1	599.0	113.0	291.0	54.8	53.0	262.0	86.3	23.0	123.0	109.9	19.6	118.0	122.6	22.2	21.6	62.2	66.4	9.0	9.3	57.2	9.0	1,849	1,843
2	550.0	211.0	587.0	77.9	79.6	373.0	109.0	29.5	154.0	123.6	21.2	113.0	122.8	20.8	19.8	51.7	54.6	6.2	6.7	34.5	5.0	2,344	2,327
3	396.0	143.0	274.0	41.5	41.9	181.0	44.9	11.9	62.7	59.3	10.7	62.0	63.9	12.6	10.7	33.0	30.9	4.1	4.0	22.7	3.1	1,303	1,298
4	395.0	230.0	602.0	78.2	76.0	342.0	88.6	21.8	104.0	89.2	14.6	77.9	85.8	14.1	14.1	35.9	39.7	4.5	5.0	27.1	3.9	2,040	2,035
5	392.0	147.0	283.0	42.8	42.9	185.0	46.0	12.1	64.6	60.1	10.8	62.9	64.5	12.8	10.8	33.5	31.3	4.2	4.1	23.1	3.2	1,323	1,316
6	383.0	183.0	597.0	69.4	65.9	305.0	87.5	21.4	98.1	91.5	15.2	85.5	92.1	16.2	15.7	43.6	46.3	6.0	6.2	36.1	5.3	1,952	1,951
7	381.0	142.0	431.0	56.0	56.2	267.0	82.9	22.1	111.0	93.1	15.9	85.6	92.8	15.2	15.1	38.5	42.2	4.9	5.2	27.9	4.0	1,685	1,678
8	319.0	147.0	369.0	44.0	45.6	201.0	53.3	14.3	76.6	61.9	10.7	56.7	61.8	10.6	9.9	26.2	27.1	3.1	3.3	16.8	2.4	1,351	1,343
9	298.0	123.0	359.0	42.2	42.6	195.0	55.7	14.9	78.6	64.3	11.1	58.8	64.2	10.9	10.3	27.5	28.4	3.3	3.5	17.8	2.5	1,298	1,290
10	206.0	86.9	288.0	46.8	44.2	222.0	65.5	15.5	69.7	59.2	9.2	47.1	53.1	7.9	8.5	19.2	23.3	2.4	2.8	14.4	2.1	1,103	1,101
11	88.0	15.5	52.7	8.2	8.3	41.8	15.7	4.5	26.2	24.0	4.5	25.8	26.8	4.8	4.5	12.2	13.0	1.6	1.7	9.5	1.3	312	312
12	23.0	6.0	16.2	2.5	2.7	13.3	4.7	1.2	6.5	5.3	0.9	5.2	5.3	0.9	0.9	2.2	2.4	0.3	0.3	1.6	0.3	85	84
13	2.0	4.4	8.8	1.0	1.0	4.1	1.1	0.2	0.8	0.8	0.1	0.7	0.7	0.1	0.1	0.4	0.4	0.1	0.1	0.4	0.1	24	24

Appendix table 3 Appalachian AMD treatment solid samples and analyses included in this database.

REE concentrations above detection limits	Number of samples	Analysis
Total REE (Y + all lanthanides)	13	Correlate total REE with Y
INAA analysis (Y, La, Ce, Nd, Sm, Eu, Tb, Yb, Lu)	35	Calculate missing REE via table S1 and correlate with Y
Partial REE (>1 REE, <9 REE)	45	Estimate total REE using Y
Y only	170	Estimate total REE using Y
All REE below detect	18	Unused

Appendix C: Supplemental material for chapter 4: Determination and prediction of micro scale rare earth element geochemical relationships in mine drainage treatment wastes

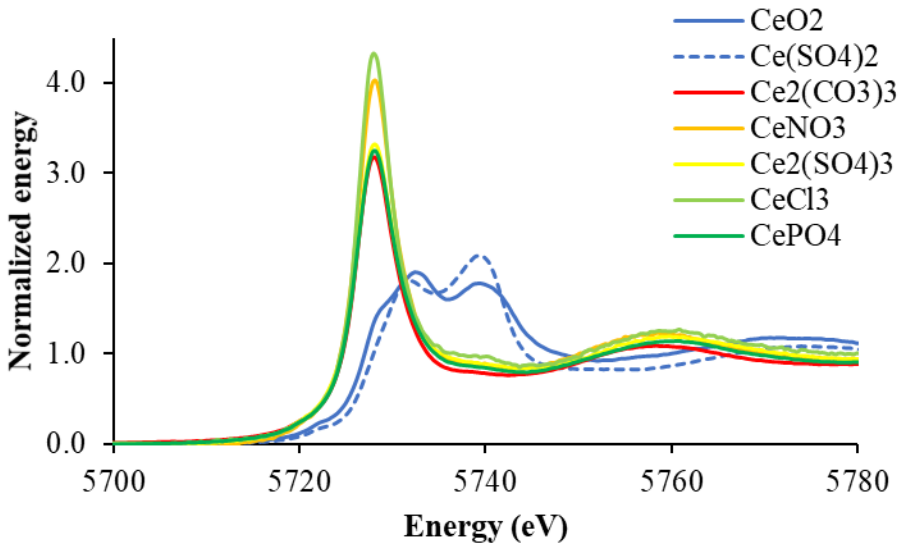

Appendix figure 9 All bulk Ce XANES standards analyzed in this study.

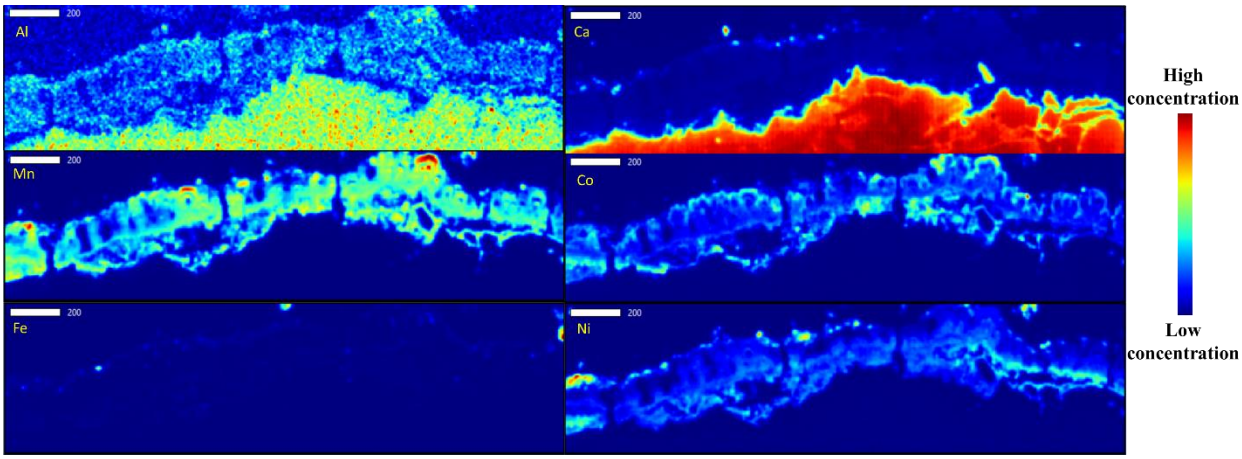

Appendix figure 10 Scootac Mn area 2 µXRF map of major and trace metals.

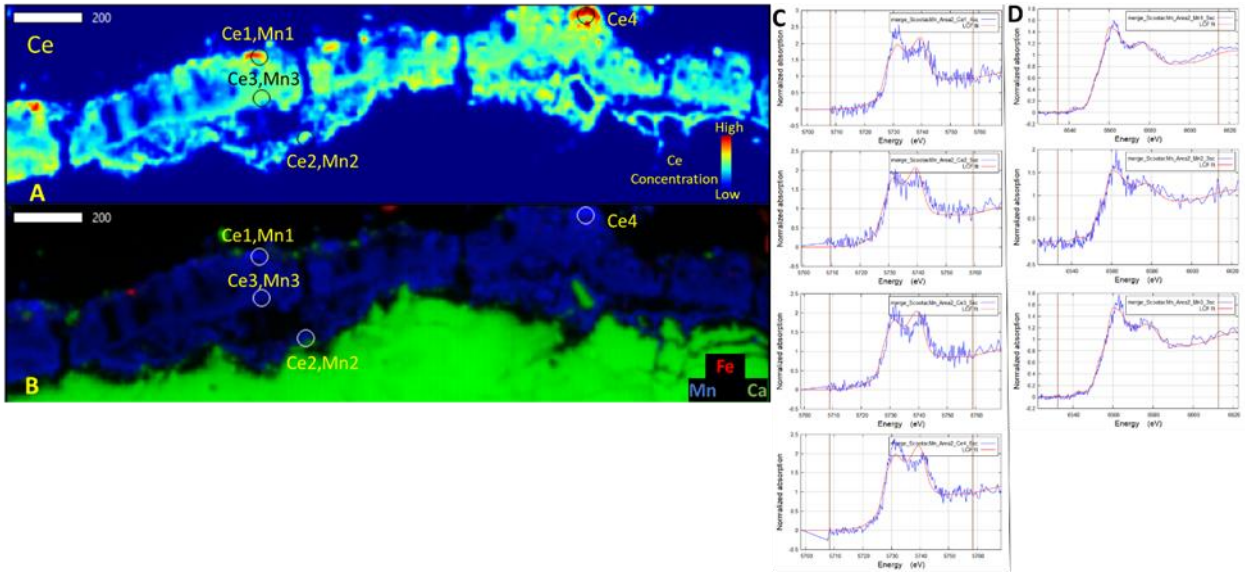

Appendix figure 11 A. Scootac Mn area 2 µ-XRF map of Ce concentrations with locations of Ce and Mn µ-XANES. B. Tricolor µ-XRF map with Fe in red, Mn in blue, and Ca in green with locations of Ce and Mn µ-XANES. C. Ce µ-XANES spectra showing measured data (blue) and results of LCF using $Ce(III)Cl_3$ and $Ce(IV)(SO_4)_2$ standards as endmembers (red). D. Mn µ-XANES spectra showing measured data (blue) and results of LCF using $Mn(II)O$, $Mn(III)_2O_3$, and $Mn(IV)O_2$ endmembers (red). Quantitative fitting results show in appendix table 9.

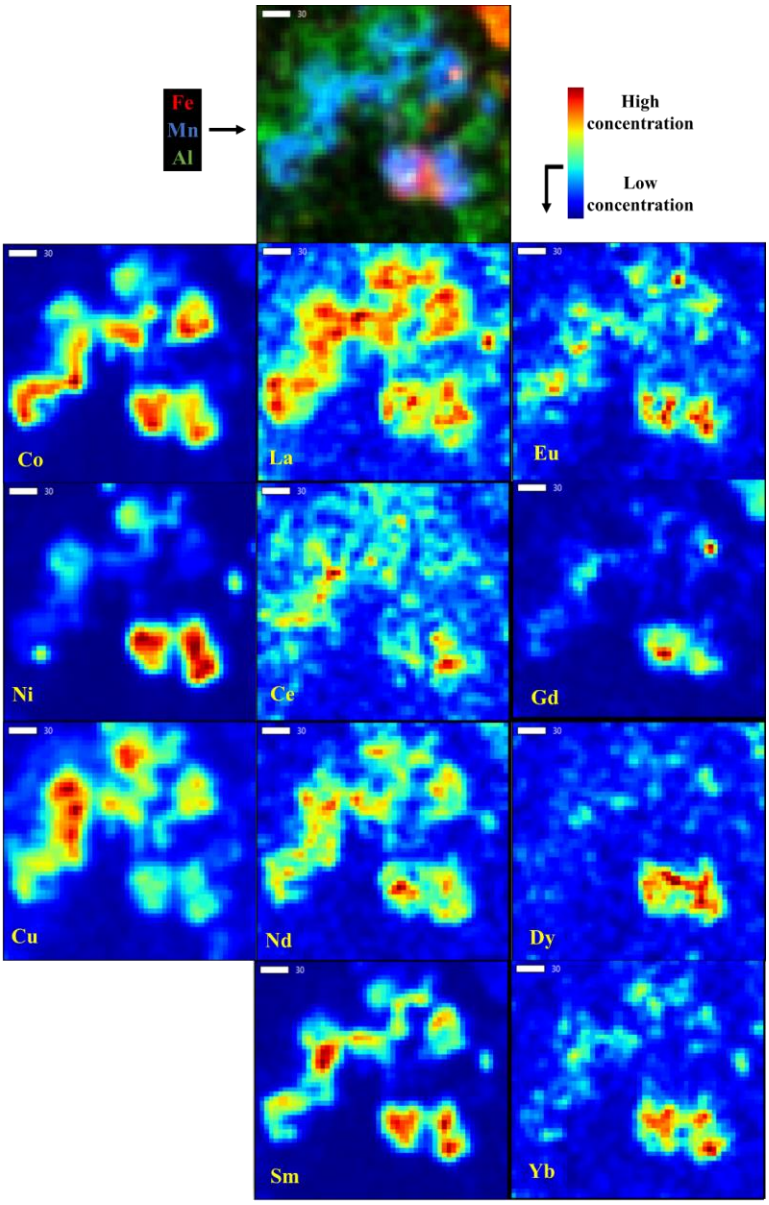

Appendix figure 12 Westbox uXRF area 3 small.

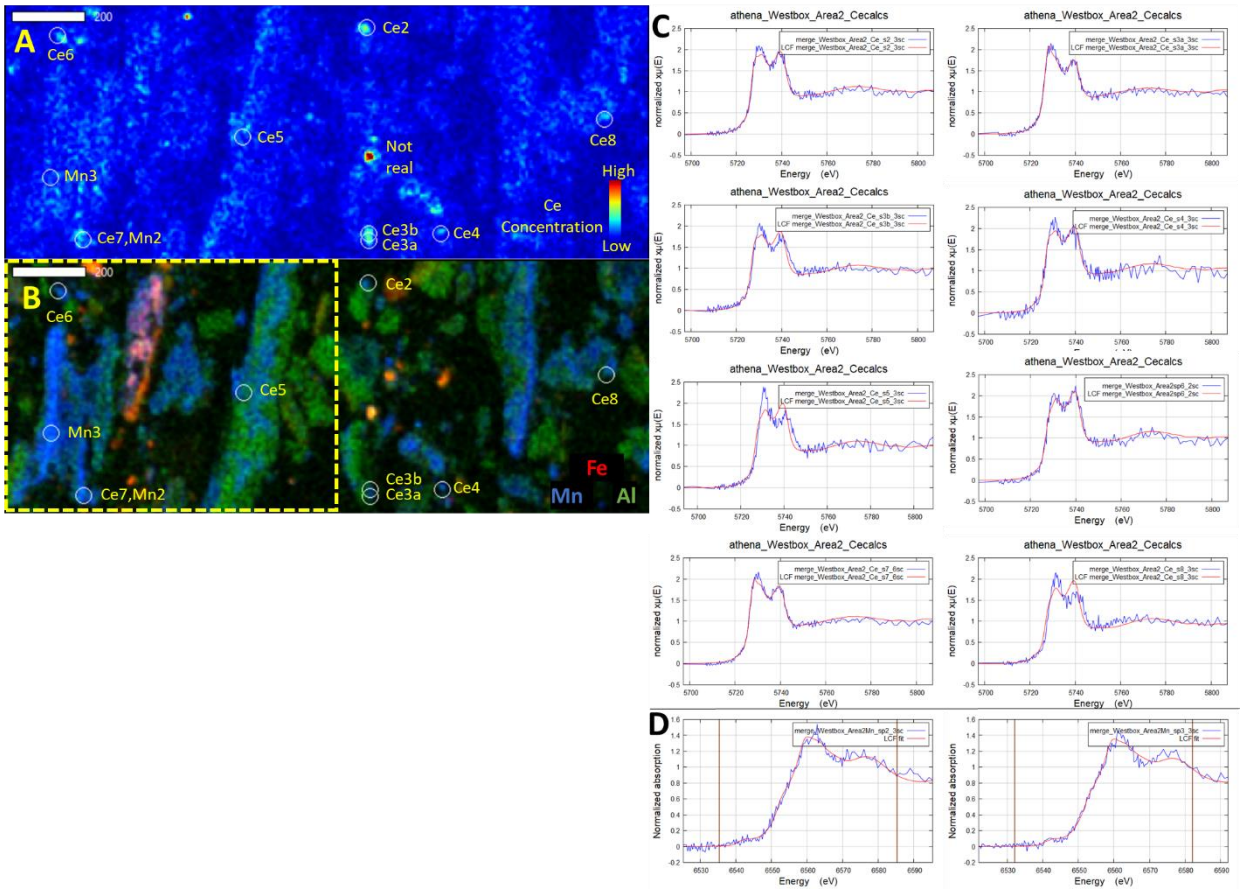

Appendix figure 13 A. Westbox area 2 µ-XRF map of Ce concentrations with locations of Ce and Mn µ-XANES. The hotspot in the middle of the map is not real (determined using pre and post Ce edge imaging (data not shown)). B. Same map area as A but with concentrations of and Fe, Mn, and Al with locations of Ce and Mn µ-XANES. Yellow dotted box shows the map area of figure 3 (area 2 small). C. Ce µ-XANES spectra show measured data (blue) and results of LCF using Ce(III)Cl and Ce(IV)$(SO_4)_2$ as endmembers (red). D. Mn µ-XANES spectra showing measured data (blue) and results of LCF using Mn(II)O, $Mn(III)_2O_3$, and $Mn(IV)O_2$ endmembers (red). Quantitative fitting results for Mn and Ce µ-XANES are show in appendix table 9 and appendix table 10, respectively.

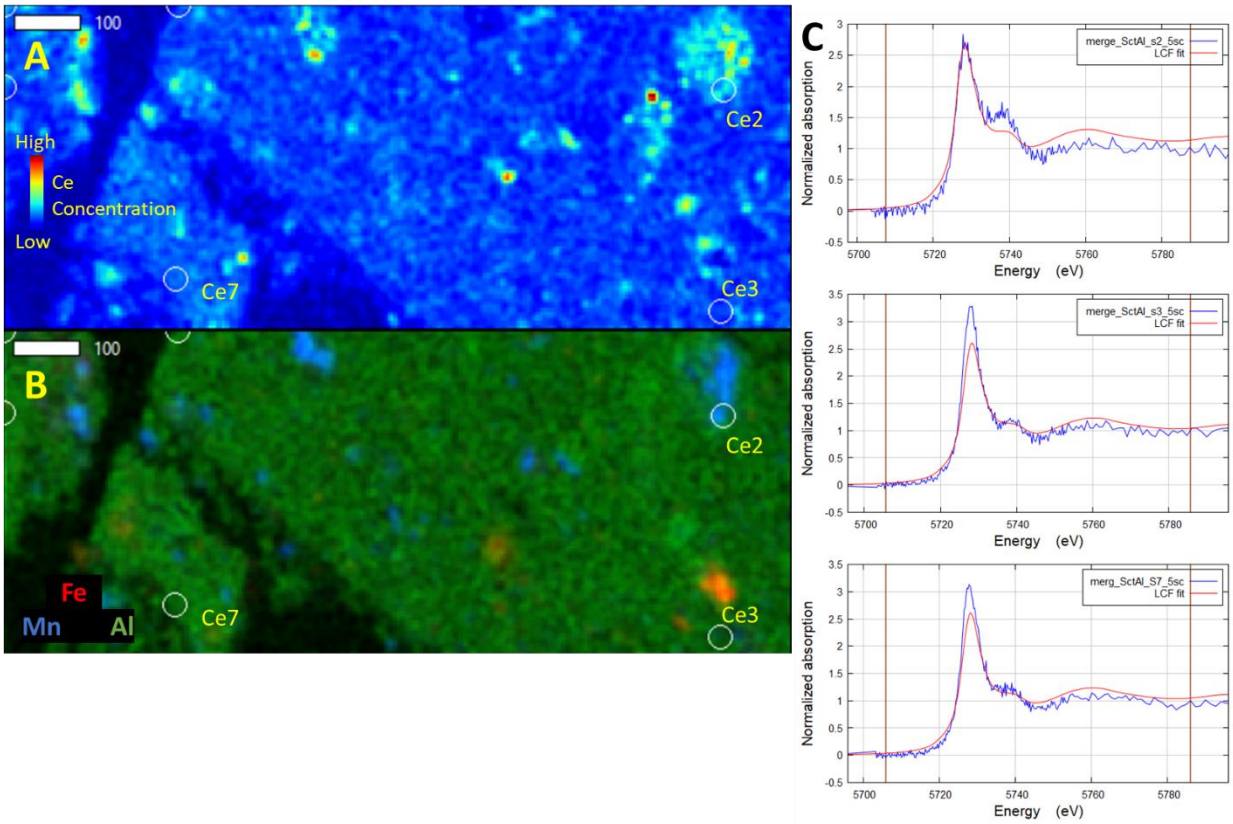

Appendix figure 14 A. Scootac Al Ce µ-XRF map with locations of Ce µ-XANES. B. Same map area as A but with concentrations of and Fe, Mn, and Al with locations of Ce µ-XANES. C. Ce µ-XANES spectra show measured data (blue) and results of LCF using Ce(III)Cl and $Ce(IV)(SO_4)_2$ as endmembers (red). Quantitative fitting results for Ce µ-XANES are show in appendix table 10.

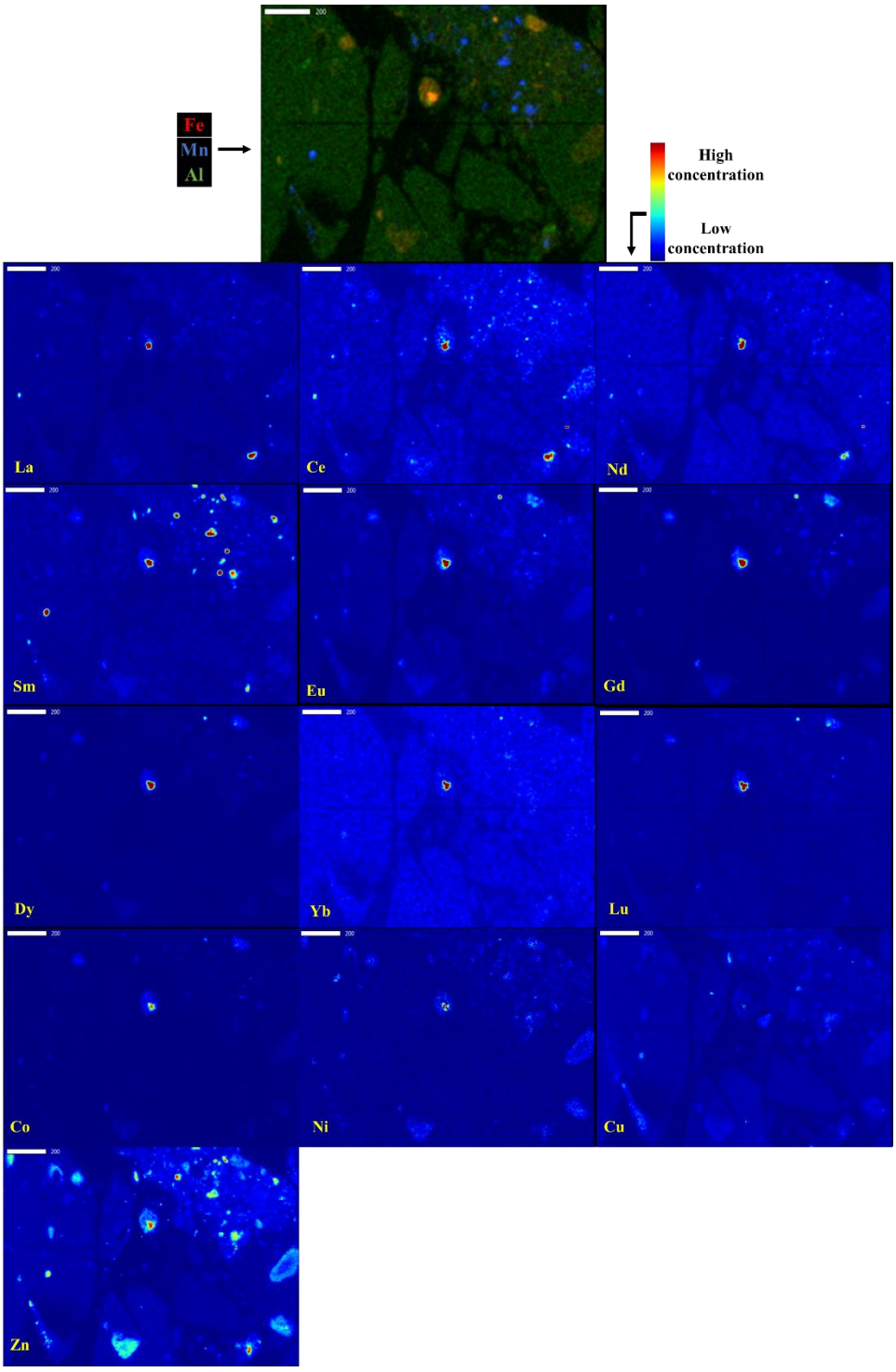

Appendix figure 15 Woodlands 1fA µXRF. The high signal spot in the middle of the map is not real (see Ce3 in appendix figure 17 of the spot).

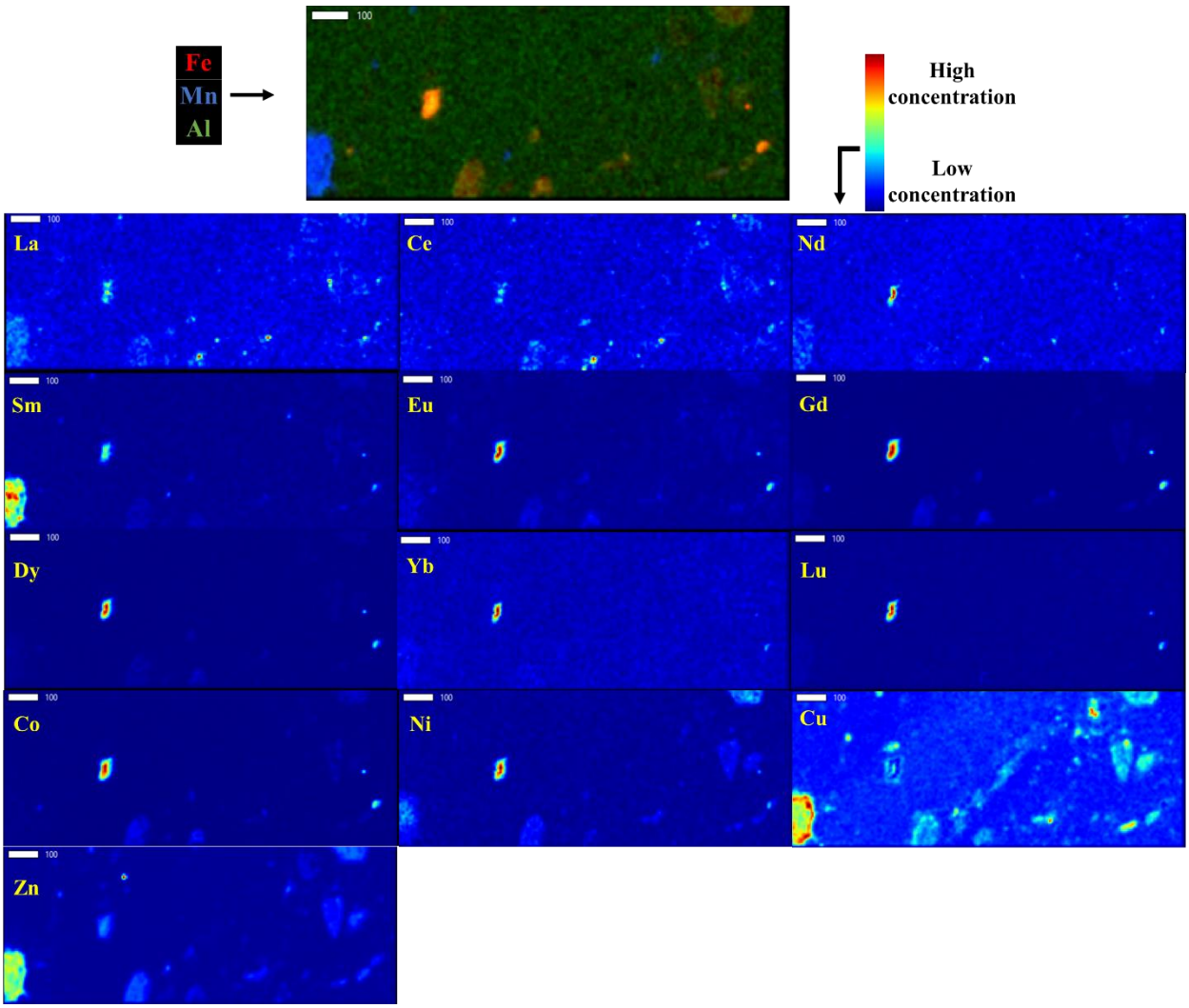

Appendix figure 16 Woodlands reg2 µXRF.

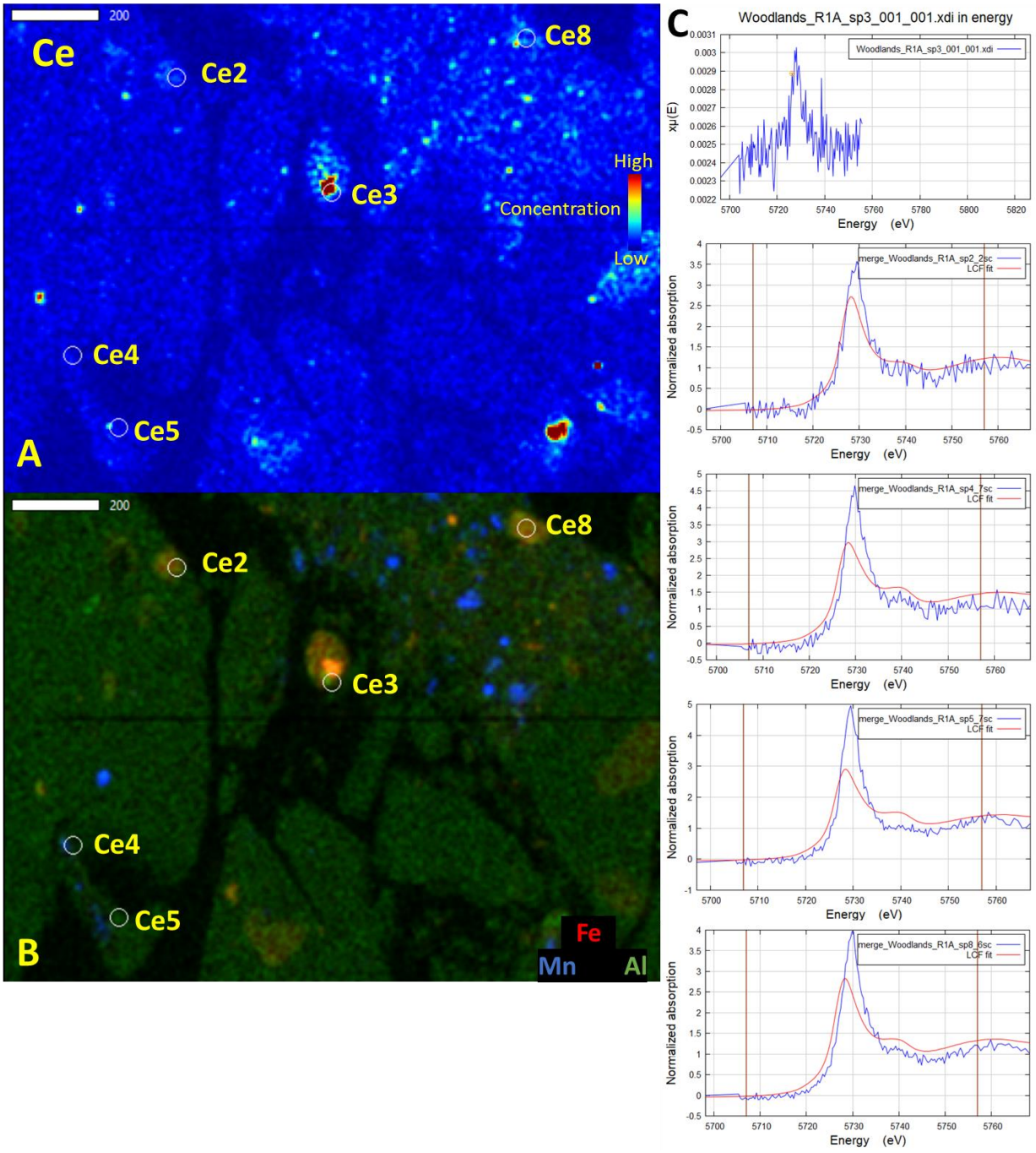

Appendix figure 17 A. Woodlands 1fA Ce µ-XRF map with locations of Ce µ-XANES. B. Same map area as A but with concentrations of and Fe, Mn, and Al with locations of Ce µ-XANES. C. Ce µ-XANES spectra show measured data (blue) and results of LCF using Ce(III)Cl and Ce(IV)$(SO_4)_2$ as endmembers (red). Quantitative fitting results for Ce µ-XANES are show in appendix table 10.

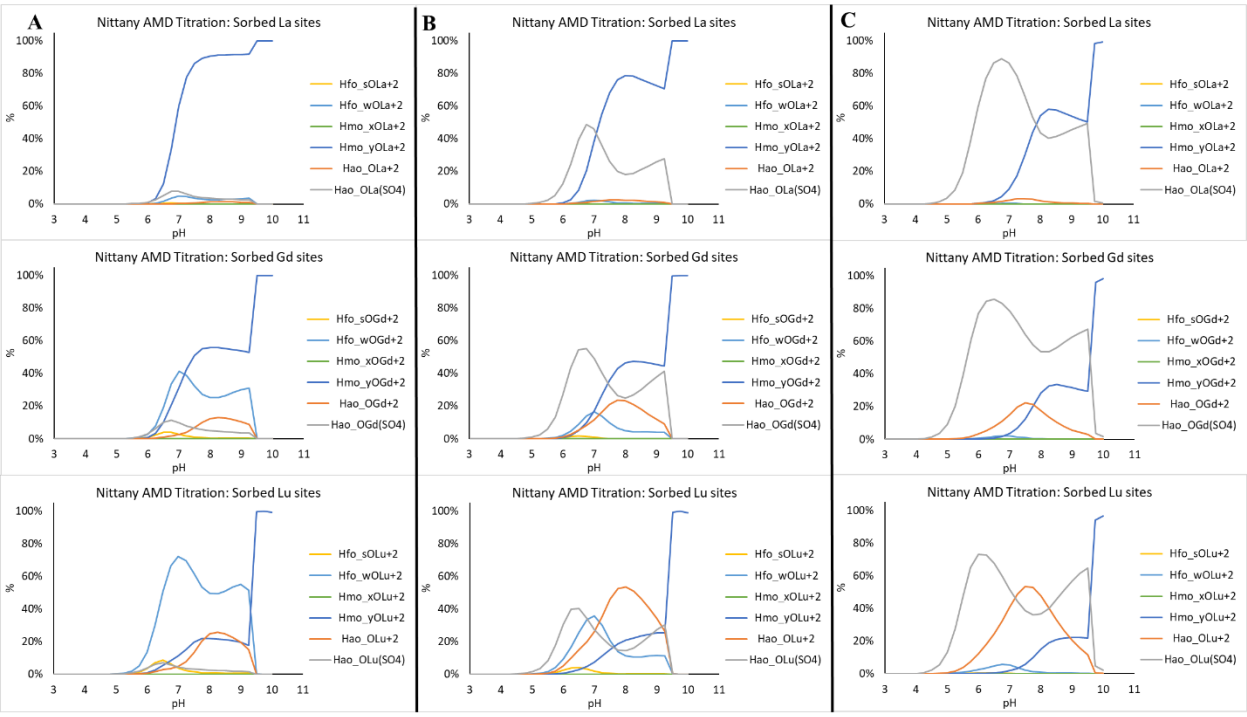

Appendix figure 18 Modeled La, Gd, and Lu surface complexation sites from the Nittanny AMD titration from Cravotta and Brady, 2015. A is using default gibbsite surface area of 32 m^2/g for HAO for a site density of 0.03 moles of surface sites/mole $Al(OH)_3$. B is using freshly precipitated $Al(OH)_3$ surface area of 376 m^2/g for HAO for a site density of 0.39 moles of surface sites/mole $Al(OH)_3$. C is $Al(OH)_3$ with a surface site density of 3.9 moles of surface sites/mole $Al(OH)_3$.

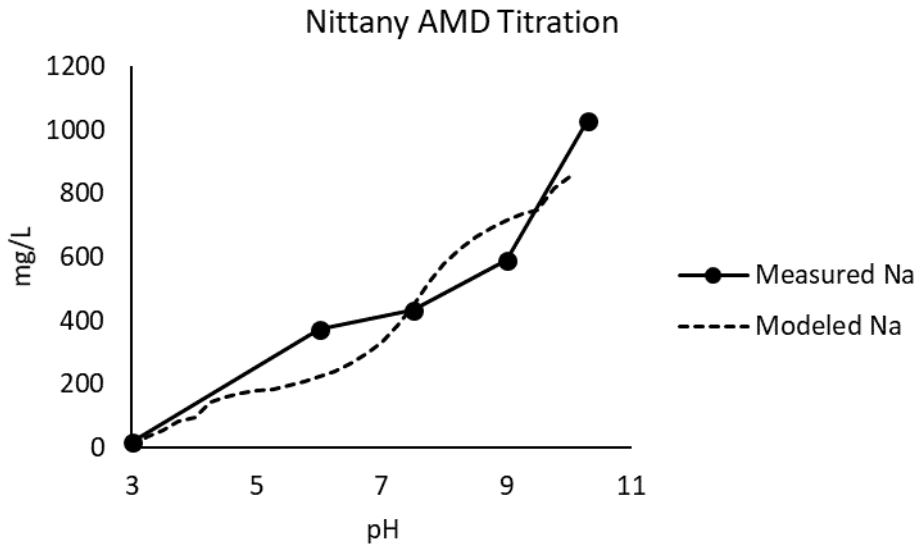

Appendix figure 19 Measured and modeled dissolved Na concentrations for the Nittanny titration from Cravotta and Brady, 2015.

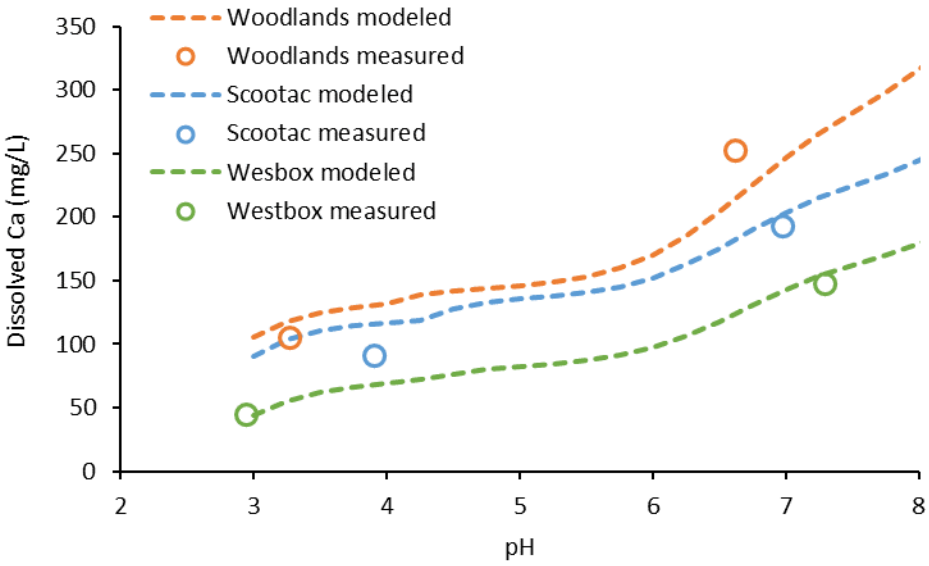

Appendix figure 20 Dissolved Ca concentrations predicted by geochemical models and concentrations measured at the influent and effluent of the treatment systems modeled in this study.

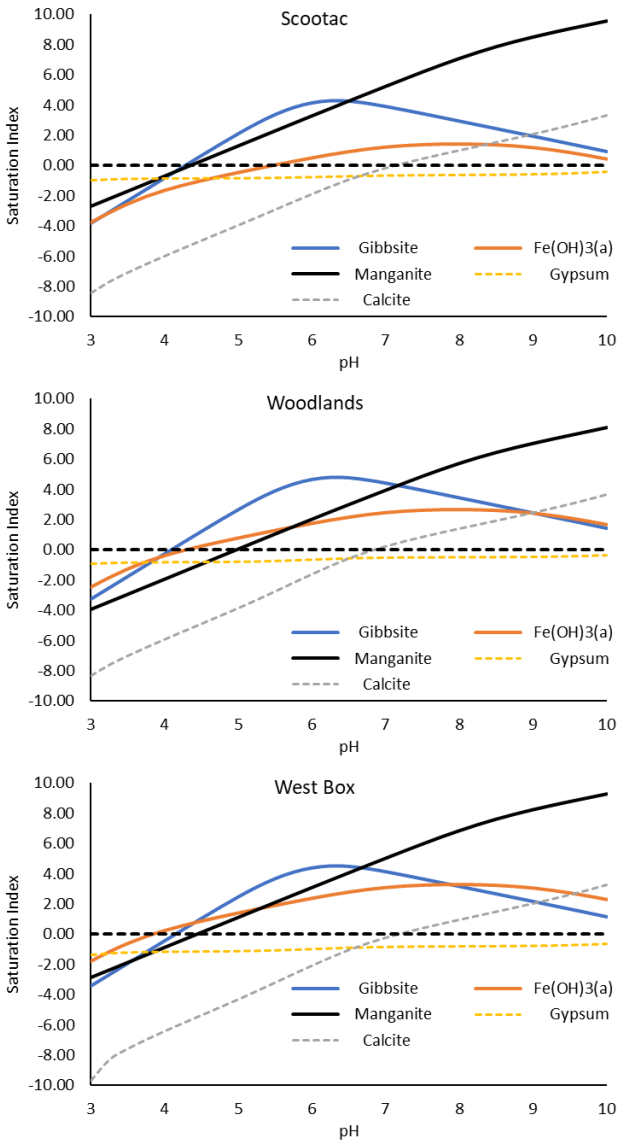

Appendix figure 21 Major mineral saturation indices for the three treatment systems modeled in this study.

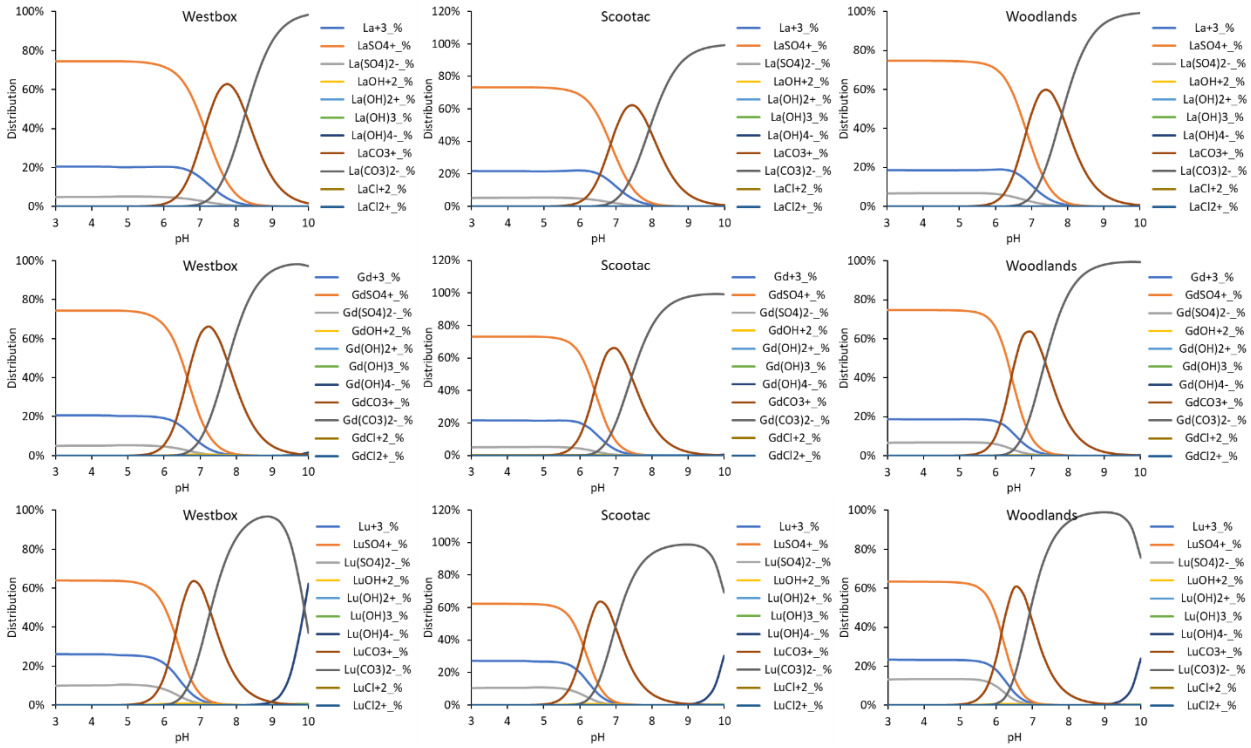

Appendix figure 22 REE aqueous speciation for all sites sampled in this study. La, Gd, and Lu are shown to illustrate atomic number trends.

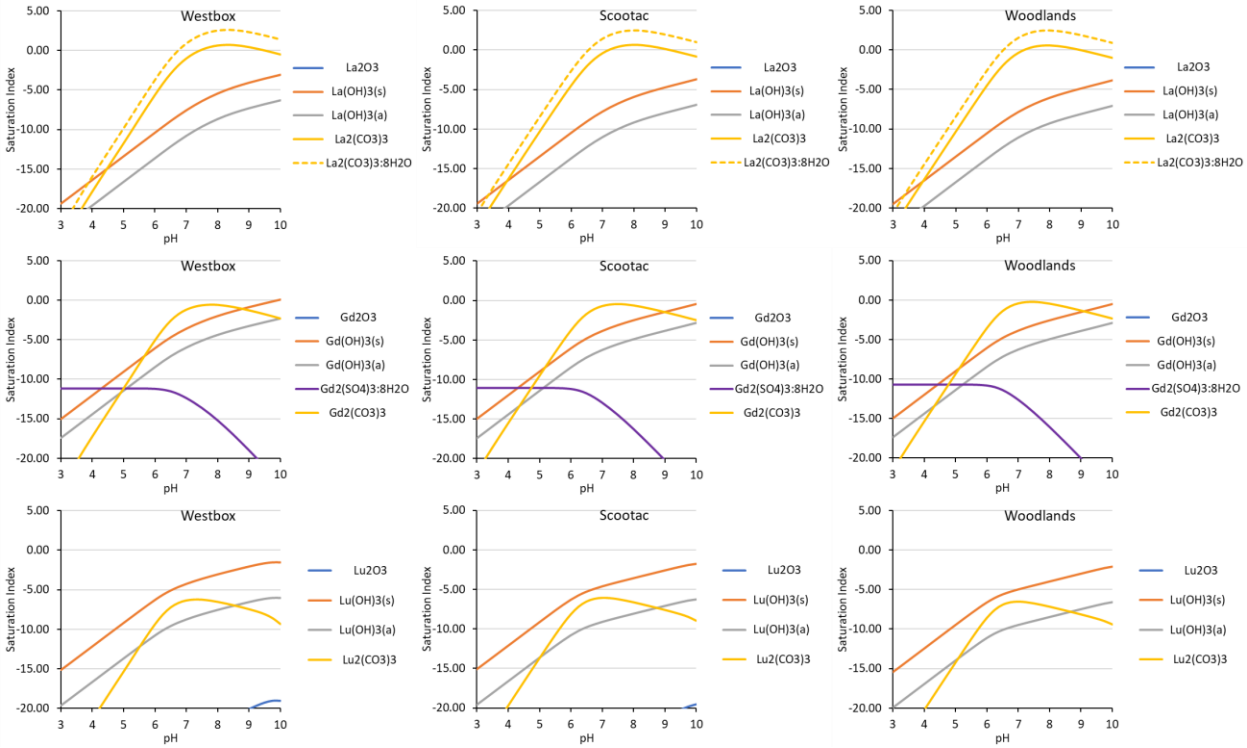

Appendix figure 23 REE mineral saturation index for all sites sampled in this study. La, Gd, and Lu are shown to illustrate atomic number trends. Different minerals are shown depending on what thermodynamic data is available.

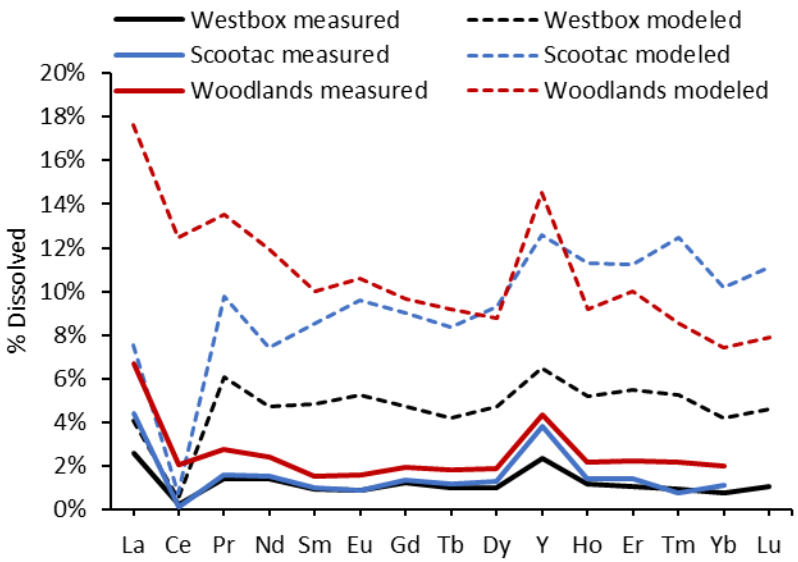

Appendix figure 24 Measured and modeled REE removal (effluent/influent) from the AMD systems modeled and/or modeled in this study.

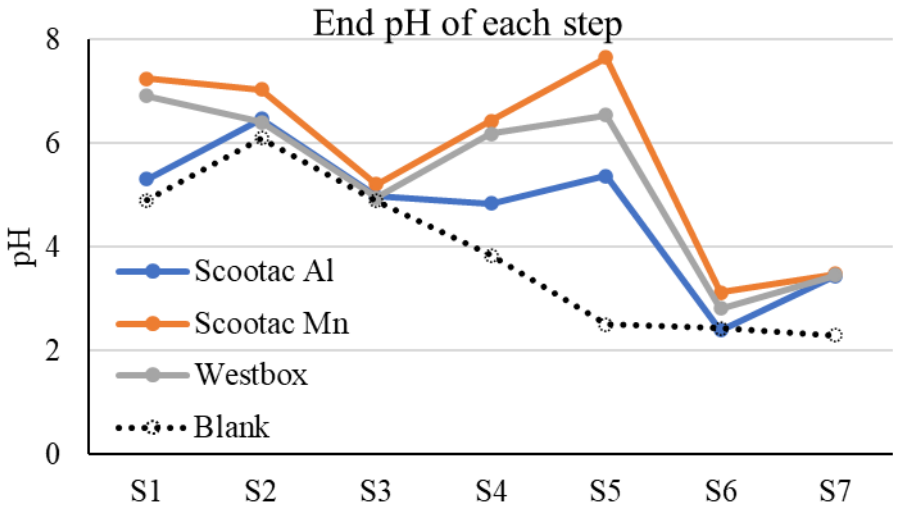

Appendix figure 25 Solution pH after sequential extractions were reacted overnight.

Appendix table 4 Log k REE aqeuous speciation data. $REE(SO_4)^{-2}$ is from the Ram et al., 2019 addition to the Thermoddem database. All other Y and Sc data is from Visual Minteq thermodynamic database. All other data is from Liu et al., 2017. Log K values are given for association reactions (e.g. $La^{+3} + SO_4^{-2} = La(SO_4)^{+}$

	La	Ce	Pr	Nd	Sm	Eu	Gd	Tb	Dy	Ho	Er	Tm	Yb	Lu	Y	Sc
$REE(OH)^{2+}$	-8.81	-8.34	-8.32	-8.18	-7.84	-7.76	-7.83	-7.64	-7.59	-7.56	-7.52	-7.39	-7.24	-7.27	-7.70	-4.30
$REE(OH)_2^{+}$	-18.14	-17.60	-17.27	-17.04	-16.51	-16.37	-16.37	-16.18	-16.10	-16.07	-15.96	-15.88	-15.74	-16.67	-16.39	-9.69
$REE(OH)_3$ (aq)	-27.90	-27.23	-26.63	-26.40	-25.91	-25.41	-2.28	-25.08	-24.83	-24.56	-24.35	-24.18	-23.85	-23.85	-25.99	-18.09
$REE(CO_3)^{+}$	6.73	7.06	7.23	7.28	7.46	7.48	7.39	7.46	7.56	7.55	7.61	7.68	7.81	7.75	7.73	no data
$REE(CO_3)_2^{-}$	11.30	11.76	12.08	12.17	12.53	12.63	12.48	12.78	12.91	13.00	13.12	13.27	13.30	13.37	11.86	no data
$REE(NO_3)^{2+}$	0.58	0.69	0.69	0.79	0.78	0.83	0.47	0.51	0.15	0.25	0.15	0.20	0.25	0.56	0.40	no data
$REE(SO_4)^{+}$	3.61	3.61	3.62	3.60	3.63	3.64	3.61	3.59	3.57	3.54	3.51	3.48	3.46	3.44	3.48	4.18
$REEF^{+2}$	3.63	3.85	3.86	3.82	4.14	4.26	4.23	4.36	4.39	4.28	4.27	4.28	4.37	4.24	4.81	7.08
$REECl^{+2}$	0.74	0.68	0.71	0.71	0.67	0.69	0.71	0.67	0.70	0.71	0.70	0.71	0.69	0.67	0.58	0.79
$REECl_2^{+}$	0.51	0.46	0.45	0.47	0.42	0.44	0.46	0.43	0.43	0.45	0.45	0.46	0.44	0.43	0.33	0.54
$REE(SO4)_2^{-}$	5.10	5.00	4.90	5.15	5.20	5.47	5.10	5.00	5.00	4.90	5.00	5.10	5.10	5.30	4.90	no data

Appendix table 5 REE mineral thermodynamic data used in this study. n/a = data not available

REE mineral	Reaction	log K	ΔH	log K source	ΔH source
Sc2O3	Sc2O3 + 6H+ = 2Sc+3 + 3H2O	11.43	n/a	Wagman et al 1982	Wagman et al 1982
Sc(OH)3	Sc(OH)3 + 3H+ = Sc+3 + 3H2O	11.33	n/a	Wagman et al 1982	Wagman et al 1982
Y2O3	Y2O3 + 6H+ = 2Y+3 + 3H2O	46.40	n/a	Spahiu and Bruno 1995	Wagman et al 1982
Y(OH)3(s)	Y(OH)3 + 3H+ = Y+3 + 3H2O	17.49	n/a	Spahiu and Bruno 1995	
Y(OH)3(a)	Y(OH)3 + 3H+ = Y+3 + 3H2O	18.99	n/a	Spahiu and Bruno 1995	
YF3	YF3 = Y+3 + 3F-	-20.07	-441.99	Spahiu and Bruno 1995	
YF3:0.5H2O	YF3:0.5H2O = Y+3 + 3F- + 0.5H2O	-16.90	n/a	Spahiu and Bruno 1995	
YCl3:6H2O	YCl3:6H2O = Y+3 + 3Cl- + 6H2O	5.83	n/a	Wagman et al 1982	Wagman et al 1982
Y2(SO4)3	Y2(SO4)3 = 2Y+3 + 3SO4-2	-0.93	n/a	Wagman et al 1982	
Y2(SO4)3:8H2O	Y2(SO4)3:8H2O = 2Y+3 + 3SO4-2 + 8H2O	-9.58	-38.26	Wagman et al 1982	
Y2(CO3)3:3H2O	Y2(CO3)3:3H2O + 3H+ = 2Y+3 + 3HCO3- + 3H2O	-1.81	n/a	Spahiu and Bruno 1995	
Y2(CO3)3	Y2(CO3)3 = 2Y+3 + 3CO3-2	-30.99	n/a	Wagman et al 1982	
La2O3	La2O3 + 6H+ = 2La+3 + 3H2O	66.20	-417.69	llnl	Wagman et al 1982
La(OH)3(s)	La(OH)3 + 3H+ = La+3 + 3H2O	20.29	n/a	llnl	
La(OH)3(a)	La(OH)3 + 3H+ = La+3 + 3H2O	23.49	n/a	llnl	

LaF3:0.5H2O	LuF3:0.5H2O = Lu+3 + 3F- + 0.5H2O	-18.70	n/a	llnl	
LaCl3	LaCl3 = La+3 + 3Cl-	14.40	-37.86	llnl	
LaCl3:7H2O	LuCl3:7H2O = Lu+3 + 3Cl- + 7H2O	4.70	n/a	llnl	
La2(CO3)3	La2(CO3)3 = 2La+3 + 3CO3-2	-33.42	n/a	Wagman et al 1982	
LaPO4:10H2O	LaPO4:10H2O +H+ = La+3 + HPO4-2 + 10H2O	-12.38	-611.25	llnl	
Ce2O3	Ce2O3 + 6H+ = 2Ce+3 + 3H2O	62.30	-221.20	llnl	Wagman et al 1982
CeO2	CeO2 + 4H+ = Ce+3 + 2H2O	-8.16	-126.90	llnl	Wagman et al 1982
CeO2	CeO2 + 4H+ + e- = Ce+3 + 2H2O	21.31	n/a	Wagman et al 1982	Wagman et al 1982
Ce(OH)3(s)	Ce(OH)3 + 3H+ = Ce+3 + 3H2O	19.89	-170.86	llnl	
Ce(OH)3(a)	Ce(OH)3 + 3H+ = Ce+3 + 3H2O	21.19	-40.03	llnl	
CeF3:0.5H2O	CeF3:0.5H2O = Ce+3 + 3F- + 0.5H2O	-18.70	-39.26	llnl	
CeCl3	CeCl3 = Ce+3 + 3Cl-	0.00	-86.59	llnl	
Ce2(SO4)3:8H2O	Ce2(SO4)3:8H2O = 2Ce+3 + 3SO4-2 + 8H2O	-8.79	-137.51	Wagman et al 1982	
Ce2(CO3)3:8H2O	Ce2(CO3)3:8H2O + 3H+ = 2Ce+3 + 3HCO3- + 8H2O	-4.11	n/a	llnl	
CePO4:10H2O	CePO4:10H2O +H+ = Ce+3 + HPO4-2 + 10H2O	-12.28	15.23	llnl	
Pr2O3	Pr2O3 + 6H+ = 2Pr+3 + 3H2O	61.40	20.88	llnl	
Pr(OH)3(s)	Pr(OH)3 + 3H+ = Pr+3 + 3H2O	19.59	-147.17	llnl	
Pr(OH)3(a)	Pr(OH)3 + 3H+ = Pr+3 + 3H2O	21.09	n/a	llnl	
PrF3:0.5H2O	PrF3:0.5H2O = Pr+3 + 3F- + 0.5H2O	-18.70	n/a	llnl	
Pr2(CO3)3	Pr2(CO3)3 + 3H+ = 2Pr+3 + 3HCO3-	-3.81	n/a	llnl	
PrPO4:10H2O	PrPO4:10H2O +H+ = Pr+3 + HPO4-2 + 10H2O	-12.28	-96.41	llnl	
Nd2O3	Nd2O3 + 6H+ = 2Nd+3 + 3H2O	58.60	33.87	llnl	Wagman et al 1982
Nd(OH)3(s)	Nd(OH)3 + 3H+ = Nd+3 + 3H2O	18.09	-409.89	llnl	
Nd(OH)3(a)	Nd(OH)3 + 3H+ = Nd+3 + 3H2O	20.49	n/a	llnl	
NdF3:0.5H2O	NdF3:0.5H2O = Nd+3 + 3F- + 0.5H2O	-18.60	n/a	llnl	
NdCl3:6H2O	NdCl3:6H2O = Nd+3 + 3Cl- + 6H2O	4.86	n/a	llnl	Wagman et al 1982
Nd2(CO3)3	Nd2(CO3)3 + 3H+ = 2Nd+3 + 3HCO3-	-3.66	-36.46	llnl	
Nd(OH)CO3	Nd(OH)CO3 + 2H+ = Nd+3 + H2O + HCO3-	2.82	-56.45	llnl	
NdPO4:10H2O	NdPO4:10H2O +H+ = Nd+3 + HPO4-2 + 10H2O	-12.18	n/a	llnl	
Sm2O3	Sm2O3 + 6H+ = 2Sm+3 + 3H2O	42.90	n/a	llnl	Wagman et al 1982
Sm(OH)3(s)	Sm(OH)3 + 3H+ = Sm+3 + 3H2O	16.49	n/a	llnl	
Sm(OH)3(a)	Sm(OH)3 + 3H+ = Sm+3 + 3H2O	18.59	-357.89	llnl	
SmF3:0.5H2O	SmF3:0.5H2O = Sm+3 + 3F- + 0.5H2O	-17.50	n/a	llnl	
SmCl3:6H2O	SmCl3:6H2O = Sm+3 + 3Cl- + 6H2O	4.72	n/a	llnl	Wagman et al 1982
Sm2(SO4)3	Sm2(SO4)3 = 2Sm+3 + 3SO4-2	-9.80	n/a	Wagman et al 1982	

Sm2(CO3)3	Sm2(CO3)3 + 3H+ = 2Sm+3 + 3HCO3-	-3.51	-39.96	llnl	
SmPO4:10H2O	SmPO4:10H2O +H+ = Sm+3 + HPO4-2 + 10H2O	-12.18	n/a	llnl	
Eu2O3	Eu2O3 + 6H+ = 2Eu+3 + 3H2O	53.05	n/a	Wagman et al 1982	Wagman et al 1982
Eu(OH)3(s)	Eu(OH)3 + 3H+ = Eu+3 + 3H2O	15.35	n/a	llnl	llnl
EuF3:0.5H2O	EuF3:0.5H2O = Eu+3 + 3F- + 0.5H2O	-16.48	n/a	llnl	
EuCl3	EuCl3 = Eu+3 + 3Cl-	19.71	-45.46	llnl	llnl
EuCl3:6H2O	EuCl3:6H2O = Eu+3 + 3Cl- + 6H2O	4.91	n/a	llnl	llnl
Eu2(SO4)3:8H2O	Eu2(SO4)3:8H2O = 2Eu+3 + 3SO4-2 + 8H2O	-10.85	-386.79	llnl	llnl
Eu2(CO3)3:3H2O	Eu2(CO3)3:3H2O + 3H+ = 2Eu+3 + 3HCO3- + 3H2O	-5.87	n/a	llnl	llnl
EuPO4:10H2O	EuPO4:10H2O +H+ = Eu+3 + HPO4-2 + 10H2O	-12.08	n/a	llnl	
Eu(NO3):6H2O	Eu(NO3)3:6H2O = Eu+3 + 3NO3- + 6H2O	1.31	n/a	llnl	llnl
Eu(Br)3	Eu(Br)3 = Eu+3 + 3Br-	29.89	-43.26	llnl	llnl
EuOCl	EuOCl + 2H+ = Eu+3 + Cl- + H2O	15.67	n/a	llnl	llnl
Eu(OH)2Cl	Eu(OH)2Cl + 2H+ = Eu+3 + Cl- + 2H2O	8.80	-370.39	llnl	
Eu(OH)2.5Cl0.5	Eu(OH)2.5Cl0.5 + 2.5H+ = Eu+3 + 0.5Cl- + 2.5H2O	12.55	n/a	llnl	
EuOHCO3	EuOHCO3 + 2H+ = Eu+3 + HCO3- + H2O	2.52	n/a	llnl	
Gd2O3	Gd2O3 + 6H+ = 2Gd+3 + 3H2O	53.80	n/a	llnl	Wagman et al 1982
Gd(OH)3(s)	Gd(OH)3 + 3H+ = Gd+3 + 3H2O	15.59	n/a	llnl	
Gd(OH)3(a)	Gd(OH)3 + 3H+ = Gd+3 + 3H2O	17.99	-364.59	llnl	
GdF3:0.5H2O	GdF3:0.5H2O = Gd+3 + 3F- + 0.5H2O	-16.90	n/a	llnl	
GdCl3:6H2O	GdCl3:6H2O = Gd+3 + 3Cl- + 6H2O	4.64	n/a	llnl	Wagman et al 1982
Gd2(SO4)3:8H2O	Gd2(SO4)3:8H2O = 2Gd+3 + 3SO4-2 +8H2O	-13.73	n/a	Wagman et al 1982	Wagman et al 1982
Gd2(CO3)3	Gd2(CO3)3 + 3H+ = 2Gd+3 + 3HCO3-	-3.71	n/a	llnl	
GdPO4	GdPO4:H2O = Gd+3 + PO4-3 +H2O	-23.33	n/a	llnl	
GdPO4:10H2O	GdPO4:10H2O +H+ = Gd+3 + HPO4-2 + 10H2O	-11.98	-391.89	llnl	
Tb2O3	Tb2O3 + 6H+ = 2Tb+3 + 3H2O	47.10	n/a	llnl	Wagman et al 1982
Tb(OH)3(s)	Tb(OH)3 + 3H+ = Tb+3 + 3H2O	15.69	n/a	llnl	
Tb(OH)3(a)	Tb(OH)3 + 3H+ = Tb+3 + 3H2O	18.79	n/a	llnl	
GdF3:0.5H2O	TbF3:0.5H2O = Tb+3 + 3F- + 0.5H2O	-16.70	-44.96	llnl	
GdCl3:6H2O	TbCl3:6H2O = Tb+3 + 3Cl- + 6H2O	4.86	n/a	llnl	Wagman et al 1982
Tb2(CO3)3	Tb2(CO3)3 + 3H+ = 2Tb+3 + 3HCO3-	-3.21	n/a	llnl	
TbPO4:10H2O	TbPO4:10H2O +H+ = Tb+3 + HPO4-2 + 10H2O	-11.98	-309.29	llnl	
Dy2O3	Dy2O3 + 6H+ = 2Dy+3 + 3H2O	47.00	n/a	llnl	Wagman et al 1982
Dy(OH)3(s)	Dy(OH)3 + 3H+ = Dy+3 + 3H2O	15.89	n/a	llnl	
Dy(OH)3(a)	Dy(OH)3 + 3H+ = Dy+3 + 3H2O	17.49	n/a	llnl	

DyF3:0.5H2O	DyF3:0.5H2O = Dy+3 + 3F- + 0.5H2O	-16.50	-50.56	llnl	
DyCl3:6H2O	DyCl3:6H2O = Dy+3 + 3Cl- + 6H2O	5.34	n/a	llnl	Wagman et al 1982
Dy2(CO3)3	Dy2(CO3)3 + 3H+ = 2Dy+3 + 3HCO3-	-3.01	n/a	llnl	
DyPO4:10H2O	DyPO4:10H2O +H+ = Dy+3 + HPO4-2 + 10H2O	-11.98		llnl	
Ho2O3	Ho2O3 + 6H+ = 2Ho+3 + 3H2O	47.30		llnl	Wagman et al 1982
Ho(OH)3(s)	Ho(OH)3 + 3H+ = Ho+3 + 3H2O	15.39		llnl	
Ho(OH)3(a)	Ho(OH)3 + 3H+ = Ho+3 + 3H2O	17.79		llnl	
HoF3:0.5H2O	HoF3:0.5H2O = Ho+3 + 3F- + 0.5H2O	-16.40		llnl	
HoCl3:6H2O	HoCl3:6H2O = Ho+3 + 3Cl- + 6H2O	5.53		llnl	Wagman et al 1982
Ho2(CO3)3	Ho2(CO3)3 + 3H+ = 2Ho+3 + 3HCO3-	-2.81		llnl	
HoPO4:10H2O	HoPO4:10H2O +H+ = Ho+3 + HPO4-2 + 10H2O	-11.88		llnl	
Er2O3	Er2O3 + 6H+ = 2Er+3 + 3H2O	42.10		llnl	Wagman et al 1982
Er(OH)3(s)	Er(OH)3 + 3H+ = Er+3 + 3H2O	14.99		llnl	
Er(OH)3(a)	Er(OH)3 + 3H+ = Er+3 + 3H2O	18.99		llnl	
ErF3:0.5H2O	ErF3:0.5H2O = Er+3 + 3F- + 0.5H2O	-16.30		llnl	
ErCl3:6H2O	ErCl3:6H2O = Er+3 + 3Cl- + 6H2O	5.53		llnl	Wagman et al 1982
Er2(CO3)3	Er2(CO3)3 + 3H+ = 2Er+3 + 3HCO3-	-2.61		llnl	
ErPO4:10H2O	ErPO4:10H2O +H+ = Er+3 + HPO4-2 + 10H2O	-11.88		llnl	
Tm2O3	Tm2O3 + 6H+ = 2Tm+3 + 3H2O	44.70		llnl	Wagman et al 1982
Tm(OH)3(s)	Tm(OH)3 + 3H+ = Tm+3 + 3H2O	14.99		llnl	
Tm(OH)3(a)	Tm(OH)3 + 3H+ = Tm+3 + 3H2O	17.29		llnl	
TmF3:0.5H2O	TmF3:0.5H2O = Tm+3 + 3F- + 0.5H2O	-16.20		llnl	
Tm2(CO3)3	Tm2(CO3)3 + 3H+ = 2Tm+3 + 3HCO3-	-2.41		llnl	
TmPO4:10H2O	TmPO4:10H2O +H+ = Tm+3 + HPO4-2 + 10H2O	-11.88		llnl	
Yb2O3	Yb2O3 + 6H+ = 2Yb+3 + 3H2O	47.80		llnl	Wagman et al 1982
Yb(OH)3(s)	Yb(OH)3 + 3H+ = Yb+3 + 3H2O	14.69		llnl	
Yb(OH)3(a)	Yb(OH)3 + 3H+ = Yb+3 + 3H2O	18.99		llnl	
YbF3:0.5H2O	YbF3:0.5H2O = Yb+3 + 3F- + 0.5H2O	-16.00		llnl	
YbCl3:6H2O	YbCl3:6H2O = Yb+3 + 3Cl- + 6H2O	5.53		llnl	Wagman et al 1982
Yb2(CO3)3	Yb2(CO3)3 + 3H+ = 2Yb+3 + 3HCO3-	-2.31		llnl	
YbPO4:10H2O	YbPO4:10H2O +H+ = Yb+3 + HPO4-2 + 10H2O	-11.78		llnl	
Lu2O3	Lu2O3 + 6H+ = 2Lu+3 + 3H2O	45.00		llnl	Wagman et al 1982
Lu(OH)3(s)	Lu(OH)3 + 3H+ = Lu+3 + 3H2O	14.49		llnl	
Lu(OH)3(a)	Lu(OH)3 + 3H+ = Lu+3 + 3H2O	18.99		llnl	
LuF3:0.5H2O	LuF3:0.5H2O = Lu+3 + 3F- + 0.5H2O	-15.90		llnl	

LuCl3:6H2O	LuCl3:6H2O = Lu+3 + 3Cl- + 6H2O	12.71		llnl	Wagman et al 1982
Lu2(CO3)3	Lu2(CO3)3 + 3H+ = 2Lu+3 + 3HCO3-	-2.01		llnl	
LuPO4:10H2O	LuPO4:10H2O +H+ = Lu+3 + HPO4-2 + 10H2O	-11.68		llnl	

Thermodynamic data not used in PHREEQC model

Y2(CO3)3	Y2(CO3)3 + 3H+ = 2Y+3 + 3HCO3-	0.00	n/a	Wagman et al 1982	
La2(CO3)3	La2(CO3)3 + 3H+ = 2La+3 + 3HCO3-	-2.43	n/a	Wagman et al 1982	
La2(CO3)3:8H2O	La2(CO3)3:8H2O + 3H+ = 2La+3 + 3HCO3- + 8H2O	-4.31	-416.09	llnl	
Ce3(PO4)4	Ce3(PO4)4 + 4H+ = 3Ce+4 + 4HPO4-2	-40.81	-217.17	llnl	
Eu3O4	Eu3O4 + 8H+ = Eu+2 + 2Eu+3 + 4H2O	87.04	-392.39	llnl	llnl
EuO	EuO + 2H+ = Eu+2 + 2H2O	37.48	n/a	llnl	llnl
EuCl2	EuCl2 = Eu+2 + 2Cl-	5.92	n/a	llnl	llnl
Eu(IO3)	Eu(IO3)3:2H2O = Eu+3 + 3IO3- + 2H2O	-11.70	n/a	llnl	llnl
EuS	EuS + 1H+ = Eu+2 + HS-	14.91	n/a	llnl	llnl
EuSO4	EuSO4 = Eu+2 + SO4-2	-8.84	-47.44	llnl	llnl

Appendix table 6 REE surface complexation thermodyanmic data compiled for this study.

HFO_w sites			HFO_s sites		
LFER: log_ks = -4.374 + logKMOH * 1.166			LFER: log_kw = -7.893 + logKMOH * 1.299		
Equation	**log k**	**Source**	**Equation**	**log k**	**Source**
Protonation					
Hfo_sOH + H+ = Hfo_sOH2+	7.29	Dzombak and Morel, 1990	Hfo_wOH + H+ = Hfo_wOH2+	7.29	Dzombak and Morel, 1990
Hfo_sOH = Hfo_sO- + H+	-8.93	Dzombak and Morel, 1990	Hfo_wOH = Hfo_wO- + H+	-8.93	Dzombak and Morel, 1990
REE + Y + Sc					
Hfo_sOH + La+3 = Hfo_sOLa+2 + H+	1.68	LFER calculation from Dzombak and Morel, 1990	Hfo_wOH + La+3 = Hfo_wOLa+2 + H+	-1.15	LFER calculation from Dzombak and Morel, 1990
Hfo_sOH + Ce+3 = Hfo_sOCe+2 + H+	2.22	LFER calculation from Dzombak and Morel, 1990	Hfo_wOH + Ce+3 = Hfo_wOCe+2 + H+	-0.54	LFER calculation from Dzombak and Morel, 1990
Hfo_sOH + Pr+3 = Hfo_sOPr+2 + H+	2.23	LFER calculation from Dzombak and Morel, 1990	Hfo_wOH + Pr+3 = Hfo_wOPr+2 + H+	-0.53	LFER calculation from Dzombak and Morel, 1990
Hfo_sOH + Nd+3 = Hfo_sONd+2 + H+	2.41	LFER calculation from Dzombak and Morel, 1990	Hfo_wOH + Nd+3 = Hfo_wONd+2 + H+	-0.34	LFER calculation from Dzombak and Morel, 1990
Hfo_sOH + Sm+3 = Hfo_sOSm+2 + H+	2.81	LFER calculation from Dzombak and Morel, 1990	Hfo_wOH + Sm+3 = Hfo_wOSm+2 + H+	0.10	LFER calculation from Dzombak and Morel, 1990
Hfo_sOH + Eu+3 = Hfo_sOEu+2 + H+	2.86	LFER calculation from Dzombak and Morel, 1990	Hfo_wOH + Eu+3 = Hfo_wOEu+2 + H+	0.16	LFER calculation from Dzombak and Morel, 1990
Hfo_sOH + Gd+3 = Hfo_sOGd+2 + H+	2.82	LFER calculation from Dzombak and Morel, 1990	Hfo_wOH + Gd+3 = Hfo_wOGd+2 + H+	0.12	LFER calculation from Dzombak and Morel, 1990
Hfo_sOH + Tb+3 = Hfo_sOTb+2 + H+	3.04	LFER calculation from Dzombak and Morel, 1990	Hfo_wOH + Tb+3 = Hfo_wOTb+2 + H+	0.37	LFER calculation from Dzombak and Morel, 1990
Hfo_sOH + Dy+3 = Hfo_sODy+2 + H+	3.10	LFER calculation from Dzombak and Morel, 1990	Hfo_wOH + Dy+3 = Hfo_wODy+2 + H+	0.43	LFER calculation from Dzombak and Morel, 1990
Hfo_sOH + Ho+3 = Hfo_sOHo+2 + H+	3.14	LFER calculation from Dzombak and Morel, 1990	Hfo_wOH + Ho+3 = Hfo_wOHo+2 + H+	0.47	LFER calculation from Dzombak and Morel, 1990
Hfo_sOH + Er+3 = Hfo_sOEr+2 + H+	3.18	LFER calculation from Dzombak and Morel, 1990	Hfo_wOH + Er+3 = Hfo_wOEr+2 + H+	0.52	LFER calculation from Dzombak and Morel, 1990
Hfo_sOH + Tm+3 = Hfo_sOTm+2 + H+	3.33	LFER calculation from Dzombak and Morel, 1990	Hfo_wOH + Tm+3 = Hfo_wOTm+2 + H+	0.69	LFER calculation from Dzombak and Morel, 1990
Hfo_sOH + Yb+3 = Hfo_sOYb+2 + H+	3.51	LFER calculation from Dzombak and Morel, 1990	Hfo_wOH + Yb+3 = Hfo_wOYb+2 + H+	0.89	LFER calculation from Dzombak and Morel, 1990
Hfo_sOH + Lu+3 = Hfo_sOLu+2 + H+	3.47	LFER calculation from Dzombak and Morel, 1990	Hfo_wOH + Lu+3 = Hfo_wOLu+2 + H+	0.85	LFER calculation from Dzombak and Morel, 1990
Hfo_sOH + Y+3 = Hfo_sOY+2 + H+	2.97	LFER calculation from Dzombak and Morel, 1990	Hfo_wOH + Y+3 = Hfo_wOY+2 + H+	0.29	LFER calculation from Dzombak and Morel, 1990

HMO_x sites			HMO_y sites		
Equation	**log k**	**Source**	**Equation**	**log k**	**Source**
Hmo_xOH + H+ = Hmo_xOH2+	2.35	Tonkin et al., 2004	Hmo_yOH + H+ = Hmo_yOH2+	2.35	Tonkin et al., 2004
Hmo_xOH = Hmo_xO- + H+	-6.06	Tonkin et al., 2004	Hmo_yOH = Hmo_yO- + H+	-6.06	Tonkin et al., 2004
Hmo_xOH + La+3 = Hmo_xOLa+2 + H+	-0.47	Porret and Davranche, 2013	Hmo_yOH + La+3 = Hmo_yOLa+2 + H+	2.50	Porret and Davranche, 2013
Hmo_xOH + Ce+3 = Hmo_xOCe+2 + H+	1.02	Porret and Davranche, 2013	Hmo_yOH + Ce+3 = Hmo_yOCe+2 + H+	3.73	Porret and Davranche, 2013
Hmo_xOH + Pr+3 = Hmo_xOPr+2 + H+	-0.15	Porret and Davranche, 2013	Hmo_yOH + Pr+3 = Hmo_yOPr+2 + H+	2.51	Porret and Davranche, 2013
Hmo_xOH + Nd+3 = Hmo_xONd+2 + H+	-0.33	Porret and Davranche, 2013	Hmo_yOH + Nd+3 = Hmo_yONd+2 + H+	2.70	Porret and Davranche, 2013
Hmo_xOH + Sm+3 = Hmo_xOSm+2 + H+	-0.24	Porret and Davranche, 2013	Hmo_yOH + Sm+3 = Hmo_yOSm+2 + H+	2.70	Porret and Davranche, 2013
Hmo_xOH + Eu+3 = Hmo_xOEu+2 + H+	-0.37	Porret and Davranche, 2013	Hmo_yOH + Eu+3 = Hmo_yOEu+2 + H+	2.65	Porret and Davranche, 2013
Hmo_xOH + Gd+3 = Hmo_xOGd+2 + H+	-0.73	Porret and Davranche, 2013	Hmo_yOH + Gd+3 = Hmo_yOGd+2 + H+	2.58	Porret and Davranche, 2013
Hmo_xOH + Tb+3 = Hmo_xOTb+2 + H+	-2.35	Porret and Davranche, 2013	Hmo_yOH + Tb+3 = Hmo_yOTb+2 + H+	2.69	Porret and Davranche, 2013
Hmo_xOH + Dy+3 = Hmo_xODy+2 + H+	-2.51	Porret and Davranche, 2013	Hmo_yOH + Dy+3 = Hmo_yODy+2 + H+	2.67	Porret and Davranche, 2013
Hmo_xOH + Ho+3 = Hmo_xOHo+2 + H+	-2.37	Porret and Davranche, 2013	Hmo_yOH + Ho+3 = Hmo_yOHo+2 + H+	2.49	Porret and Davranche, 2013
Hmo_xOH + Er+3 = Hmo_xOEr+2 + H+	-1.79	Porret and Davranche, 2013	Hmo_yOH + Er+3 = Hmo_yOEr+2 + H+	2.61	Porret and Davranche, 2013
Hmo_xOH + Tm+3 = Hmo_xOTm+2 + H+	-1.55	Porret and Davranche, 2013	Hmo_yOH + Tm+3 = Hmo_yOTm+2 + H+	2.45	Porret and Davranche, 2013
Hmo_xOH + Yb+3 = Hmo_xOYb+2 + H+	-3.86	Porret and Davranche, 2013	Hmo_yOH + Yb+3 = Hmo_yOYb+2 + H+	2.69	Porret and Davranche, 2013

Hmo_xOH + Lu+3 = Hmo_xOLu+2 + H+	-1.49	Porret and Davranche, 2013	Hmo_yOH + Lu+3 = Hmo_yOLu+2 + H+	2.61	Porret and Davranche, 2013
Hmo_xOH + Y+3 = Hmo_xOY+2 + H+	-1.54	average of Gd and Tb	Hmo_yOH + Y+3 = Hmo_yOY+2 + H+	2.64	average of Gd and Tb
	HAO sites			**HAO sites**	
LFER: log_k = -9.19 + logKMOH * 1.32					
Equation	**log k**	**Source**	**Equation**	**log k**	**Source**
Hao_OH + H+ = Hao_OH2+	7.17	Karamalidis and Dzombak, 2010			
Hao_OH = Hao_O- + H+	-11	Karamalidis and Dzombak, 2010			
Hao_OH + La+3 = Hao_OLa+2 + H+	-2.3	LFER calculation from Karamalidis and Dzombak, 2010	Hao_OH + La(SO4)+ = Hao_OLa(SO4) + H+	-2.95	Lozano et al., 2019
Hao_OH + Ce+3 = Hao_OCe+2 + H+	-1.7	LFER calculation from Karamalidis and Dzombak, 2010	Hao_OH + Ce(SO4)+ = Hao_OCe(SO4) + H+	-2.81	Lozano et al., 2019
Hao_OH + Pr+3 = Hao_OPr+2 + H+	-1.7	LFER calculation from Karamalidis and Dzombak, 2010	Hao_OH + Pr(SO4)+ = Hao_OPr(SO4) + H+	-2.69	Lozano et al., 2019
Hao_OH + Nd+3 = Hao_ONd+2 + H+	-1.5	LFER calculation from Karamalidis and Dzombak, 2010	Hao_OH + Nd(SO4)+ = Hao_ONd(SO4) + H+	-2.60	Lozano et al., 2019
Hao_OH + Sm+3 = Hao_OSm+2 + H+	-1.1	LFER calculation from Karamalidis and Dzombak, 2010	Hao_OH + Sm(SO4)+ = Hao_OSm(SO4) + H+	-2.48	Lozano et al., 2019
Hao_OH + Eu+3 = Hao_OEu+2 + H+	-1	LFER calculation from Karamalidis and Dzombak, 2010	Hao_OH + Eu(SO4)+ = Hao_OEu(SO4) + H+	-2.50	Lozano et al., 2019
Hao_OH + Gd+3 = Hao_OGd+2 + H+	-1.1	LFER calculation from Karamalidis and Dzombak, 2010	Hao_OH + Gd(SO4)+ = Hao_OGd(SO4) + H+	-2.50	Lozano et al., 2019
Hao_OH + Tb+3 = Hao_OTb+2 + H+	-0.8	LFER calculation from Karamalidis and Dzombak, 2010	Hao_OH + Tb(SO4)+ = Hao_OTb(SO4) + H+	-2.48	Lozano et al., 2019
Hao_OH + Dy+3 = Hao_ODy+2 + H+	-0.7	LFER calculation from Karamalidis and Dzombak, 2010	Hao_OH + Dy(SO4)+ = Hao_ODy(SO4) + H+	-2.37	Lozano et al., 2019
Hao_OH + Ho+3 = Hao_OHo+2 + H+	-0.7	LFER calculation from Karamalidis and Dzombak, 2010	Hao_OH + Ho(SO4)+ = Hao_OHo(SO4) + H+	-2.40	Lozano et al., 2019
Hao_OH + Er+3 = Hao_OEr+2 + H+	-0.6	LFER calculation from Karamalidis and Dzombak, 2010	Hao_OH + Er(SO4)+ = Hao_OEr(SO4) + H+	-2.40	Lozano et al., 2019
Hao_OH + Tm+3 = Hao_OTm+2 + H+	-0.5	LFER calculation from Karamalidis and Dzombak, 2010	Hao_OH + Tm(SO4)+ = Hao_OTm(SO4) + H+	-2.27	Lozano et al., 2019
Hao_OH + Yb+3 = Hao_OYb+2 + H+	-0.3	LFER calculation from Karamalidis and Dzombak, 2010	Hao_OH + Yb(SO4)+ = Hao_OYb(SO4) + H+	-2.13	Lozano et al., 2019
Hao_OH + Lu+3 = Hao_OLu+2 + H+	-0.3	LFER calculation from Karamalidis and Dzombak, 2010	Hao_OH + Lu(SO4)+ = Hao_OLu(SO4) + H+	-2.19	Lozano et al., 2019
Hao_OH + Y+3 = Hao_OY+2 + H+	-0.9	LFER calculation from Karamalidis and Dzombak, 2010	Hao_OH + Y(SO4)+ = Hao_OY(SO4) + H+	-2.48	Lozano et al., 2019

Appendix table 7 HFO, HMO, HAO surface characteristics used for this study. HFO strong and weak site densities are the highest values reported in Dzombak and Morel, 1990.

HFO	**Dzombak and Morel, 1990**	
Surface area	600	m2/g Fe(OH)3
Strong sites density	0.010	mol/mol Fe(OH)3
Weak sites density	0.910	mol/mol Fe(OH)3
HMO	**Tonkin et al., 2004**	
Surface area	746	m2/g MnO2
X sites desnsity	0.074	mol/mol MnO2
Y sites density	0.042	mol/mol MnO2
HAO	**Karamalidis and Dzombak, 2010**	
Surface area	32	m2/g Al(OH)3
Site density	0.033	mol/mol Al(OH)3

Appendix table 8 Linear combination fitting of bulk Ce XANES using different combinations of standards. LCF was conducted on normalized μ(E) data with a fit range of -20eV to +60eV from the Ce edge identified in preprocessing steps. Component sums were not constrained to 100%. R-factor = sum((data-fit)^2)/sum(data^2). The best fit (lowest R-factor) is bolded.

Sample	**Component 1**	**Weight**	**Error**	**Component 2**	**Weight**	**Error**	**Sum**	**R-factor**	**Ce valence**
Scootac Al	Ce(III)SO4	0.834	0.022	Ce(IV)O2	0.214	0.023	1.048	0.0829	3.20
Scootac Al	Ce(III)SO4	0.854	0.019	Ce(IV)SO4	0.209	0.020	1.063	0.0793	3.20
Scootac Al	**Ce(III)Cl**	**0.692**	**0.014**	**Ce(IV)SO4**	**0.308**	**0.017**	**1.000**	**0.0695**	**3.31**
Scootac Al	Ce(III)Cl	0.659	0.016	Ce(IV)O2	0.324	0.018	0.983	0.0716	3.33
Scootac Al	Ce(III)CO3	0.877	0.019	Ce(IV)SO4	0.251	0.019	1.128	0.0807	3.22
Woodlands	Ce(III)SO4	0.617	0.018	Ce(IV)O2	0.411	0.018	1.028	0.0645	3.40
Woodlands	Ce(III)SO4	0.669	0.014	Ce(IV)SO4	0.385	0.016	1.054	0.0578	3.37
Woodlands	**Ce(III)Cl**	**0.541**	**0.011**	**Ce(IV)SO4**	**0.463**	**0.013**	**1.004**	**0.0523**	**3.46**
Woodlands	Ce(III)Cl	0.489	0.013	Ce(IV)O2	0.491	0.015	0.980	0.0552	3.50
Woodlands	Ce(III)CO3	0.687	0.015	Ce(IV)SO4	0.418	0.015	1.105	0.0595	3.38
Scootac Mn	Ce(III)SO4	0.077	0.010	Ce(IV)O2	0.908	0.011	0.985	0.0266	3.92
Scootac Mn	**Ce(III)SO4**	**0.209**	**0.008**	**Ce(IV)SO4**	**0.830**	**0.008**	**1.039**	**0.0204**	**3.80**
Scootac Mn	Ce(III)Cl	0.166	0.006	Ce(IV)SO4	0.857	0.008	1.023	0.0209	3.84
Scootac Mn	Ce(III)Cl	0.067	0.008	Ce(IV)O2	0.912	0.009	0.979	0.0254	3.93

Scootac Mn	Ce(III)CO3	0.214	0.008	Ce(IV)SO4	0.840	0.008	1.054	0.0213	3.80
Westbox	Ce(III)SO4	0.000	0.000	Ce(IV)O2	1.000	0.000	1.000	0.0431	4.00
Westbox	**Ce(III)SO4**	**0.019**	**0.007**	**Ce(IV)SO4**	**0.979**	**0.007**	**0.998**	**0.0166**	**3.98**
Westbox	Ce(III)Cl	0.010	0.006	Ce(IV)SO4	0.986	0.007	0.996	0.0168	3.99
Westbox	Ce(III)Cl	0.000	0.000	Ce(IV)O2	1.000	0.000	1.000	0.0431	4.00
Westbox	Ce(III)CO3	0.019	0.007	Ce(IV)SO4	0.980	0.007	0.999	0.0174	3.98
Birnessite + CeCl3	Ce(III)SO4	0.000	0.008	Ce(IV)O2	0.884	0.008	0.884	0.0219	4.00
Birnessite + CeCl3	Ce(III)SO4	0.109	0.012	Ce(IV)SO4	0.814	0.013	0.923	0.0686	3.88
Birnessite + CeCl3	Ce(III)Cl	0.072	0.010	Ce(IV)SO4	0.843	0.012	0.915	0.0746	3.92
Birnessite + CeCl3	**Ce(III)Cl**	**0.000**	**0.006**	**Ce(IV)O2**	**0.883**	**0.007**	**0.883**	**0.0218**	**4.00**
Birnessite + CeCl3	Ce(III)CO3	0.111	0.012	Ce(IV)SO4	0.820	0.012	0.931	0.0688	3.88
Ferrihydrite + CeCl3	Ce(III)SO4	0.407	0.010	Ce(IV)O2	0.628	0.010	1.035	0.0235	3.61
Ferrihydrite + CeCl3	Ce(III)SO4	0.499	0.008	Ce(IV)SO4	0.573	0.009	1.072	0.0212	3.53
Ferrihydrite + CeCl3	Ce(III)Cl	0.397	0.007	Ce(IV)SO4	0.638	0.009	1.035	0.0258	3.62
Ferrihydrite + CeCl3	Ce(III)Cl	0.319	0.007	Ce(IV)O2	0.684	0.008	1.003	0.0219	3.68
Ferrihydrite + CeCl3	**Ce(III)CO3**	**0.512**	**0.008**	**Ce(IV)SO4**	**0.598**	**0.008**	**1.110**	**0.0205**	**3.54**
Boehmite + CeCl3	Ce(III)SO4	0.725	0.013	Ce(IV)O2	0.252	0.013	0.977	0.0387	3.26
Boehmite + CeCl3	Ce(III)SO4	0.760	0.011	Ce(IV)SO4	0.232	0.012	0.992	0.0375	3.23
Boehmite + CeCl3	Ce(III)Cl	0.607	0.009	Ce(IV)SO4	0.329	0.011	0.936	0.0422	3.35
Boehmite + CeCl3	Ce(III)Cl	0.565	0.010	Ce(IV)O2	0.356	0.012	0.921	0.0389	3.39
Boehmite + CeCl3	**Ce(III)CO3**	**0.780**	**0.011**	**Ce(IV)SO4**	**0.270**	**0.011**	**1.050**	**0.0368**	**3.26**

Appendix table 9 Mn μ-XANES summary. Mn(II), Mn(III), and Mn(IV) fractions are calculated using linear combination fitting with Mn(II)O, $Mn(III)_2O_3$, and $Mn(IV)O_2$ as endmembers. Parentheses are software generated errors.

Sample	Type	Mn(II) weight	Mn(III) weight	Mn(IV) weight)	Sum	R-factor	Average valence
Scootac Mn	μ-XANES, Mn1	0.000 (0.017)	0.000 (0.039)	0.995 (0.027)	1.00	0.01	4.00
Scootac Mn	μ-XANES, Mn2	0.000 (0.038)	0.011 (0.086)	0.994 (0.069)	1.01	0.04	3.99
Scootac Mn	μ-XANES, Mn3	0.000 (0.035)	0.011 (0.050)	0.994 (0.035)	1.01	0.02	3.99
Westbox	μ-XANES, Mn2	0.039 (0.019)	0.123 (0.043)	0.765 (0.029)	0.93	0.01	3.78
Westbox	μ-XANES, Mn3	0.045 (0.019)	0.182 (0.042)	0.694 (0.029)	0.92	0.01	3.70

Appendix table 10 Ce bulk and μ-XANES summary. Ce(III) and Ce(IV) fractions are calculated using linear combination fitting with $Ce(III)Cl_3$ and $Ce(IV)(SO_4)_2$ as endmembers. Parentheses are software generated errors. † no error generated.

Sample	Type	Ce(III) weight	Ce(IV) weight	Sum	R-factor	Average valence
Scootac Mn	Bulk XANES	0.209 (0.008)	0.830 (0.008)	1.04	0.02	3.80
Scootac Mn	μ-XANES, Ce1	0.105 (0.022)	0.980 (0.022)	1.08	0.08	3.90
Scootac Mn	μ-XANES, Ce2	0.018 (0.020)	0.960 (0.020)	0.98	0.10	3.98
Scootac Mn	μ-XANES, Ce3	0.069 (0.020)	0.930 (0.020)	1.00	0.09	3.93
Scootac Mn	μ-XANES, Ce4	0.121 (0.019)	0.980 (0.019)	1.10	0.06	3.89
Westbox	Bulk XANES	0.019 (0.007)	0.979 (0.007)	1.00	0.02	3.98
Westbox	μ-XANES, Ce2	0.260 (0.010)	0.790 (0.009)	1.05	0.02	3.75
Westbox	μ-XANES, Ce3a	0.400 (0.009)	0.646 (0.008)	1.05	0.01	3.62
Westbox	μ-XANES, Ce3b	0.234 (0.014)	0.764 (0.013)	1.00	0.04	3.77
Westbox	μ-XANES, Ce4	0.242 (0.016)	0.840 (0.015)	1.08	0.03	3.78
Westbox	μ-XANES, Ce5	0.170 (0.021)	0.840 (0.020)	1.01	0.08	3.83
Westbox	μ-XANES, Ce6	0.160 (0.011)	0.895 (0.011)	1.06	0.02	3.85
Westbox	μ-XANES, Ce7	0.354 (0.008)	0.706 (0.007)	1.06	0.01	3.67
Westbox	μ-XANES, Ce8	0.125 (0.019)	0.834 (0.018)	0.96	0.07	3.87
Scootac Al	Bulk XANES	0.692 (0.014)	0.308 (0.017)	1.00	0.07	3.31
Scootac Al	μ-XANES, Ce2	1.000†	0.182†	1.18	0.06	3.15
Scootac Al	μ-XANES, Ce3	1.000†	0.096†	1.10	0.06	3.09
Scootac Al	μ-XANES, Ce7	1.000†	0.102†	1.10	0.05	3.09
Woodlands	Bulk XANES	0.541 (0.011)	0.463 (0.013)	1.00	0.05	3.46
Woodlands	μ-XANES, Ce2	1.000†	0.103†	1.10	0.11	3.09
Woodlands	μ-XANES, Ce4	1.000†	0.382†	1.38	0.19	3.28
Woodlands	μ-XANES, Ce5	1.000†	0.308†	1.31	0.23	3.24
Woodlands	μ-XANES, Ce8	1.000†	0.226†	1.23	0.16	3.18

Appendix table 11 Measured and modeled Ca concentrations at the influent and effluent of the treatment systems modeled in this study.

	Westbox		Scootac		Woodlands	
	pH	Ca (mg/L)	pH	Ca (mg/L)	pH	Ca (mg/L)
Influent (measured)	2.95	44.3	3.91	90.5	3.27	105.5
Effluent (measured)	7.30	147.5	6.98	193.0	6.62	252.0
Modeled	7.25	153.5	7.00	203.5	6.50	204.4

Appendix D: All influent and effluent chemistry data from samples collected for chapter 2

Data are available at: http://d-scholarship.pitt.edu/40198/3/Hedin%202021%20Dissertation%20Attached%20Tables.xlsx.

Appendix E: All treatment solids geochemistry data for treatment solids samples collected for chapter 2

Data are available at: http://d-scholarship.pitt.edu/40198/3/Hedin%202021%20Dissertation%20Attached%20Tables.xlsx.

Appendix F: Dissolved Y and TDS data from liquid samples, and treatment solids Y concentration data for calculating solids concentration factors for chapter 2

Data are available at: http://d-scholarship.pitt.edu/40198/3/Hedin%202021%20Dissertation%20Attached%20Tables.xlsx.

Appendix G: All solids and water data collected in chapter 3

Data are available at: http://d-scholarship.pitt.edu/40198/3/Hedin%202021%20Dissertation%20Attached%20Tables.xlsx.

Bibliography

Acero, P., Ayora, C., Torrentó, C., & Nieto, J.-M. (2006). The behavior of trace elements during schwertmannite precipitation and subsequent transformation into goethite and jarosite. *Geochimica et Cosmochimica Acta, 70*(16), 4130-4139. doi:10.1016/j.gca.2006.06.1367

Actlabs. (2018). Methods. Retrieved from http://www.actlabs.com/list.aspx?menu=64&app=226&cat1=549&tp=12&lk=no

Alonso, E., Sherman, A. M., Wallington, T. J., Everson, M. P., Field, F. R., Roth, R., & Kirchain, R. E. (2012). Evaluating rare earth element availability: a case with revolutionary demand from clean technologies. *Environ Sci Technol, 46*(6), 3406-3414. doi:10.1021/es203518d

Ault, T., Krahn, S., & Croff, A. (2015). Radiological Impacts and Regulation of Rare Earth Elements in Non-Nuclear Energy Production. *Energies, 8*(3), 2066-2081. doi:10.3390/en8032066

Ayora, C., Macias, F., Torres, E., Lozano, A., Carrero, S., Nieto, J. M., . . . Castillo-Michel, H. (2016). Recovery of Rare Earth Elements and Yttrium from Passive-Remediation Systems of Acid Mine Drainage. *Environ Sci Technol, 50*(15), 8255-8262. doi:10.1021/acs.est.6b02084

Bao, Z., & Zhao, Z. (2008). Geochemistry of mineralization with exchangeable REY in the weathering crusts of granitic rocks in South China. *Ore Geology Reviews, 33*(3-4), 519-535. doi:10.1016/j.oregeorev.2007.03.005

Bau, M. (1999). Scavenging of dissolved yttrium and rare earths by precipitating iron oxyhydroxide: Experimental evidence for Ce oxidation, Y-Ho fractionation, and lanthanide tetrad effect. *Geochemica et Cosmochimica Acta, 63*(1), 66-77.

Bau, M., & Koschinsky, A. (2009). Oxidative scavenging of cerium of hydrous Fe oxide: Evidence from the distribution of rare earth elements and yttrium between Fe oxides and Mn oxides in hydrogenetic ferromanganese crusts. *Geochemical Journal, 43*, 37-47.

Bau, M., Koschinsky, A., Dulski, P., & Hein, J. (1996a). Comparison of the partitioning behaviors of yttrium, rare earth elemtns, and titanium between hydrogenetic marine ferromanganese crusts and seawater. *Geochemica et Cosmochimica Acta, 60*(10), 1709-1725.

Bau, M., Koschinsky, A., Dulski, P., & Hein, J. (1996b). Comparison of the partitioning behaviours of yttrium, rare earth elements, and titanium between hydrogenetic marine ferromanganese crusts and seawater. *Geochemica et Cosmochimica Acta, 60*(10), 1709-1725.

Bau, M., Schmidt, K., Koschinsky, A., Hein, J., Kuhn, T., & Usui, A. (2014). Discriminating between different genetic types of marine ferro-manganese crusts and nodules based on rare earth elements and yttrium. *Chemical Geology, 381*, 1-9. doi:10.1016/j.chemgeo.2014.05.004

Beam, R. L. (2019, March 26, 2019). *Overview of acitive mine drainage treatment facilities currently operated by the PA-DEP bureau of abandoned mine reclamation.* Paper presented at the West Virginia Mine Drainage Task Force Symposium, Morgantown, WV.

Berger, V. I., Singer, D. A., Bliss, J. D., & Moring, B. C. (2011). Ni-Co laterite deposits of the world - database and grade and tonnage models. *U.S. Geological Survey Open-File Report 2011-1058*, 1-30.

Bigham, J. M., & Nordstrom, D. K. (2000). Iron and Aluminum Hydroxysulfates from Acid Sulfate Waters. *Reviews in Mineralogy and Geochemistry, 40*(1), 351-403. doi:10.2138/rmg.2000.40.7

Bigham, J. M., Schwertmann, U., Traina, S. J., Winland, R. L., & Wolf, M. (1996). Schwertmannite and the chemical modeling of iron in acid sulfate waters. *Geochemica et Cosmochimica Acta, 60*(12), 2111-2121.

Binnemans, K., Jones, P. T., Blanpain, B., Van Gerven, T., Yang, Y., Walton, A., & Buchert, M. (2013). Recycling of rare earths: a critical review. *Journal of Cleaner Production, 51*, 1-22. doi:10.1016/j.jclepro.2012.12.037

Bosoaga, A., Masek, O., & Oakey, J. E. (2009). CO2 Capture Technologies for Cement Industry. *Energy Procedia, 1*(1), 133-140. doi:10.1016/j.egypro.2009.01.020

Brookins, D. G. (1983). Eh-pH diagrams for the rare earth elements at 25C and one Bar pressure. *Geochemical Journal, 17*, 223-229.

Burns, R. G. (1976). The uptake of cobalt into ferromanganese nodules, soils, and synthetic manganese (IV) oxides. *Geochemica et Cosmochimica Acta, 40*(1), 95-102.

Callura, J. C., Perkins, K. M., Noack, C. W., Washburn, N. R., Dzombak, D. A., & Karamalidis, A. K. (2018). Selective adsorption of rare earth elements onto functionalized silica particles. *Green Chemistry, 20*(7), 1515-1526. doi:10.1039/c8gc00051d

Cannon, W. F., Kimball, B. E., & Corathers, L. A. (2018). Manganese, Chapter L of Critical Metal Resources of the United States - Economic and Environmental Geology and Prospects for Future Supple. *U.S. Geological Survey Professional Paper 1802*, L1-L28.

Cao, X., Chen, Y., Wang, X., & Deng, X. (2001). Effects of redox potential and pH value on the release of rare earth elements from soil. *Chemosphere, 44*(4), 655-661.

Caraballo, M. A., Rötting, T. S., Macías, F., Nieto, J. M., & Ayora, C. (2009). Field multi-step limestone and MgO passive system to treat acid mine drainage with high metal

concentrations. *Applied Geochemistry*, *24*(12), 2301-2311. doi:10.1016/j.apgeochem.2009.09.007

Castor, S., B. (2008). The Mountain Pass Rare-Earth Carbonatite and Associated Ultrapotassic Rocks, California. *The Canadian Mineralogist, 46*, 779-806. doi:10.3749/canmin.46.4.779

Cavazza, E. C., & Beam, R. L. (2010). *Restoring the Bennett Branch Sinnemahoning Creek, Clearfield and Elk Counties, Pennsylvania*. Paper presented at the 2010 National Meeting of the American Society of Mining and Reclamation, Pittsburgh, PA, USA.

Chen, L. H., M. L., Fabian-Wheeler, E. E., Xu, Z., Bruns, M. A., Brown, V. (2018). Iron Oxide to Mitigate Hydrogen Sulfide Gas Release from Gypsum-Bedded Dairy Manure Storages. *American Society of Agricultural and Biological Engineers, 61*(3), 1101-1112.

Cornell, R. M., & Schwertmann, U. (2003). *The Iron Oxides: Structure, Properties, Reactions, Occurences and Uses*. Weinheim, Germany: Wiley-VCH.

Cravotta, C. A. (2008a). Dissolved metals and associated constituents in abandoned coal-mine discharges, Pennsylvania, USA. Part 1: Constituent quantities and correlations. *Applied Geochemistry, 23*(2), 166-202. doi:10.1016/j.apgeochem.2007.10.011

Cravotta, C. A. (2008b). Dissolved metals and associated constituents in abandoned coal-mine discharges, Pennsylvania, USA. Part 2: Geochemical controls on constituent concentrations. *Applied Geochemistry, 23*, 203-226. doi:10.1016/j.apgeochem.2007.10.003

Cravotta, C. A. (2020). Interactive PHREEQ-N-AMDTreat water-quality modeling tools to evaluate performance and design of treatment systems for acid mine drainage. *Applied Geochemistry*. doi:10.1016/j.apgeochem.2020.104845

Cravotta, C. A., & Brady, K. B. C. (2015). Priority pollutants and associated constituents in untreated and treated discharges from coal mining or processing facilities in Pennsylvania, USA. *Applied Geochemistry, 62*, 108-130. doi:10.1016/j.apgeochem.2015.03.001

Cravotta, C. A., Means, B. P., Arthur, W., McKenzie, R. M., & Parkhurst, D. L. (2014). AMDTreat 5.0+ with PHREEQC Titration Module to Compute Caustic Chemical Quantity, Effluent Quality, and Sludge Volume. *Mine Water and the Environment, 34*(2), 136-152. doi:10.1007/s10230-014-0292-6

Cravotta, C. A., & Trahan, M. K. (1999). Limestone drains to increase pH and remove dissolved metals from acidic mine drainage. *Applied Geochemistry, 14*, 581-606.

Dai, S., & Finkelman, R. B. (2018). Coal as a promising source of critical elements: Progress and future prospects. *International Journal of Coal Geology, 186*, 155-164. doi:10.1016/j.coal.2017.06.005

Dai, S., Li, D., Chou, C.-L., Zhao, L., Zhang, Y., Ren, D., . . . Sun, Y. (2008). Mineralogy and geochemistry of boehmite-rich coals: New insights from the Haerwusu Surface Mine,

Jungar Coalfield, Inner Mongolia, China. *International Journal of Coal Geology, 74*(3-4), 185-202. doi:10.1016/j.coal.2008.01.001

Davranche, M., Pourret, O., Gruau, G., & Dia, A. (2004). Impact of humate complexation on the adsorption of REE onto Fe oxyhydroxide. *J Colloid Interface Sci, 277*(2), 271-279. doi:10.1016/j.jcis.2004.04.007

Davranche, M., Pourret, O., Gruau, G., Dia, A., Jin, D., & Gaertner, D. (2008). Competitive binding of REE to humic acid and manganese oxide: Impact of reaction kinetics on development of cerium anomaly and REE adsorption. *Chemical Geology, 247*, 154-170. doi:10.1016/j.chemgeo.2007.10.010

de Carlo, E. H., Wen, X.-Y., & Irving, M. (1998). The Influence of Redox Reactions on the Uptake of Dissolved Ce by Suspended Fe and Mn Oxide Particles. *Aquatic Geochemistry, 3*, 357-389.

De Carlo, E. H., Wen, X. Y., & Cowen, J. P. (2000). Rare Earth Element Fractionation in Hydrogenetic Fe-Mn Crusts: The Influence of Carbonate Complexation and Phosphatization on Sm/Yb Ratios. In *Marine Authigenesis: From Global to Microbial* (pp. 271-285).

DeSa, T. C., Brown, J. F., & Burgos, W. D. (2010). Laboratory and Field-scale Evaluation of Low-pH Fe(II) Oxidation at Hughes Borehole, Portage, Pennsylvania. *Mine Water and the Environment, 29*(4), 239-247. doi:10.1007/s10230-010-0105-5

Do, S. H., Batchelor, B., Lee, H. K., & Kong, S. H. (2009). Hydrogen peroxide decomposition on manganese oxide (pyrolusite): kinetics, intermediates, and mechanism. *Chemosphere, 75*(1), 8-12. doi:10.1016/j.chemosphere.2008.11.075

DOE. (2011). U.S. Department of Energy Critical Materials Strategy.

Dominish, E., Florin, N., & Teske, S. (2019). Responsible Minerals Sourcing for Renewable Energy. Report prepared for Earthworks by the Institute for Sustainable Futures.

Donovan, J. J., & Ziemkiewicz, P. F. (2013). Selenium Adsorption onto Iron Oxide Layers beneath Coal-Mine Overburden Spoil. *J Environ Qual, 42*(5), 1402-1411. doi:10.2134/jeq2012.0500

Du, X., & Graedel, T. E. (2011). Global in-use stocks of the rare Earth elements: a first estimate. *Environ Sci Technol, 45*(9), 4096-4101. doi:10.1021/es102836s

Dutta, T., Kim, K. H., Uchimiya, M., Kwon, E. E., Jeon, B. H., Deep, A., & Yun, S. T. (2016). Global demand for rare earth resources and strategies for green mining. *Environ Res, 150*, 182-190. doi:10.1016/j.envres.2016.05.052

Dzombak, D. A., & Morel, F. A. A. (1990). *Surface Complexation Modeling: Hydrous Ferric Oxide*: John Wiley & Sons.

EPA. (2015, March 3, 2017). 303(d) List Impaired Waters NHDPlus Indexed Dataset with Program Attributes. May 1, 2015. Retrieved from https://www.epa.gov/waterdata/waters-geospatial-data-downloads

Erickson, B. (2018, 7/9/2018). Rare-earth Recovery. *Chemical & Engineering News, 96*, 28-33.

Feng, X. H., Liu, F., Tan, W. F., & Liu, X. W. (2004). Synthesis of Birnessite from the Oxidation of Mn2+ by O2 in Alkali Medium: Effects of Synthesis Conditions. *Clays and Clay Minerals, 52*(2), 240-250. doi:10.1346/ccmn.2004.0520210

Finkelman, R. B. (1993). Trace and Minor Elements in Coal. In *Organic Geochemistry* (pp. 593-607).

Fishman, T., & Graedel, T. E. (2019). Impact of the establishment of US offshore wind power on neodymium flows. *Nature Sustainability, 2*(4), 332-338. doi:10.1038/s41893-019-0252-z

Foley, N. K., Jaskula, B. W., Kimball, B. A., & Schulte, R. F. (2017). Gallium, chapter H of Critical mineral resources of the United States - economic and environmental geology and prospects for future supply. *U.S. Geological Survey Professional Paper 1802*, H1-H35.

Fukuishi, K., Tsukimura, K., & Yamada, H. (2006). Surface Acidity of Amorphous Aluminum Hydroxide. *Acta Geologica Sinica, 80*(2), 206-211.

Gambogi, J. (2019a). U.S. Geological Survey, Mineral Commodity Summaries, February 2019, Rare Earths.

Gambogi, J. (2019b). U.S. Geological Survey, Mineral Commodity Summaries, February 2019, Yttrium.

Golden, D. C., Chen, C. C., & Dixon, J. B. (1987). Transformation of Birnessite to Buserite, Todorokite, and Manganite Under Mild Hydrothermal Treatment. *Clays and Clay Minerals, 35*(4), 271-280.

Goonan, T. G. (2014). The lifecycle of silver in the United States in 2009. *U.S. Geological Survey Scientific Investigations Report 2013-5178*, 1-17.

Gromet, L. P., Dymek, R. F., Haskin, L. A., & Korotev, R. L. (1984). The "North American shale composite": Its compilation, major and trace element characteristics. *Geochemica et Cosmochimica Acta, 48*, 2469-2482.

Gu, C., & Karthikeyan, K. G. (2005). Interaction of Tetracycline with Aluminum and Iron Hydrous Oxides. *Environmental Science and Technology, 39*, 2660-2667.

Hansel, C. M., Zeiner, C. A., Santelli, C. M., & Webb, S. M. (2012). Mn(II) oxidation by an ascomycete fungus is linked to superoxide production during asexual reproduction. *Proc Natl Acad Sci U S A, 109*(31), 12621-12625. doi:10.1073/pnas.1203885109

Haque, N., Hughes, A., Lim, S., & Vernon, C. (2014). Rare Earth Elements: Overview of Mining, Mineralogy, Uses, Sustainability and Environmental Impact. *Resources, 3*(4), 614-635. doi:10.3390/resources3040614

Haskin, M. A., & Haskin, L. A. (1966). Rare Earths in European Shales: A Redetermination. *Science, 154*, 507-509.

Hedin, B. C., Capo, R. C., Stewart, B. W., Hedin, R. S., Lopano, C. L., & Stuckman, M. Y. (2019a). The evaluation of critical rare earth element (REE) enriched treatment solids from coal mine drainage passive treatment systems. *International Journal of Coal Geology, 28*, 54-64. doi:10.1016/j.coal.2019.04.007

Hedin, B. C., Hedin, R. S., Capo, R. C., & Stewart, B. W. (2020a). Critical metal recovery potential of Appalachian acid mine drainage treatment solids. *International Journal of Coal Geology, 231*. doi:10.1016/j.coal.2020.103610

Hedin, B. C., Stuckman, M. Y., Lopano, C. L., & Capo, R. C. (2019b). *Characterization of Rare Earth Elements in Coal Mine Drainage Treatment Solids*. Paper presented at the 36th Annual Internation Pittsburgh Coal Conference, Pittsburgh, PA, USA.

Hedin Environmental. (2008). *Optimizing the Design and Operation of Self-flushing Limestone Systems for Mine Drainage Treatment*. Retrieved from http://files.dep.state.pa.us/Mining/Abandoned%20Mine%20Reclamation/AbandonedMinePortalFiles/InnovativeTechnologyGrantFinalReports/Flushing.pdf

Hedin, R., Hedin, B., Spargo, J. T., & Brimmer, R. (2020b). Characteristics of solids produced from coal mine drainage and their suitability for phosphorus control in dairy manure management. *J Environ Qual, 49*(6), 1502-1514. doi:10.1002/jeq2.20157

Hedin, R., Weaver, T., Wolfe, N., & Watzlaf, G. (2013). *Effective Passive Treatment of Coal Mine Drainage*. Paper presented at the 35th Annual National Association of Abandoned Mine Land Programs Conference, The Resort at Glade Springs, Daniels, West Virginia.

Hedin, R., Weaver, T., Wolfe, N., & Weaver, K. (2010). Passive Treatment of Acidic Coal Mine Drainage: The Anna S Mine Passive Treatment Complex. *Mine Water and the Environment, 29*(3), 165-175. doi:10.1007/s10230-010-0117-1

Hedin, R. S. (2003). Recovery of marketable iron oxide from mine drainage in the USA. *Land Contamination & Reclamation, 11*(2), 93-97. doi:10.2462/09670513.802

Hedin, R. S. (2008). Iron Removal by a Passive System Treating Alkaline Coal Mine Drainage. *Mine Water and the Environment, 27*(4), 200-209. doi:10.1007/s10230-008-0041-9

Hedin, R. S., Watzlaf, G. R., & Nairn, R. W. (1994). Passive Treatment of Acid Mine Drainage with Limestone. *Journal of Environmental Quality, 23*, 1338-1345.

Hein, J. R., Mizell, K., Koschinsky, A., & Conrad, T. A. (2013). Deep-ocean mineral deposits as a source of critical metals for high- and green-technology applications: Comparison with

land-based resources. *Ore Geology Reviews, 51*, 1-14. doi:10.1016/j.oregeorev.2012.12.001

Hudson-Edwards, K. A., Jamieson, H. E., & Lottermoser, B. G. (2011). Mine Wastes: Past, Present, Future. *Elements, 7*(6), 375-380. doi:10.2113/gselements.7.6.375

Kairies, C. L., Capo, R. C., & Watzlaf, G. R. (2005). Chemical and physical properties of iron hydroxide precipitates associated with passively treated coal mine drainage in the Bituminous Region of Pennsylvania and Maryland. *Applied Geochemistry, 20*(8), 1445-1460. doi:10.1016/j.apgeochem.2005.04.009

Karamalidis, A. K., & Dzombak, D. A. (2010). *Surface Complexation Modeling: Gibbsite*. Hoboken, New Jersey: John Wiley & Sons.

Koschinsky, A., Heinrich, L., Boehnke, K., Cohrs, J. C., Markus, T., Shani, M., . . . Werner, W. (2018). Deep-sea mining: Interdisciplinary research on potential environmental, legal, economic, and societal implications. *Integr Environ Assess Manag*. doi:10.1002/ieam.4071

Larson, L. N., Sánchez-España, J., & Burgos, W. (2014). Rates of low-pH biological Fe(II) oxidation in the Appalachian Bituminous Coal Basin and the Iberian Pyrite Belt. *Applied Geochemistry, 47*, 85-98. doi:10.1016/j.apgeochem.2014.05.012

Law, Y.-H. (2019). Politics could upend global trade in rare earth elements. *Science, 364*(6436), 114-115.

Lefticariu, L., Klitzing, K. L., & Kolker, A. (2019). Rare Earth Elements and Yttrium (REY) in coal mine drainage from the Illinois Basin, USA. *International Journal of Coal Geology*. doi:10.1016/j.coal.2019.103327

Lienemann, C.-P., Taillefert, M., Perret, D., & Gaillard, J.-F. (1997). Association of cobalt and manganese in aquatic systems: Chemical and microscopic evidence. *Geochemica et Cosmochimica Acta*, *16*(7), 1437-1446.

Lifton, J., & Hatch, G. (2015). TMR Advanced Rare-Earth Projects Index. Retrieved from http://www.techmetalsresearch.com/metrics-indices/tmr-advanced-rare-earth-projects-index/

Lin, R., Stuckman, M., Howard, B. H., Bank, T. L., Roth, E. A., Macala, M. K., . . . Granite, E. J. (2018). Application of sequential extraction and hydrothermal treatment for characterization and enrichment of rare earth elements from coal fly ash. *Fuel, 232*, 124-133. doi:10.1016/j.fuel.2018.05.141

Liu, H., Pourretc, O., Guoa, H., & Bonhourec, J. (2017). Rare earth elements sorption to iron oxyhydroxide: Model development and application to groundwater. *Applied Geochemistry, 87*, 158-166. doi:10.1016/j.apgeochem.2017.10.020

Liu, R., Altschul, E. B., Hedin, R. S., Nakles, D. V., & Dzombak, D. A. (2014). Sequestration Enhancement of Metals in Soils by Addition of Iron Oxides Recovered from Coal Mine

Drainage Sites. *Soil and Sediment Contamination: An International Journal, 23*(4), 374-388. doi:10.1080/15320383.2014.831027

Long, K. R., Gosen, B. S. V., Foley, N. K., & Cordier, D. (2010). *The Principal Rare Earth Element Deposits of the United States—A Summary of Domestic Deposits and a Global Perspective*. Retrieved from Available at http://pubs.usgs.gov/sir/2010/5220/.

Lozano, A., Ayora, C., & Fernández-Martínez, A. (2019a). Sorption of rare earth elements onto basaluminite: The role of sulfate and pH. *Geochimica et Cosmochimica Acta, 258*, 50-62. doi:10.1016/j.gca.2019.05.016

Lozano, A., Ayora, C., & Fernández-Martínez, A. (2020). Sorption of rare earth elements on schwertmannite and their mobility in acid mine drainage treatments. *Applied Geochemistry, 113*. doi:10.1016/j.apgeochem.2019.104499

Lozano, A., Fernandez-Martinez, A., Ayora, C., Di Tommaso, D., Poulain, A., Rovezzi, M., & Marini, C. (2019b). Solid and Aqueous Speciation of Yttrium in Passive Remediation Systems of Acid Mine Drainage. *Environ Sci Technol, 53*(19), 11153-11161. doi:10.1021/acs.est.9b01795

Luan, F., Santelli, C. M., Hansel, C. M., & Burgos, W. D. (2012). Defining manganese(II) removal processes in passive coal mine drainage treatment systems through laboratory incubation experiments. *Applied Geochemistry, 27*(8), 1567-1578. doi:10.1016/j.apgeochem.2012.03.010

Lynas Corporation Ltd. (2012). *Increase in Mt Weld Resource Estimate for the Central Lanthanide Deposit and Duncan Deposit*. Retrieved from 56 Pitt Street Sydney NSW 2000:

Manceau, A., Marcus, M. A., & Grangeon, S. (2012). Determination of Mn valence states in mixed-valent manganates by XANES spectroscopy. *American Mineralogist, 97*(5-6), 816-827. doi:10.2138/am.2012.3903

Manceau, A., Schlegel, M. L., Musso, M., Sole, V. A., Gauthier, C., Petit, P. E., & Trolard, F. (2000). Crystal chemistry of trace elements in natural and synthetic goethite. *Geochemica et Cosmochimica Acta, 64*(21), 3643-3661.

Manning, B. A., & Goldberg, S. (1997). Adsorption and Stability of Arsenic(III) at the Clay Mineral-Water Interface. *Environmental Science and Technology, 31*, 2005-2011.

Margolis, S. V., & Burns, R. G. (1976). Pacific Deep-Sea Manganese Nodules: Their Distribution, Composition, and Origin. *Annual Review of Earth and Planetary Sciences, 4*, 229-263.

Marsac, R., Davranche, M., Gruau, G., Bouhnik-Le Coz, M., & Dia, A. (2011). An improved description of the interactions between rare earth elements and humic acids by modeling: PHREEQC-Model VI coupling. *Geochimica et Cosmochimica Acta, 75*(19), 5625-5637. doi:10.1016/j.gca.2011.07.009

McLaughlin, J. R., Ryden, J. C., & Syers, J. K. (1981). Sorption of inorganic phosphate by iron- and aluminium- containing components. *Journal of Soil Science, 32*, 365-377.

Montross, S. N., Verba, C. A., Chan, H. L., & Lopano, C. (2018). Advanced characterization of rare earth element minerals in coal utilization byproducts using multimodal image analysis. *International Journal of Coal Geology, 195*, 362-372. doi:10.1016/j.coal.2018.06.018

Moraes, M. L. B., Murciego, A., Álvarez-ayuso, E., & Ladeira, A. C. Q. (2020). The role of Al13-polymers in the recovery of rare earth elements from acid mine drainage through pH neutralization. *Applied Geochemistry, 113*. doi:10.1016/j.apgeochem.2019.104466

National Energy Technology Laboratory, US Department of Energy, Rare Earth Element Database. Retrieved from https://edx.netl.doe.gov/ree/

Noack, C. W., Dzombak, D. A., & Karamalidis, A. K. (2014). Rare earth element distributions and trends in natural waters with a focus on groundwater. *Environ Sci Technol, 48*(8), 4317-4326. doi:10.1021/es4053895

Ohta, A., & Kawabe, I. (2001). REE(III) adsorption onto Mn dioxide (d-MnO2) and Fe oxyhydroxide: Ce(III) oxidation by d-MnO2. *Geochemica et Cosmochimica Acta, 65*(5), 695-703.

Okazaki, M., Sakaidani, K., Saigusa, T., & Sakaida, N. (1989). Ligand exchange of oxyanions on synthetic hydrated oxides of iron and aluminum. *Soil Science and Plant Nutrition, 35*(3), 337-346. doi:10.1080/00380768.1989.10434767

Orden, S., Macias, F., Canovas, C. R., Nieto, J. M., Perez-Lopez, R., & Ayora, C. (2021). Eco-sustainable passive treatment for mine waters: Full-scale and long-term demonstration. *J Environ Manage, 280*, 111699. doi:10.1016/j.jenvman.2020.111699

Papangelakis, V. G., & Moldoveanu, G. (2014). *Recovery of Rare Earth Elements from Clay Minerals*. Paper presented at the ERES 2014 — The 1st conference on European Rare Earth Resources, Milos, Greece.

Parkhurst, D. L., & Appelo, C. A. J. (2013). Description of Input and Examples for PHREEQC Version 3—A Computer Program for Speciation, Batch-Reaction, One-Dimensional Transport, and Inverse Geochemical Calculations: U.S. Geological Survey Techniques and Methods, book 6, chap. A43.

Post, J. E. (1999). Manganese oxide minerals: Crystal structures and economic and environmental significance. *Proceedings of the National Academy of Sciences of the United States of America, 96*, 3447-3454.

Pourret, O., & Davranche, M. (2013). Rare earth element sorption onto hydrous manganese oxide: a modeling study. *J Colloid Interface Sci, 395*, 18-23. doi:10.1016/j.jcis.2012.11.054

Pourret, O., & Martinez, R. E. (2009). Modeling lanthanide series binding sites on humic acid. *J Colloid Interface Sci, 330*(1), 45-50. doi:10.1016/j.jcis.2008.10.048

Prudêncio, M. I., Valente, T., Marques, R., & Braga, M. A. S. (2015). Geochemistry of rare earth elements in a passive treatment system built for acid mine drainage remediation. *Chemosphere, 138*, 691-700. doi:10.1016/j.chemosphere.2015.07.064

Pu, X., Vazquez, O., Monnell, J. D., & Neufeld, R. D. (2010). Speciation of Aluminum Precipitates from Acid Rock Discharges in Central Pennsylvania. *Environmental Engineering Science, 27*(2), 169-180.

Rakotonarivo, E., Bottero, J. Y., Thomas, F., Poirier, J. E., & Cases, J. M. (1988). Electrochemical Modelling of Freshly Precipitated Aluminum Hydroxide-Electrolyte Interface. *Colloids and Surfaces, 33*, 191-207.

Ram, R., Vaughan, J., Etschmann, B., & Brugger, J. (2019). The aqueous chemistry of polonium (Po) in environmental and anthropogenic processes. *Journal of Hazardous Materials, 380*, 120725. doi:https://doi.org/10.1016/j.jhazmat.2019.06.002

Ravel, B., & Newville, M. (2005). ATHENA, ARTEMIS, HEPHAESTUS: data analysis for X-ray absorption spectroscopy using IFEFFIT. *Journal of Synchrotron Radiation, 12*(4), 537-541. doi:doi:10.1107/S0909049505012719

Romero, F. M., Prol-Ledesma, R. M., Canet, C., Alvares, L. N., & Pérez-Vázquez, R. (2010). Acid drainage at the inactive Santa Lucia mine, western Cuba: Natural attenuation of arsenic, barium and lead, and geochemical behavior of rare earth elements. *Applied Geochemistry, 25*, 716-727. doi:10.1016/j.apgeochem.2010.02.004

Ryan, P. C., Hillier, S., & Wall, A. J. (2008). Stepwise effects of the BCR sequential chemical extraction procedure on dissolution and metal release from common ferromagnesian clay minerals: a combined solution chemistry and X-ray powder diffraction study. *Sci Total Environ, 407*(1), 603-614. doi:10.1016/j.scitotenv.2008.09.019

Santelli, C. M., Webb, S. M., Dohnalkova, A. C., & Hansel, C. M. (2011a). Diversity of Mn oxides produced by Mn(II)-oxidizing fungi. *Geochimica et Cosmochimica Acta, 75*(10), 2762-2776. doi:10.1016/j.gca.2011.02.022

Santelli, C. M., Webb, S. M., Dohnalkova, A. C., & Hansel, C. M. (2011b). Diversity of Mn oxides produced by Mn(II)-oxidizing fungi. *Geochemica et Cosmochimica Acta, 75*, 2762-2776. doi:10.1016/j.gca.2011.02.022

Schwertmann, U., & Carlson, L. (2005). The pH-dependent transformation of schwertmannite to goethite at 25C. *Clay Minerals, 40*, 63-66.

Senanayake, G. (2011). Acid leaching of metals from deep-sea manganese nodules – A critical review of fundamentals and applications. *Minerals Engineering, 24*(13), 1379-1396. doi:10.1016/j.mineng.2011.06.003

Seredin, V. V., & Dai, S. (2012). Coal deposits as potential alternative sources for lanthanides and yttrium. *International Journal of Coal Geology, 94*, 67-93. doi:10.1016/j.coal.2011.11.001

Shiel, A. E., Weis, D., & Orians, K. J. (2010). Evaluation of zinc, cadmium and lead isotope fractionation during smelting and refining. *Sci Total Environ, 408*(11), 2357-2368. doi:10.1016/j.scitotenv.2010.02.016

Sibrell, P. L., Montgomery, G. A., Ritenour, K. L., & Tucker, T. W. (2009). Removal of phosphorus from agricultural wastewaters using adsorption media prepared from acid mine drainage sludge. *Water Res, 43*(8), 2240-2250. doi:10.1016/j.watres.2009.02.010

Silva, G. A., Petter, C. O., & Albuquerque, N. R. (2018). Factors and competitiveness analysis in rare earth mining, new methodology: case study from Brazil. *Heliyon, 4*(3), e00572. doi:10.1016/j.heliyon.2018.e00570

Singer, D. A., Berger, V. I., & Moring, B. C. (2008). Porphyry copper deposits of the world: databse and grade and tonnage models. *U.S. Geological Survey Open-File Report 2008-1155*, 1-45.

Skousen, J. G., Zipper, C. E., Rose, A., Ziemkiewicz, P. F., Nairn, R. W., McDonald, L. M., & Kleinmann, R. L. (2017). Review of Passive Systems for Acid Mine Drainage Treatment. *Mine Water and the Environment, 36*, 133-153. doi:10.1007/s10230-016-0417-1

Slack, J. F., Kimball, B. E., & Shedd, K. B. (2017). Cobalt, Chapter F of Critical mineral resources of the United States - Economic and environmental geology and prospects for future supple *U.S. Geological Survey Professional Paper 1802*, F1-F40.

Spahiu, K., & Bruno, J. (1995). *Tachnical Report 95-35: A selected thermodynamic database for REE to be used in HLNW performance assessment exercises*. Retrieved from Cerdanyola, Spain:

Stewart, B. W., Capo, R. C., Hedin, B. C., & Hedin, R. S. (2017). Rare earth element resources in coal mine drainage and treatment precipitates in the Appalachian Basin, USA. *International Journal of Coal Geology, 169*, 28-39. doi:10.1016/j.coal.2016.11.002

Stream Restoration, I. (2018). Datashed. Retrieved from https://www.datashed.org/

Stuckman, M. Y., Lopano, C. L., & Granite, E. J. (2018). Distribution and speciation of rare earth elements in coal combustion by-products via synchrotron microscopy and spectroscopy. *International Journal of Coal Geology, 195*, 125-138. doi:10.1016/j.coal.2018.06.001

Sun, H., Zhao, F., Zhang, M., & Li, J. (2011). Behavior of rare earth elements in acid coal mine drainage in Shanxi Province, China. *Environmental Earth Sciences, 67*(1), 205-213. doi:10.1007/s12665-011-1497-7

Takahashi, Y., Sakami, H., & Nomura, M. (2002). Determination of the oxidation state of cerium in rocks by Ce LIII-edge X-ray absorption near-edge structure spectroscopy. *Geochemica et Cosmochimica Acta, 468*, 345-354.

Takahashi, Y., Shimizu, H., Usui, A., Kagi, H., & Nomura, M. (2000). Direct observation of tetravalent cerium in ferromanganese nodules and crusts by X-ray-absorption near-edge structure (XANES). *Geochemica et Cosmochimica Acta, 64*(17), 2929-2935.

Takaya, Y., Yasukawa, K., Kawasaki, T., Fujinaga, K., Ohta, J., Usui, Y., . . . Kato, Y. (2018). The tremendous potential of deep-sea mud as a source of rare-earth elements. *Sci Rep, 8*(1), 5763. doi:10.1038/s41598-018-23948-5

Tan, H., Zhang, G., Heaney, P. J., Webb, S. M., & Burgos, W. D. (2010). Characterization of manganese oxide precipitates from Appalachian coal mine drainage treatment systems. *Applied Geochemistry, 25*(3), 389-399. doi:10.1016/j.apgeochem.2009.12.006

Tanizaki, Y., Shimokawa, T., & Yamazaki, M. (1992). Physio-chemical speciation of trace elements in urban streams by size fractionation. *Water Research, 26*(1), 55-63.

Tonkin, J. W., Balistrieri, L. S., & Murray, J. W. (2004). Modeling sorption of divalent metal cations on hydrous manganese oxide using the diffuse double layer model. *Applied Geochemistry, 19*, 29-53. doi:10.1016/S0883-2927(03)00115-X

US Department of the Interior, U. G. S. (2020). Mineral Commodity Summaries, Co, January 2020.

USGS. (2018). *Mineral Commodity Summaries: Rare earths*. Reston, Virginia: United Stated Department of the Interior, United States Geological Survey.

USGS. (2020). *Mineral Commodity Summaries: Rare Earths*. Reston, Virginia: United Stated Department of the Interior, United States Geological Survey.

Van Gosen, B. S., Verplanck, P. L., Seal, R. I. R., Long, K. R., & Gambogi, J. (2017a). *Critical Mineral Resources of the United States - Economic and Environmental Geology and Prospects for Future Supply: U.S. Geologic Survey Professional Paper 1802*. Reston, VA.

Van Gosen, B. S., Verplanck, P. L., Seal, R. I. R., Long, K. R., & Gambogi, J. (2017b). Rare-earth elements, chapter O of Critical mineral resources of the United States - Economic and environmental geology and prospects for future supply. *U.S. Geological Survey Professional Paper 1802*, O1-O31.

Vass, C. R., Noble, A., & Ziemkiewicz, P. F. (2019a). The Occurrence and Concentration of Rare Earth Elements in Acid Mine Drainage and Treatment By-products: Part 1—Initial Survey of the Northern Appalachian Coal Basin. *Mining, Metallurgy & Exploration, 36*(5), 903-916. doi:10.1007/s42461-019-0097-z

Vass, C. R., Noble, A., & Ziemkiewicz, P. F. (2019b). The Occurrence and Concentration of Rare Earth Elements in Acid Mine Drainage and Treatment Byproducts. Part 2: Regional Survey of Northern and Central Appalachian Coal Basins. *Mining, Metallurgy & Exploration, 36*(5), 917-929. doi:10.1007/s42461-019-00112-9

Verplanck, P. L., Nordstrom, D. K., Taylor, H. E., & Kimball, B. A. (2004). Rare earth element partitioning between hydrous ferric oxides and acid mine water during iron oxidation. *Applied Geochemistry, 19*(8), 1339-1354. doi:10.1016/j.apgeochem.2004.01.016

Vesper, D. J., & Edenborn, H. M. (2012). Determination of free CO2 in emergent groundwaters using a commercial beverage carbonation meter. *Journal of Hydrology, 438-439*, 148-155. doi:10.1016/j.jhydrol.2012.03.015

Vesper, D. J., & Smilley, M. J. (2010). Attenuation and diel cycling of coal-mine drainage constituents in a passive treatment wetland: A case study from Lambert Run, West Virginia, USA. *Applied Geochemistry, 25*(6), 795-808. doi:10.1016/j.apgeochem.2010.02.010

Wagman, D. D., Evans, W. H., Parker, V. B., Schumm, R. H., & Halow, I. (1982). The NBS Tables of Chemical Thermodynamic Properties. Selected Values for Inorganic and C1 and C2 Organic Substances in SI Units. *Journal of Physical and Chemical Reference Data, 11 (Supplement No. 2)*.

Wall, F. (2014). Rare Earth Elements. In G. Gunn (Ed.), *Critical Metals Handbook*: John Wiley & Sons, Ltd.

Wallrich, I. L. R., Stewart, B. W., Capo, R. C., Hedin, B. C., & Phan, T. T. (2020). Neodymium isotopes track sources of rare earth elements in acidic mine waters. *Geochimica et Cosmochimica Acta, 269*, 465-483. doi:10.1016/j.gca.2019.10.044

Webb, S. M. (2005). SIXpack: a graphical user interface for XAS analysis using IFEFFIT. *Physica Scripta, 2005*, 1011-1014.

Yang, X. J., Lin, A., Li, X.-L., Wu, Y., Zhou, W., & Chen, Z. (2013). China's ion-adsorption rare earth resources, mining consequences and preservation. *Environmental Development, 8*, 131-136. doi:10.1016/j.envdev.2013.03.006

Younger, P. L., Banwart, S. A., & Hedin, R. S. (2002). *Mine Water: Hydrology, Pollution, Remediation*. Norwell, MA: Kluwer Academic Publishers.

Zhang, W., & Cheng, C. Y. (2007). Manganese metallurgy review. Part I: Leaching of ores/secondary materials and recovery of electrolytic/chemical manganese dioxide. *Hydrometallurgy, 89*(3-4), 137-159. doi:10.1016/j.hydromet.2007.08.010

Zhang, W., & Honaker, R. Q. (2018). Rare earth elements recovery using staged precipitation from a leachate generated from coarse coal refuse. *International Journal of Coal Geology, 195*, 189-199. doi:10.1016/j.coal.2018.06.008

Zhou, B., Li, Z., & Chen, C. (2017). Global Potential of Rare Earth Resources and Rare Earth Demand from Clean Technologies. *Minerals, 7*(11). doi:10.3390/min7110203

Ziemkiewicz, P., He, T., Noble, A., & Lui, X. (2016). *Recovery of Rare Earth Elements (REEs) from Coal Mine Drainage*. Paper presented at the West Virginia Mine Drainage Task Force, Morgantown, WV.